Perspectives of Upconverting Luminescent Nanoparticles for (bio)-analytical Applications

vorgelegt von

Stefan Wilhelm

aus Nabburg

(Landkreis Schwandorf)

im Juni 2014

Perspectives of Upconverting Luminescent Nanoparticles for (bio)-analytical Applications

Doctoral Thesis

Stefan Wilhelm

Diese Doktorarbeit entstand in der Zeit von Juli 2010 bis Juni 2014 am Institut für Analytische Chemie, Chemo- und Biosensorik an der Universität Regensburg.

Die Arbeit wurde angeleitet von Prof. Dr. Otto S. Wolfbeis.

Promotionsgesuch eingereicht am: 26. Juni 2014

Kolloquiumstermin: 18. Juli 2014

Prüfungsausschuss

Vorsitzende: Prof. Dr. Antje J. Baeumner

Erstgutachter: Prof. Dr. Otto S. Wolfbeis

Zweitgutachter: Prof. Dr. Reinhard Rachel

Drittprüfer: Prof. Dr. Bernhard Dick

Acknowledgments

First of all, I want to thank **Prof. Otto S. Wolfbeis** for providing me with this interesting topic, for the opportunity to work independently and valuable discussions.

Furthermore, I thank **Dr. Thomas Hirsch** for his great help, good advices and scientific discussions, and for his excellent support and encouragement during this thesis.

I also thank my colleagues **Dr. Wendy Patterson**, **Verena Muhr**, **Nadja Leibl**, **Rosmarie Walter**, **Sandy Himmelstoß**, **Dr. Alexander Riechers**, **Michael Lemberger**, **Alexander Zöpfl**, **Josef Heiland**, **Christoph Fenzl**, **Markus Buchner**, and **Joachim Rewitzer** for their encouraging support and profound advice.

I want to thank all members of the Institute of Analytical Chemistry, Chemo- and Biosensors for the great atmosphere in both scientific and private manner.

Finally, I want to thank my family and my parents for providing never-ending support.

Contents

1.   Introduction

1.1.   Nanoparticles and Colloids

Particles (organic or inorganic) with dimensions in the 1-100 nm range are referred to as nanoparticles (NPs; Greek νᾶνος: dwarf). They comprise an intermediate form of matter between individual atoms (or small molecules) and the bulk phase [1]. Exemplarily images of lanthanide-doped $NaYF_4$ NPs acquired by transmission electron microscopy (TEM) are shown in Figure 1. TEM is a commonly utilized powerful imaging technique which can be used to directly visualize NPs. Moreover, TEM allows for the characterization of material on the nanoscale in terms of their size, shape, crystallinity, elemental composition, *etc*. [2].

NPs can be considered as an assembly of only a few atoms, since atomic radii are about 1 Å [3]. Using a simplified model, one can calculate the number of gold atoms (atomic radius of 144 pm) per one single gold NP (AuNP) with a diameter of 2 nm to be ~ 334 (assuming spherical AuNPs) [4,5]. Accordingly, the number of gold atoms located at the surface of the AuNP is ~ 192 (~ 57 %). This is in stark contrast to the bulk phase where the majority of atoms are located in the interior. Hence, the surface area-to-volume ratio of a spherical particle increases with $6 \cdot d^{-1}$ (d: diameter) with decreasing particle diameter.
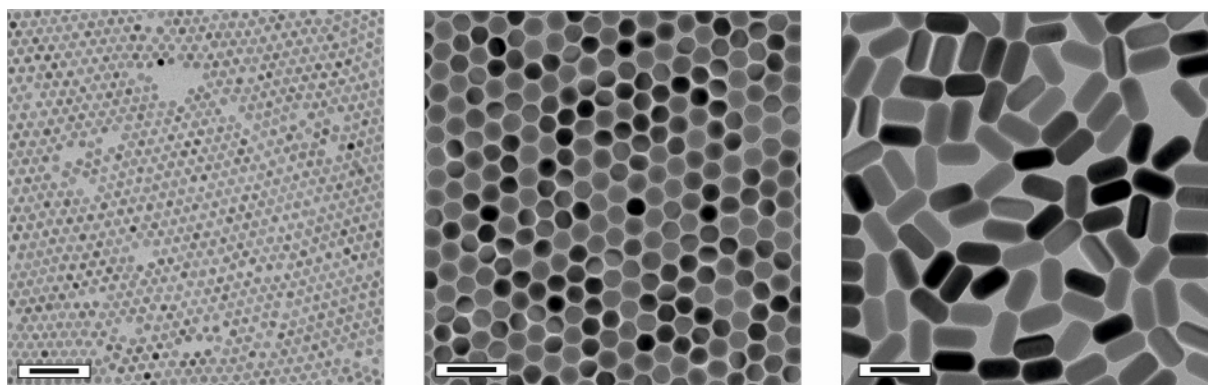
Figure 1 | Transmission electron microscopy images of lanthanide-doped $NaYF_4$ NPs deposited on a carbon-coated copper grid. The average particle diameter is ~ 9 nm (left) and ~ 22 nm (middle), respectively. The image on the right shows rod-like NPs with dimensions of ~ 28x54 nm. Scale bars indicate 60 nm.

Such a tremendous increase in the surface area-to-volume ratio can strongly alter the physical and chemical characteristics of NPs in comparison to their respective bulk phase [6]. For example, semiconductor NPs based on CdSe (referred to as quantum dots) show size dependent emissions in the visible range due to quantum confinement effects, which makes them highly attractive candidates for (bio)-imaging and sensing applications [7]. Another example are AuNPs (2-3 nm in diameter) dispersed on a titania support which have been found to show high catalytic activity for the oxidation of CO to CO_2 at ambient conditions [8,9]. Today, the majority of industrial catalysts consist of metallic NPs dispersed on high surface area supports [10].

Interestingly, the application of AuNPs to make ruby glass appeared around the 5th or 4th century B.C. in Egypt and China [11]. The most famous example is the *Lycurgus Cup*, which is ruby red in transmitted light and green in reflected light, due to the presence of AuNPs [12]. In 1857, Faraday reported on the formation of deep-red solutions of (colloidal) gold particles by reduction of an aqueous solution of chloroaurate [13]. The term *colloid* was coined by Graham in 1861 [14], which is defined as one substance (*e.g.* NPs) evenly dispersed throughout a solution. This type of mixture can be further specified as a *colloidal dispersion*.

A qualitative explanation to Faraday's observation is that AuNPs absorb visible light. In more detail, AuNPs display a broad absorption band (surface plasmon absorption) with a maximum at ~ 520 nm (for a NP diameter of ~ 15 nm), which is due to the collective oscillations of free electrons (plasmons) caused by the oscillating electric field of the irradiation light [15,16]. In 1908, Mie rationalized the nature of the surface plasmon absorption band by solving Maxwell's equations for the absorption and scattering of electromagnetic radiation by spherical metal particles [17].

The examples of CdSe quantum dots and AuNPs demonstrate how the material properties can change on the nanoscale due to quantum mechanical effects. The impact of nanomaterials and nanotechnology – a highly interdisciplinary science which includes aspects of material science, chemistry, physics, biology, and medicine – on (bio)-analytical applications will be discussed in the next chapters.

1.2.   Nanomaterials for (bio)-analytical Applications

1.2.1.   Gold Nanoparticles

One of the earliest reports on colloidal AuNPs used as labelling markers (immunogold staining) for the detection of *Salmonella* antigens in electron microscopy dates back to 1971 [18]. Here, Faulk and Taylor successfully applied AuNPs by taking advantage of their unique properties such as: (1) High electron density and therefore clear visibility in heavy metal ion-contrasted biological structures in transmission electron microscopy (TEM); (2) Preparation of NPs with a very narrow size distribution is possible; (3) Multiplexed labelling by use of AuNPs exhibiting significant differences in diameter [19]. Today, AuNPs are extensively used in the biomedical and (bio)-analytical fields due to their unique optical and electronic properties [20]. Their applications are summarized in numerous of excellent review articles which range from sensing [21], diagnosis [22], and photothermal therapeutics [23], to catalysis [24,25], surface plasmon resonance spectroscopy (SPR) [26], and surface enhanced Raman spectroscopy (SERS) [27,28].

In more detail, AuNPs can be used for absorption-based colorimetric sensing, since the aggregation of AuNPs of appropriate sizes (diameter > 3.5 nm) induces interparticle surface plasmon coupling, resulting in a visible color change [29]. The presence of an analyte may lead to aggregation of AuNPs functionalized with corresponding recognition elements on their surface. Such a colorimetric sensing scheme has been used for the detection of ssDNA targets with detection limits in the picomolar range [30]. Here, AuNPs were functionalized with respective complementary oligonucleotide strands leading to aggregation of AuNPs due to complementary DNA base pairing with target ssDNA.

In a different fluorescence-based approach for sensing of ssDNA, a hairpin loop structure (molecular beacon) is used. This structure is formed by a self-complementary nucleic acid probe and conjugated to an organic fluorophore on one end and a AuNP on the other end (see Scheme 1). As an example, the AuNP (diameter 1.4 nm) acts as a fluorescence quencher for the organic fluorophore Rhodamine 6G due to non-radiative energy transfer from the dye to the metal nanoparticle. The hairpin structure changes to a rod-like conformation after hybridization to a ssDNA target. Accordingly, the distance between the

dye (Rhodamine 6G) and the AuNP gets larger. This results in a significant increase in fluorescence since the quenching efficiency is > 99.9 % [31].
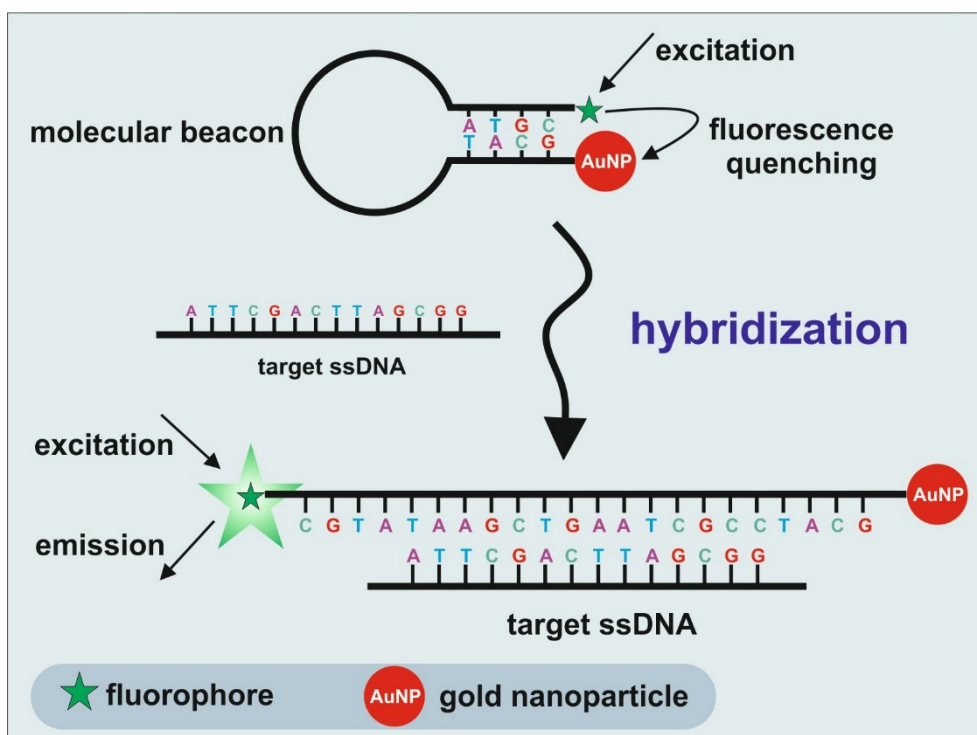
Scheme 1 | A fluorescence-based assay for sensing of target ssDNA using a gold-quenched nucleic acid probe (molecular beacon). The hairpin structure of the molecular beacon brings the fluorophore and the AuNP in close proximity. Accordingly, upon excitation of the fluorophore, its emission is quenched by the AuNP. Through sequence-specific hybridization to a ssDNA target, the hairpin structure changes to a rod-like conformation which increases the distance between the fluorophore and the quencher (AuNP). Consequently, the fluorescence of the organic dye is restored.

1.2.2. Magnetic Nanoparticles

Magnetic nanoparticles (MNPs) based on magnetite (Fe_3O_4) or maghemite (γ-Fe_2O_3) constitute another important class of functional NPs for (bio)-analytical applications [32]. They are referred to as superparamagnetic iron oxide nanoparticles (SPIONs) since particles with diameters smaller than ~ 20 nm (single magnetic domain limit) exhibit superparamagnetism at room temperature (*i.e.* their magnetization can randomly flip direction under the influence of temperature, leading to a net magnetic moment of zero in absence of an external magnetic field) [33]. SPIONs can be magnetically manipulated using an external

magnetic force (see Figure 2) and used for magnetic separation of target species from a complex mixture (*e.g.* separation of proteins from a cell lysate) [34], or remote-controlled delivery of drugs and therapeutics [35,36]. Other applications employ MNPs for hyperthermia [37], (bio)-sensing [38], or as contrast agents for magnetic resonance imaging (MRI) [39].

SPIONs for MRI diagnosis are widely used for clinical purposes (*e.g.* Feridex® or Resovist®) [40]. Besides SPIONs, paramagnetic gadolinium chelates are also widely used as MRI contrast agents. However, these complexes must be administered in high dosage (0.1 mmol·kg^{-1} body weight for Gadovist®) because of their relatively low sensitivity [41]. Furthermore, free gadolinium ions leached from complexes can have toxic side effects like nephrogenic systemic fibrosis [42]. Finally, most gadolinium chelates are designed to have a very short circulation time, which precludes high-resolution and/or targeted MRI. In contrast, SPIONs exhibit high relaxivity and are known to be biologically well tolerated and benign. The toxicity, metabolism, and pharmacokinetics of intravenously injected SPIONs have been well studied [43]. SPIONs can be tailored in terms of size and surface functionalization which is beneficial for targeted imaging and prolonged circulation times. Moreover, they can be used as nano-platforms for multimodal imaging (*e.g.* MRI, positron emission tomography (PET), fluorescence) by conjugation to radioactive tracers or fluorescent dyes [44].
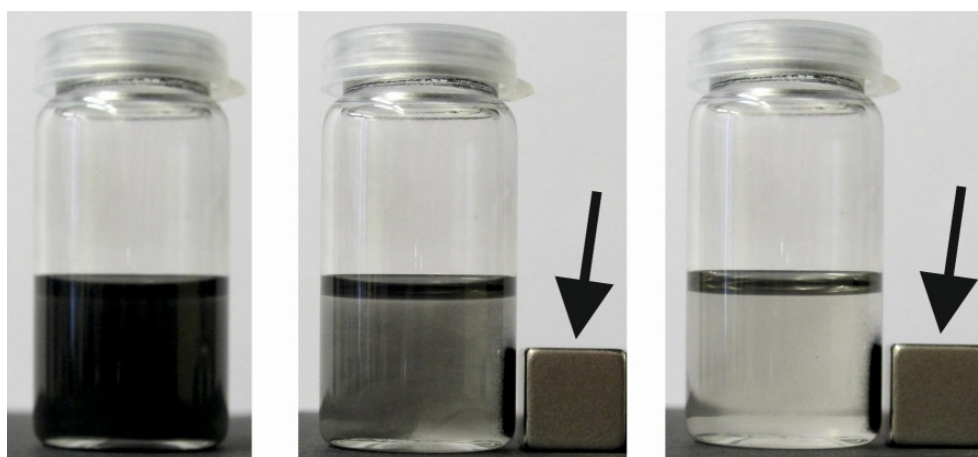
Figure 2 | Magnetic nanoparticles can be collected by using an external permanent magnet (arrow). Colloidal stable, oleic acid – coated MNPs dispersed in cyclohexane are shown on the left. Snapshots taken 5 s (middle) and 10 s (right) after applying an external magnetic field, respectively.

1.2.3. Liposomes

A third example of nanomaterials suitable for medical and (bio)-analytical applications are liposomes (vesicles). In their simplest form, liposomes are composed of a phospholipid bilayer surrounding an aqueous core [45]. The size of liposomes ranges from typically 25-50 nm for small unilamellar vesicles to 100 nm – 1 µm (or even several microns) for large unilamellar vesicles. Both hydrophilic and hydrophobic compounds can be encapsulated into the inner cavity (aqueous core) or incorporated into the bilayer membrane of liposomes, respectively. Accordingly, liposomes are utilized as versatile carriers for drugs or therapeutics, which typically serves to improve the pharmacokinetics and biodistribution of a drug [46]. Currently there are ~ 11 liposomal drug formulations (*e.g.* chemotherapeutics) available which are approved for clinical use, and many more are in clinical or preclinical development [47].

Furthermore, liposomes provide an excellent means for signal amplification in biosensors [48]. Signal markers such as dyes, enzymes, salts, chelates, DNA, or electrochemical and chemiluminescent species can be encapsulated within liposomes. Labelling of vesicles with biorecognition elements including bilayer incorporated gangliosides, cholesterol modified DNA oligonucleotides, and peptides, enzymes, and antibodies covalently attached to the hydrophilic headgroup of a lipid can be easily achieved. The controlled release of liposomal cargo using phase transition, ultrasound, or lysis strategies after a one-to-one biological binding event may lead to signal amplification. Consequently, the limit of detection using liposome-based biosensor formats or assays (*e.g.* lateral flow assay, flow injection analysis, high-throughput microtiter plate, or microfluidic devices) is usually quite low (*viz.* parts-per-billion, ppb) [49].

In summary, the development of colloidal nanomaterials (*e.g.* AuNPs, MNPs, SPIONs, and liposomes) for applications in medicine and (bio)-analysis has shown great potential. Colloidal stability of nanomaterials in appropriate media (*e.g.* cell culture buffer systems, or body fluids) is an essential prerequisite for their medical and (bio)-analytical application (*in vitro* and *in vivo*). Therefore, sophisticated engineering of surface properties is

indispensable in order to avoid aggregation of nanomaterials under physiological conditions. Beyond this, recent efforts in nanotechnology offer the possibility to combine useful chemical or physical properties of different nanomaterials within one single entity, thus allowing for synthesis of bi- or even multifunctional (hybrid) NPs (*e.g.* Fe_3O_4-Au, dumbbell-like NPs) [50,51]. Accordingly, colloidal nanomaterials are promising platforms for new and powerful theranostic agents (therapy and diagnostics) and may improve the performance and sensitivity of (bio)-analytical assays.

1.3.   Luminescent Nanomaterials

1.3.1.   Specifications of Ideal Luminescent Labels

Luminescence-based techniques are excellent methods to investigate fundamental processes in life sciences. They represent extremely important and powerful (bio)-analytical tools in medicine, biology, and chemistry due to their fast, sensitive (down to the single-molecule level), reliable, and reproducible detection procedures. There is a large variety of molecular chromophores (*e.g.* organic dyes, metal-ligand complexes, lanthanide chelates, or fluorescent proteins) from which one can choose for (bio)-imaging and sensing applications [52]. As an example, these chromophores can be employed as extrinsic luminescent labels, when the target of interest is non-luminescent or its intrinsic luminescence is not adequate for solving the analytical question of interest.

An ideal luminescent label for biological applications should fulfill the following requirements: (a) High molar absorption coefficient at a convenient excitation wavelength (without simultaneous excitation of the biological matrix); (b) Detection of luminescence with conventional instrumentation; (c) High luminescence quantum yield (number of emitted photons occurring per number of absorbed photons); (d) High brightness (product of the molar absorption coefficient at the excitation wavelength and the luminescence quantum yield); (e) Large Stokes shift between excitation and emission wavelength; (f) Solubility and stability in relevant hydrophilic media (*e.g.* buffers, cell culture media); (g) High photostability; (h) Functional groups for site-specific labeling; (i) Low

toxicity; (j) Reported data about its photophysics (luminescence lifetime, luminescence decay behavior, appearance of luminescence blinking); (k) Availability in reproducible quality; And (l) suitability for multiplexing (small and symmetric emission bands are favorable) [52].

During the last decades, luminescent labeling using nanoparticle-based chromophores as alternatives to conventional molecular dyes gained increasingly more attention [53,54]. The most ambitious and fascinating application of luminescent nanomaterials is probably related to medicine, molecular biology, and (bio)-analytics [55]. Here, these nanomaterials are promising tags for luminescent labeling and optical (bio)-imaging in order to enable novel techniques of non-invasive observation of complex vital functions (*e.g. in vivo* whole-body diagnosis, or *in vitro* examination of individual organs or cells) [56]. Generally, luminescent nanomaterials can be assigned to two classes, (a) extrinsic (dye-doped) luminescent nanomaterials, and (b) nanomaterials exhibiting intrinsic luminescence [57].

1.3.2.   Extrinsic Luminescent Nanomaterials

The first group comprises NPs doped with (organic or inorganic) chromophores as active luminescent species [58]. Examples are NPs made out of silica or organic polymers such as polystyrene doped with organic fluorophores [59,60]. The material itself does not show any intrinsic luminescence, but rather acts as a kind of a host matrix for molecular chromophores. Therefore, this group can be specified as extrinsic luminescent nanomaterials. The advantages of dye-doped NPs over single molecular dyes are many. Polymer- and silica-based NPs with tunable diameters from 10 to 100 nm can include tens, hundreds or even thousands of molecular luminophores, which leads to a significant gain in luminescence intensity and brightness [61]. This is an advantageous feature for (bio)-imaging and sensing applications since the signal-to-noise ratio can be greatly improved [62]. However, the concentration of dye molecules embedded into NPs must be strictly controlled in order to avoid self-quenching processes [63].

The incorporation of molecular chromophores inside a silica or polymer matrix protects them from the surrounding environment and increases their photostability. Hence, this concept is a universal and highly modular approach since physicochemical properties of

NPs (size, shape, surface chemistry, *etc.*) can be varied and optimized with regard to their particular application [64]. Moreover, even hydrophobic luminophores can be easily entrapped using reverse microemulsion techniques. This is a fast, simple, and elegant way for the phase transfer of hydrophobic chromophores into hydrophilic media [65,66]. Additionally, other molecules like drugs, magnetic contrast chelates, or chemotherapeutics can also be incorporated into polymer and silica NPs, which makes them promising contenders for use in smart drug delivery and therapy systems, yielding multifunctional NPs [67,68]. Furthermore, the surface of such NPs can be modified in order to introduce biorecognition ligands (*e.g.* antibodies, proteins, or DNA) enabling target-oriented imaging, sensing, and active delivery of drug molecules [69,70].

1.3.3. Intrinsic Luminescent Nanomaterials

The second group covers nanomaterials displaying intrinsic luminescence. In contrast to the first group, here, the nanomaterial itself is capable of generating luminescence due to quantum mechanical or confinement effects without the need for any additional luminophore. A further classification of the second group can be made as follows: (a) semiconductor NPs; (b) metal nanoclusters; (c) carbon-based nanomaterials; and (d) metal-doped NPs. The physical and optical properties of luminescent nanomaterials including nanodiamonds (NDs) [71], carbon nanodots (C-dots) [72], graphene oxide (GO) [73], carbon nanotubes (CNTs) [74], quantum dots (QDs), and gold nanoclusters (AuNCs) [75] are compared to conventionally used organic fluorophores (OFs) including fluorescein, Cy3, Cy5, Texas Red, or Nile Red (see Table 1).

NDs are carbon NPs with a truncated octahedral architecture and are typically about 5 to 20 nm in diameter [76]. They are made from milling microdiamonds (top-down approach), chemical vapor deposition, shockwave, or detonation processes [77]. In addition, NDs exhibit superior chemical stability and excellent resistance to photobleaching along with low toxicity [78]. However, their luminescence is not easily tunable [79]. Moreover, aggregation of colloidal NDs is often a serious problem and the production of homogeneous samples with a narrow size distribution is challenging.

Table 1 | Comparison of physical and optical properties of luminescent nanomaterials and organic fluorophores.

Property	NDs	C-dots	GO	CNTs	AuNCs	QDs	OF
Material	Carbon	Carbon	Carbon	Carbon	Gold	Semi-conductor	Organic fluorophor
Size [nm]	5 – 20	< 10	Thickness ~0.6 Lateral: variable	Variable	< 2	2 – 10	< 1
Quantum Yield [%]	~ 100	5 – 60	< 10	< 25	< 20	10 – 90	50 - 100
FWHM* [nm]	> 60	> 60	> 80	> 60	> 60	25 – 35	35 - 100
Photo-stability	Excellent	Excellent	Excellent	Excellent	Excellent	Good	Medium
Lifetime [ns]	10 – 20	< 10	< 10	< 5	> 100	> 10	< 10

*FWHM: full width at half maximum. NDs: nanodiamonds; C-dots: carbon nanodots; GO: graphene oxide; CNTs: carbon nanotubes; AuNCs: gold nanoclusters; QDs: quantum dots; OFs: organic fluorophores. Adopted from Ref. [55].

An additional category of carbon-based nanomaterial are C-dots. They exhibit a quasi-spherical particle shape with diameters < 10 nm. C-dots display non-blinking, size and excitation wavelength dependent photoluminescence behavior, and are highly photostable. However, the mechanisms of photoluminescence and the photophysical properties of C-dots and most other carbon-based nanomaterials are poorly understood [80]. GO offers intrinsic aqueous solubility due to the presence of functional groups (*e.g.* carboxyl, or hydroxyl groups) [81]. One drawback of this material is that its broad emission cannot be easily tuned [82]. CNTs do not show any photobleaching, however, the intensity of photoluminescence is relatively weak [83]. Noble metal nanoclusters (*e.g.* AuNCs) are smaller than 2 nm, exhibit no apparent plasmonic properties, and have excitation and emission bands similar to those of molecular dyes [84]. The luminescence properties of AuNCs are size-dependent and sensitive to their environment (*i.e.* pH, ionic strength, or temperature). Large Stokes shifts and long luminescence lifetimes have been observed. However, the controlled synthesis of high quality AuNCs (< 2 nm in diameter) is still very difficult [85].

Another important class of colloidal NPs are semiconductor nanocrystals with dimensions between 2 nm and 10 nm. They are referred to as quantum dots (QDs) and display size-dependent optical properties (quantum size effect), which arise from interactions between electrons, holes, and their local environment [86,87]. QDs absorb photons when the excitation energy exceeds the band gap. Electrons are promoted from the valence band to the conduction band during this process. The emission of light is due to the recombination of electron-hole pairs (excitons), which is referred to as excitonic fluorescence. For example, bulk CdSe has a band gap energy of 1.76 eV and a Bohr exciton diameter of 9.6 nm, whereas the band gap energy of 2-7 nm CdSe QDs decreases from 2.8 to 1.9 eV [88]. As a result, the wavelength of the corresponding emission can be tuned continuously from 450 to 650 nm, depending on the nanocrystal diameter. The diameter of QDs and therefore the emission wavelength can be tuned by controlling the temperature and duration of crystal growth during the synthesis. QDs are highly attractive candidates for *in vitro* and *in vivo* optical imaging [89,90,91], cell tracking [92], gene and drug delivery [93], and diagnostic applications [94,95] due to their unique optical properties, which makes them promising alternatives to conventionally used organic fluorophores.

In more detail, the absorption bands of QDs are rather broad and there is a continuous increase of absorption from their first exciton peak towards shorter wavelengths [96,97], which is in stark contrast to organic fluorophores. This broad absorption allows for free selection of the excitation wavelength, which is beneficial in order to separate emission from excitation light. Moreover, a single light source is sufficient for the excitation of QD emissions. The emission can be continuously tuned from ultraviolet (UV) to near-infrared (NIR), depending on the elemental composition and nanocrystal diameter [98]. Bawendi and coworkers reported a molar extinction coefficient for CdS QDs of $\sim 10^5$-10^6 $M^{-1} \cdot cm^{-1}$, depending on the particle diameter and the excitation wavelength [99]. Hence, QDs exhibit molar extinction coefficients as high as organic fluorophores or even one order of magnitude higher [100,101]. The full width at half maximum (FWHM) of the symmetric emission peak of QDs with a Gaussian peak profile is ~ 30 nm at room temperature [102]. This makes them ideal candidates for spectral multiplexing.

The width of emission peaks of QDs is mainly determined by the size distribution of the nanocrystals. Luminescence quantum yields (QYs) of QDs in the visible range (400-700 nm) are comparable to those of fluorescent dyes. As an example, the QY of

CdSe QDs is ~ 0.8 [103,104], which is quite high. However, QYs of 0.97 or even higher can be found for organic dyes such as fluorescein under alkaline conditions [105]. In the NIR region (> 700 nm), QDs exhibit certain advantages over organic fluorophores, such as a typically higher quantum yield and superior resistance to photobleaching [106]. The excited state decay rate of QDs is typically > 10 ns and thus slightly slower than that of organic dyes (~ 1-10 ns) [107]. This enables the use of time-gated detection to separate the QDs' luminescence from short-lived luminescence interference from scattered excitation light or cellular autofluorescence, which enhances sensitivity [108]. Another favorable feature of QDs is their large two-photon absorption cross section (10^3-10^4 GM), which is orders of magnitude larger than those of organic chromophores [109,110]. However, an inherent disadvantage of QDs is their complicated size-dependent, surface-dependent, wavelength-dependent, bi- (or even multi-) exponential decay behavior, which renders time-resolved luminescence measurements very difficult [111].

Finally, there are two additional drawbacks of QDs. First, the surface defects in the crystal structure can serve as temporary "traps" for electrons or holes. This prevents their radiative recombination and leads to a fluorescence intermittency (so-called blinking), which is apparent from single luminescent nanocrystals [112]. Second, the cytotoxicity of QDs is a serious threat, since semiconductor nanocrystals are mostly composed of toxic heavy metal ions (*e.g.* Cd^{2+}, Zn^{2+}, Pb^{2+}) [113,114]. However, toxicity may also be problematic using organic dyes.

In conclusion, there is a large variety of different luminescent nanomaterials suitable for (bio)-analytical applications. The drawback of limited photostability of organic fluorophores can be overcome to a certain extent by using dye-doped silica or polymer NPs. QDs, C-dots, and metal nanoclusters exhibit promising potential for (bio)-imaging and sensing due to their unique optical properties and extraordinary photostability. Therefore, they can be considered as alternatives to conventional organic fluorophores. However, their emissions are related to quantum confinement effects. Hence, a precise adjustment and control of their physicochemical properties (size, shape, surface chemistry, *etc.*) are important prerequisites in order to obtain NPs with defined characteristics and efficient luminescence.

1.4.   Upconverting Luminescent Nanoparticles

1.4.1.   Characteristics and Composition

All luminescent nanomaterials discussed so far (including molecular luminophores) require excitation by UV or visible light and show Stokes-shifted emissions (*i.e.* the emitted light has a longer wavelength than the excitation light). Therefore, they can be designated as downconverting luminescent (nanomaterials) nanoparticles (DCLNPs). However, in recent years, a new class of nanoscale luminophores, which are referred to as upconverting luminescent nanoparticles (UCLNPs), has gained much scientific interest. Here, the emitted light has a shorter wavelength than the excitation light, which is in stark contrast to DCLNPs. An image of UCLNPs emitting predominantly blue, green, and red emission upon 980 nm continuous wave laser excitation is shown in Figure 3. This phenomenon is called photon upconversion and was first described by Auzel, Ovsyankin and Feofilov in the 1960s [115].

There are several excellent review articles which summarize and discuss the different mechanisms of upconversion in detail [116,117,118]. Briefly the processes of photon upconversion can be roughly divided into three main classes: (1) energy transfer upconversion (ETU, see Scheme 2); (2) excited-state absorption (ESA); and (3) photon avalanche (PA). In contrast to simultaneous two-photon absorption [119,120] or second-harmonic generation [121,122], all of these three processes are based on the sequential absorption of two or more photons by existing, metastable, long-lived electronic energy states of metal ions. However, ETU is by far the most efficient UC process [123]. As a consequence of these sequential absorption steps, highly excited electronic energy states are populated from which upconversion luminescence occurs. Therefore, photon upconversion is a non-linear optical phenomenon [124].
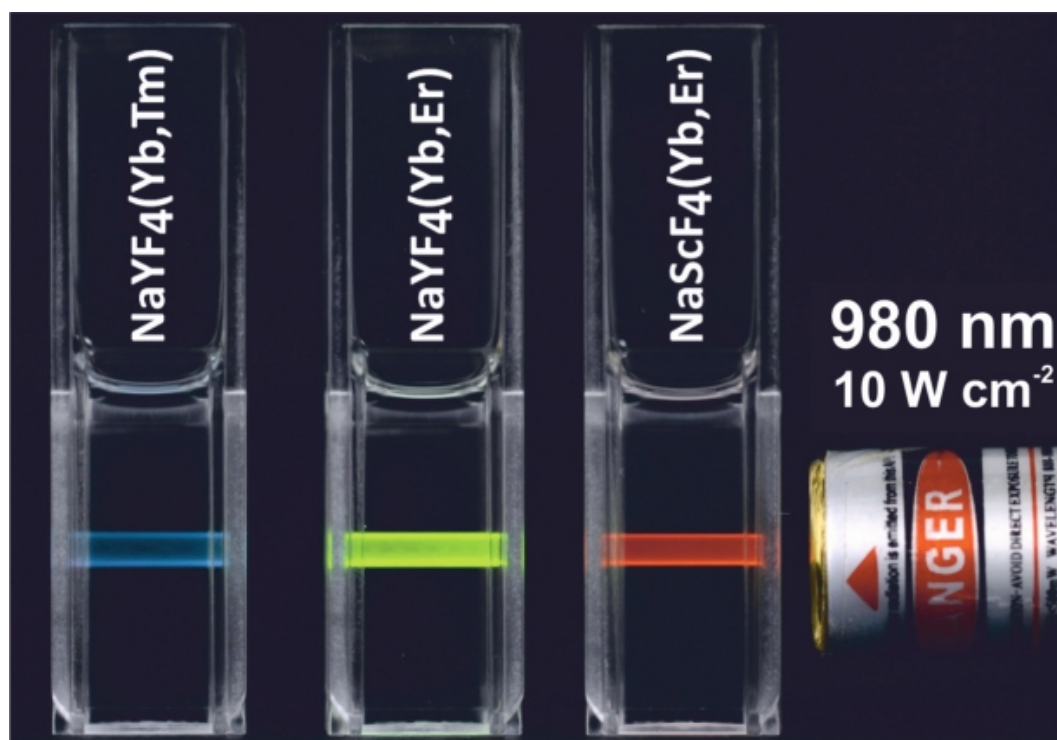
Figure 3 | UCLNPs dispersed in cyclohexane emit visible light upon 980 nm continuous wave laser excitation (laser power density 10 W·cm^{-2}). Predominant blue (NaYF$_4$ doped with Yb^{3+}/Tm^{3+}), green (NaYF$_4$ doped with Yb^{3+}/Er^{3+}), and red (NaScF$_4$ doped with Yb^{3+}/Er^{3+}) luminescence can be observed by the bare eye.

UCLNPs are composed of an inorganic (crystalline) host material doped with metal ions, which act as active luminescent centers (activators). A large number of different dopants embedded into suitable host materials has been reported to show photon upconversion, for example solids doped with transition-metal ions (3d, 4d, 5d) like Ti^{2+}, Ni^{2+}, Mo^{3+}, Re^{4+}, or Os^{4+} [116,118]. However, the highest upconversion efficiencies at room temperature are observed for lanthanide-doped (Ln^{3+}) solids [125]. Most commonly, upconversion (nano)-phosphors contain trivalent 4f ions such as Er^{3+}, Tm^{3+}, or Ho^{3+} as activators. The f-f transitions of lanthanide ions are strongly forbidden by the parity selection rule resulting in long lifetimes of the excited states (in the range of µs to ms) [126]. As a consequence, lanthanide ions typically show low molar absorption coefficients on the order of 1 M^{-1}·cm^{-1} [127]. The energy of Ln^{3+} electronic levels is well defined due to the shielding of the 4f orbitals by filled 5s^{2}p^6 sub-shells (*i.e.* there is no significant variation of the energy levels caused by the chemical environment in which Ln^{3+} ions are inserted). In principle, the absorption can be greatly improved by increasing the dopant concentration of lanthanide ions per single (nano)-crystal. However, radiation-less deactivation and cross-relaxation processes

can occur at high doping concentrations [128]. Thus, strongly absorbing sensitizer ions, which should also ensure efficient non-radiative energy transfer to activator ions, are additionally doped into the crystalline host matrix in order to further increase absorption. Yb^{3+} ions having a molar absorption coefficient of ~ 10 $M^{-1} \cdot cm^{-1}$ are the most commonly used sensitizers for Er^{3+}, Tm^{3+}, or Ho^{3+} doped upconverting (nano)-phosphors [129].

The efficiency of upconversion luminescence is strongly influenced by the crystalline host material and its crystal structure. The ion-to-ion distance of dopants located within the host lattice and their spatial arrangement are of great importance [130]. Therefore, a suitable host material provides a matrix to bring these dopants into optimal position with respect to one another [131]. The most efficient host material for Yb^{3+}/Er^{3+} and Yb^{3+}/Tm^{3+} doped upconverting (nano)-phosphors is hexagonal phase (β) $NaYF_4$ [132]. This fluoride-based host matrix is superior to oxygen-based hosts because of its relative low phonon energy of ~ 350 cm^{-1}, which is beneficial for long lifetimes of excited electronic states [133]. Moreover, Y^{3+} can be easily substituted by lanthanide ions since both exhibit similar ionic radii. Thus, the formation of crystal defects and lattice stress is prevented. The crystal structure of a host material is another important aspect for efficient upconversion luminescence. Here, $NaYF_4$ constitutes an excellent example, since it exists in two polymorphs at ambient pressure: (a) cubic (α-phase) – a metastable high-temperature phase; and (b) hexagonal (β-phase) – a thermodynamically stable low-temperature phase [134]. It is reported that the efficiency of upconversion luminescence is approximately one order of magnitude higher for bulk β-$NaYF_4$ in comparison to α-$NaYF_4$ [135,136].

1.4.2.   Photophysical Properties

The "flagship" upconversion (nano)-phosphor material is undoubtedly β-$NaYF_4$ (acting as a host matrix material) doped with either Yb^{3+}/Er^{3+} or Yb^{3+}/Tm^{3+} ion couples. The doping concentrations are usually ~ 20-25 mol% of Yb^{3+}, ~ 2 mol% of Er^{3+}, and ~ 0.3 mol% of Tm^{3+} ions [137]. Here, Yb^{3+} ions act as sensitizers which absorb excitation light at 980 nm. In contrast to other lanthanides, Yb^{3+} ions have a relatively simple energy level structure [138]. They undergo a transition from their $^2F_{7/2}$ to $^2F_{5/2}$ electronic state upon NIR excitation. Subsequently, energy is sequentially transferred from excited sensitizer ions (Yb^{3+}) to

adjacent activator ions (Er^{3+}) *via* a non-radiative, resonant energy transfer upconversion process. The energy of $^2F_{5/2}$ states of Yb^{3+} and $^4I_{11/2}$ of Er^{3+} is very similar, which allows for an efficient energy transfer from excited state Yb^{3+} to neighboring Er^{3+} to occur. Subsequently, an additional energy transfer from another excited state Yb^{3+} to the Er^{3+} can take place, resulting in further excitation to its $^4F_{7/2}$ excited state. As a result of these ETU processes, Er^{3+} ions are promoted from their $^4I_{11/2}$ ground states to $^4F_{7/2}$ excited states. Multicolor upconversion luminescence of Er^{3+} activator ions can be observed in the visible range (see Scheme 2) upon relaxation to their $^4I_{15/2}$ ground state. The primary emission peaks are located in the green ($^2H_{11/2}/^4S_{3/2} \rightarrow {}^4I_{15/2}$) and red ($^4F_{9/2} \rightarrow {}^4I_{15/2}$) region of the electromagnetic spectrum, depending on the particular relaxation pathway. Due to their unique electronic configuration, lanthanide ions display emissions with extraordinarily narrow luminescence bandwidths [139]. Here, the FWHM of the emission peaks are typically < 20 nm (see Figure 4).

The relatively long lifetime of lanthanide ions excited states on the millisecond time scale is beneficial for these ETU mechanisms. Hence, an inexpensive continuous wave (CW) diode-laser operating at 980 nm with a moderate excitation power density of ~ 10 $W \cdot cm^{-2}$ is sufficient in order to induce upconversion luminescence based on ETU (see Figure 4). This is orders of magnitude lower than for simultaneous two-photon absorption processes. Here, expensive ultrashort pulsed lasers operating at power densities of ~ 10^5-10^9 $W \cdot cm^{-2}$ are required [140] for the excitation of dye molecules. Simultaneous two-photon absorption involves a "virtual" intermediate state of dye molecules exhibiting extremely short lifetime which is in stark contrast to the long excited state lifetime of lanthanide ions in ETU processes.

The energy levels and ETU mechanisms of Yb^{3+}/Tm^{3+}-doped upconversion (nano)-phosphors are shown in Scheme 3. Here, Tm^{3+} ions can be excited into their $^1D_2$ electronic state by a four times Yb^{3+}-sensitized sequential energy transfer. As a result, emissions of Tm^{3+} activator ions in the UV, visible, and NIR spectral range can be detected upon relaxation to their electronic ground state ($^3H_6$). Figure 5 displays the typical predominant blue luminescence of β-$NaYF_4$ UCLNPs doped with Yb^{3+}/Tm^{3+} ions upon 980 nm CW laser excitation (laser power density 10 $W \cdot cm^{-2}$). Additionally, a characteristic luminescence spectrum of Yb^{3+}/Tm^{3+} doped upconversion (nano)-phosphors is shown in

Figure 5, exhibiting distinct emission peaks at 360 nm ($^1D_2 \rightarrow {}^3H_6$), 475 nm ($^1G_4 \rightarrow {}^3H_6$), 648 nm ($^1G_4 \rightarrow {}^3F_4$), and 800 nm ($^3H_4 \rightarrow {}^3H_6$).
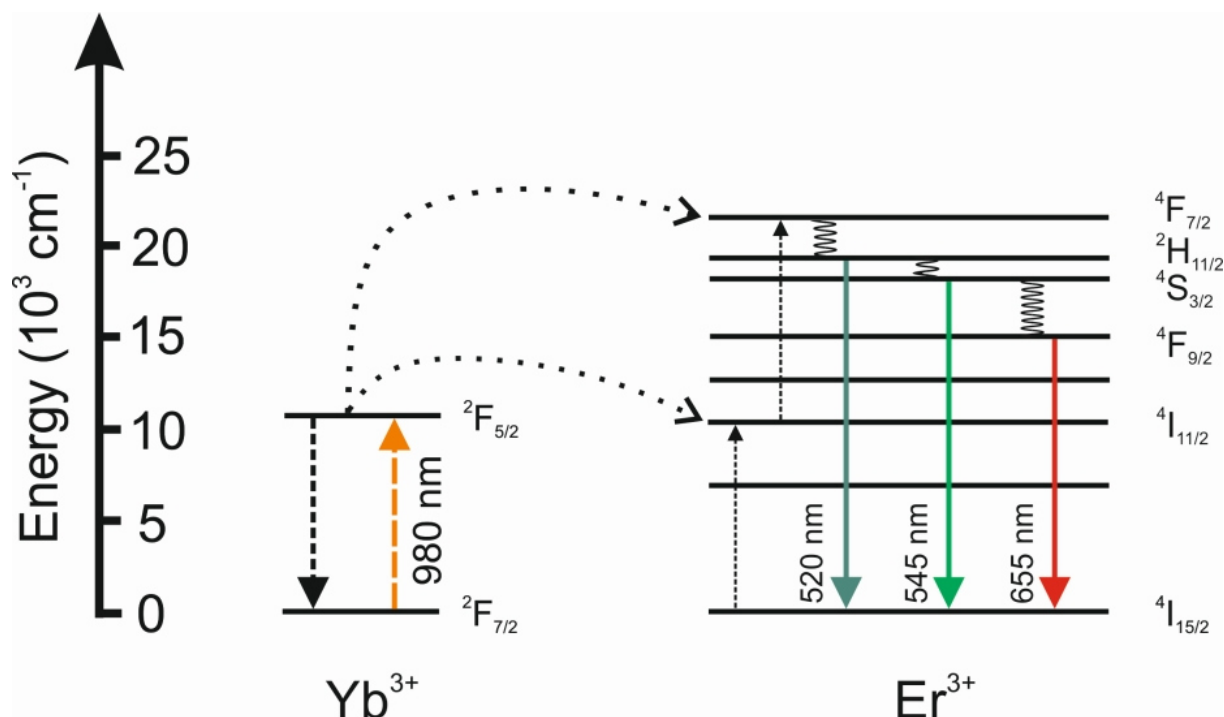
Scheme 2 | Energy level diagram and energy transfer upconversion (ETU) mechanisms for a Yb^{3+}/Er^{3+}-doped (sensitizer/activator) system. Excitation light (980 nm) is absorbed by Yb^{3+} sensitizer ions and sequentially transferred to Er^{3+} activator ions leading to multicolor upconversion luminescence in the visible range. Arrows indicate radiative, non-radiative energy transfer, and multiphonon relaxation processes.

Excitation of UCLNPs (employed as luminescent labels, biomarkers, or sensing probes) by NIR light rather than UV radiation provides several advantages such as: (a) Photo damage of biological specimens is significantly reduced [141]; (b) The penetration depth into biological tissue is higher since excitation takes place in the so-called biological optical window (from ~ 650 to ~ 1000 nm), where the absorption coefficient of tissue is minimal [142,143]; and (c) Very weak autofluorescence background from biological tissue resulting in improved detection sensitivity due to higher signal-to-noise ratio [144]. In addition, UCLNPs do not show any blinking characteristics under continuous laser excitation and are extremely resistant to photobleaching as well as photochemical degradation even under intense excitation power densities [145]. This makes them highly attractive candidates as labels and markers for (bio)-imaging and sensing applications.
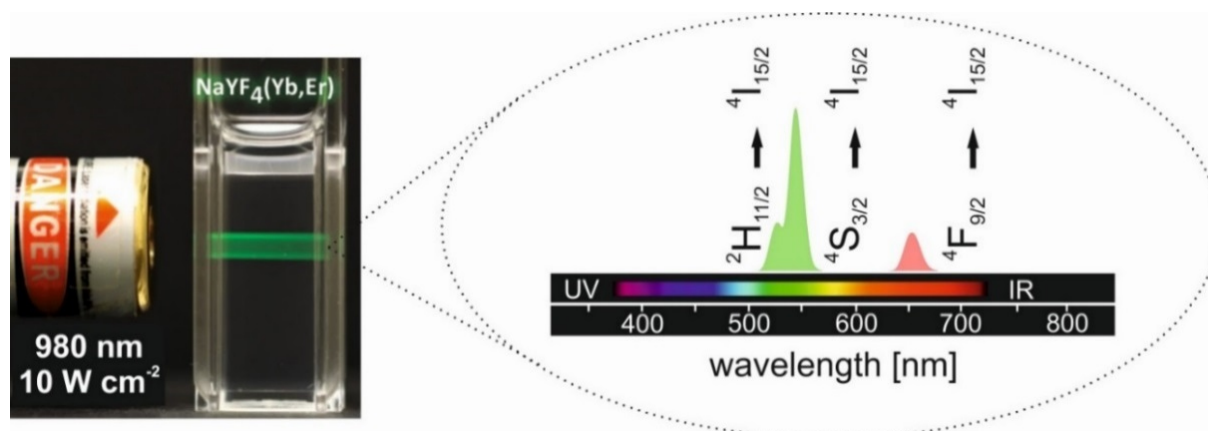
Figure 4 | Left: Colloidal dispersion of oleate-coated β-NaYF$_4$(Yb^{3+}/Er^{3+}) UCLNPs in cyclohexane displaying predominantly green luminescence upon 980 nm CW laser excitation (10 W·cm^{-2}). Right: Corresponding upconversion luminescence spectrum exhibiting two distinct emission peaks in the green and red spectral region. Related electronic transitions are indicated.
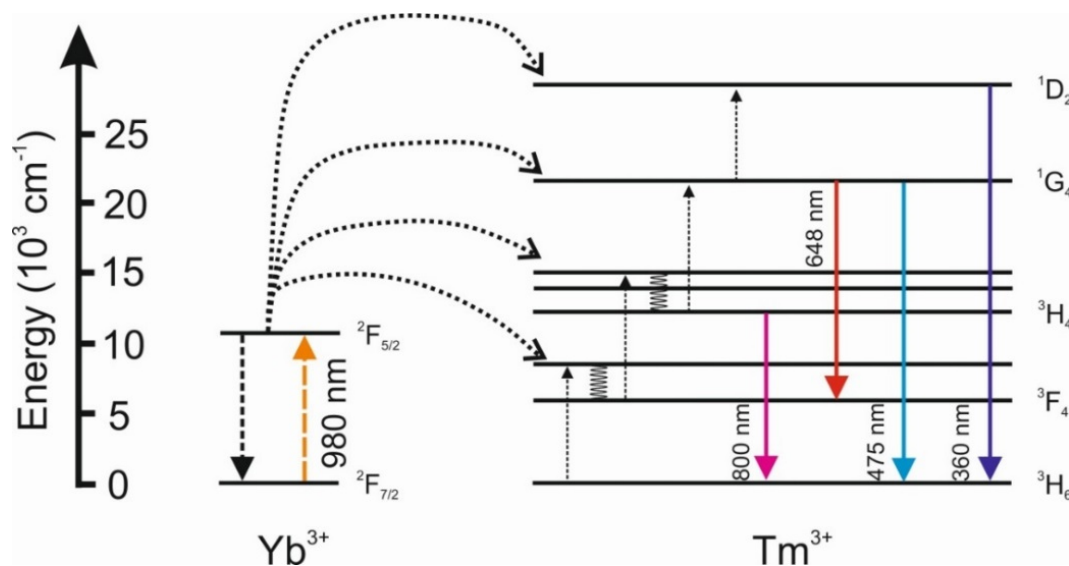
Scheme 3 | Energy level diagram and energy transfer upconversion (ETU) mechanisms for a Yb^{3+}/Tm^{3+}-doped (sensitizer/activator) system. Excitation light (980 nm) is absorbed by Yb^{3+} sensitizer ions and sequentially transferred to Tm^{3+} activator ions leading to multicolor upconversion luminescence spanning from the UV to NIR. Arrows indicate radiative, non-radiative energy transfer, and multiphonon relaxation processes.
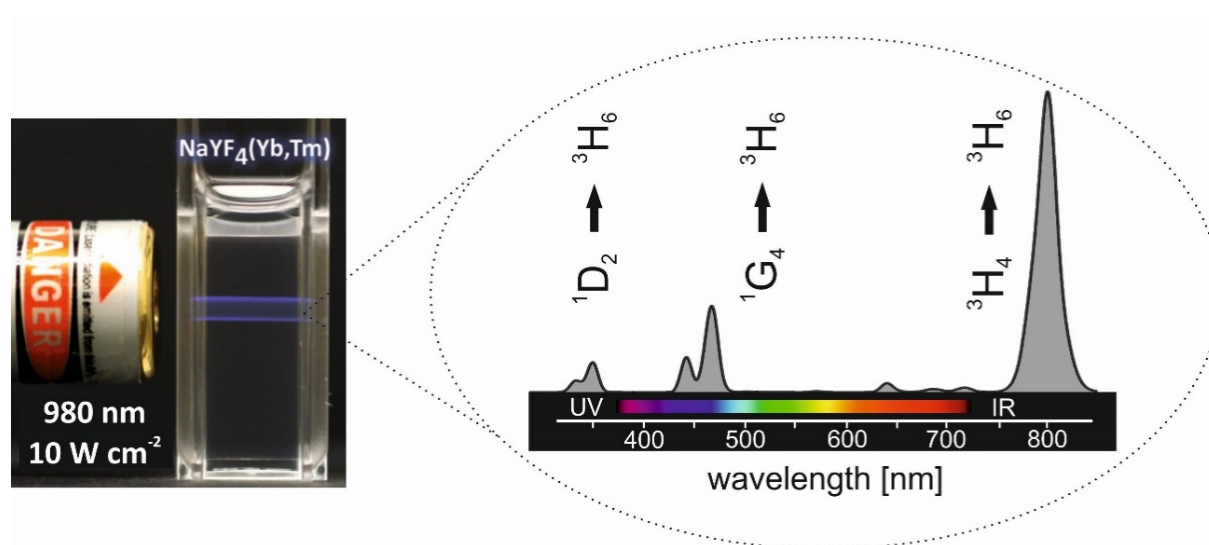
Figure 5 | Left: Colloidal dispersion of oleate-coated β-NaYF$_4$(Yb^{3+}/Tm^{3+}) UCLNPs in cyclohexane displaying predominantly blue luminescence upon 980 nm CW laser excitation (10 W·cm^{-2}). Right: Corresponding upconversion luminescence spectrum exhibiting distinct emission peaks in the UV, visible, and NIR. Related electronic transitions are indicated.

1.4.3.   Synthesis Strategies

In general, there are three main components of upconversion (nano)-phosphors one should carefully consider in order to obtain efficient upconversion luminescence: (a) The inorganic host material and its crystal structure. The type and the concentration of (b) sensitizer ions, and (c) activator ions. Synthesis methods for the fabrication of UCLNPs have been developed during the last decade in order to meet all of these criteria. These methods include co-precipitation [146,147], hydro(solvo)thermal methods [148], thermal decomposition [149,150], and ionic liquids-based synthetic strategies [151,152]. The most widely used methods for the synthesis of UCLNPs are hydro(solvo)thermal based strategies and thermal decomposition procedures.

The hydrothermal/solvothermal method is a typical solution-based bottom-up approach. For the synthesis of lanthanide-doped NaYF$_4$ UCLNPs rare-earth and fluoride precursors (*e.g.* rare-earth chlorides, nitrates, or oxides; HF, NH$_4$F, or NaF), solvents and certain surfactants (*e.g.* ehtylenediamine tetraacetic acid; cetyltrimethylammonium bromide; or oleic acid) are mixed. Educts are heated in a sealed autoclave above the critical point of the solvent, which increases the solubility and reactivity of the reactants. The optimization of the

synthesis parameters of this method is generally very time-consuming since the reaction times are long (up to several days). Therefore, it is difficult to synthesize high quality UCLNPs in terms of phase crystallinity and purity, particle size distribution, and particle shape [153]. Another disadvantage is that specialized reaction vessels (autoclave) are required, which makes it impossible to observe and control the nanocrystal growth during the synthesis.

An alternative synthesis strategy is the thermal decomposition of metal trifluoroacetates in solvent mixtures of oleic acid (OA) and 1-octadecene at temperatures of ~ 320 °C to corresponding metal fluorides. During the synthesis, nucleation of metal fluorides takes place, followed by the growth of nuclei into nanocrystals. These crystals are covered by oleic acid molecules which act as surfactants preventing their agglomeration. In 2006, Chow *et al.* reported on the synthesis of hexagonal $NaYF_4$ UCLNPs doped with Yb^{3+} and Er^{3+} ions using a thermal decomposition strategy [154]. This method allows for the production of high quality UCLNPs based on lanthanide-doped β-$NaYF_4$ with very narrow size distribution. However, expensive and toxic metal precursors are used and toxic byproducts such as trifluoroacetic anhydride, trifluoroacetyl fluoride, carbonyl difluoride, tetrafluoroethylene, or hydrogen fluoride are produced [132].

However, one general drawback of all synthesis strategies is their batch-to-batch irreproducibility. This means that each batch of UCLNPs has its own particle size, size distribution, doping concentration, arrangement of dopant ions within the crystalline host lattice, and number of surface ligands, which in summary results in slightly different optical properties [155,156]. Therefore, a scale up strategy in order to produce identical UCLNPs of high quality on a large batch is highly desirable, especially since most protocols deal with the synthesis of only a small amount of UCLNPs per batch (~ 1 mmol of lanthanide precursors resulting in ~ 100 mg of UCNLPs).

1.4.4.   Surface Modifications

Since most of the commonly used UCLNPs are synthesized using oil-phase based strategies with oleic acid or oleylamine molecules acting as surfactants, these NPs have neither intrinsic water dispersibility nor functional groups for further conjugation to biomolecules. Hence, post-synthesis methods for surface engineering are required which render UCLNPs

dispersible in aqueous media and colloidally stable under physiological conditions. Moreover, surface coatings should provide functional anchors for further bioconjugation to proteins, antibodies, DNA, *etc*. and make NPs biocompatible. Frequently used methods including silica coating (see Figure 6), ligand exchange, ligand oxidation, Layer-by-Layer coating, and coating by amphiphilic molecules and polymers have been recently summarized in several review articles [157,158,159,160]. TEM images of UCLNPs before and after silica coating are shown in Figure 6.
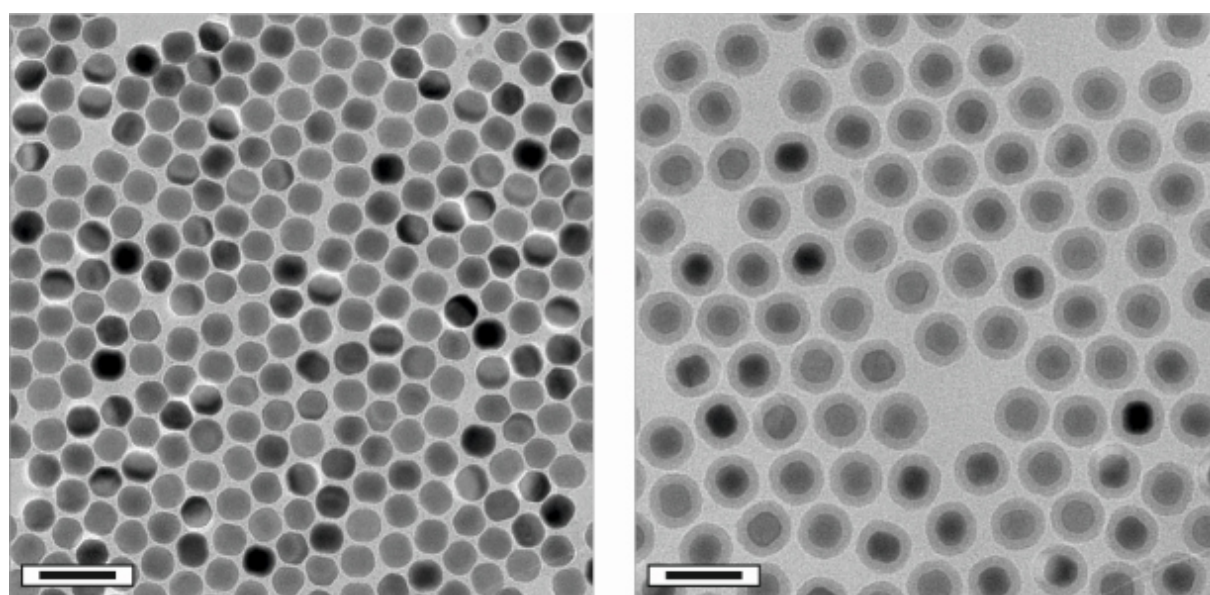
Figure 6 | TEM images of lanthanide-doped NaYF$_4$ UCLNPs before (left) and after (right) silica coating. The uniform silica shell (~ 5 nm in thickness) can be clearly distinguished from the NaYF$_4$ core, since it exhibits a different electron optical contrast. Scale bars indicate 60 nm.

1.4.5. Toxicity

The investigation of cytotoxic effects of UCLNPs is an important task for biomedical applications. In 2008, Shan *et al.* reported a study of *in vitro* cytotoxicity of silica-coated UCLNPs. Here, hydrophilic UCLNPs were incubated with human osteosarcoma cells. The results showed that silica-coated UCLNPs (concentration 1 mg·mL^{-1}) functionalized with amine and carboxyl groups have low cytotoxicity in comparison to the control group. Further studies using different human and animal cell lines confirmed no severe adverse effects that

can be directly related to UCLNPs [161,162,163,164,165]. The long-term *in vivo* bio-distribution of UCLNPs was investigated by Xiong *et al.* in 2010. Results of toxicity studies indicated that mice intravenously injected with 15 mg·kg^{-1} of polyacrylic acid-coated UCLNPs survived for 115 days without any evident (observational, histological, hematological and biochemical) toxic effects. UCLNPs were found to mainly accumulate in the liver and spleen [163]. These examples demonstrate the low toxicity of UCLNPs.

This chapter described some of the basic aspects of UCLNPs with emphasis on their composition, photophysical properties, synthesis, surface modifications, and toxicity. In recent years, the number of proof-of-concept reports using UCLNPs as markers for (bio)-imaging or as donors for Förster resonance energy transfer (FRET) based sensing greatly increased [166,167,168,169]. All of these papers employ UCLNPs because of their unique optical characteristics (*e.g.* NIR excitation; multicolor anti-Stokes emissions; long luminescence lifetimes in the µs or ms regime). However, only a few reports investigate the photophysical properties of UCLNPs such as quantum yield, emission lifetimes, ratio of luminescence peaks, *etc.*, which is of fundamental importance in order to fully exploit their potential for sensing and imaging applications. It is well known that photophysical properties of UCLNPs are strongly dependent on the excitation power density. Unfortunately, reports dealing with the photophysical characterization of hydrophilic UCLNPs dispersed in aqueous media are still missing.

2.   Motivation and Aim of the Work

UCLNPs offer unique optical properties. They are capable of emitting anti-Stokes-shifted luminescence upon NIR excitation. This is of great advantage in comparison to commonly used luminescent labels and probes which are excited by UV or visible light. The utilization of NIR rather than UV or visible radiation maximizes the penetration depth of the excitation light into biological tissue and simultaneously minimizes photodamage of biological specimens. Moreover, the detection sensitivity is greatly improved since NIR excitation does not induce background autofluorescence resulting in excellent signal-to-noise ratio.

Within this work a bottom-up synthesis protocol should be established which allowed for the size-controlled preparation of bright UCLNPs. It is well known from *in vivo* experiments that NPs with hydrodynamic diameters smaller than ~ 10 nm are rapidly cleared by the kidneys or taken up by the liver. In contrast, NPs exhibiting diameters larger than ~ 150 nm are filtered out by the spleen [170]. Therefore, the aim was to synthesize small (< 50 nm) UCLNPs with narrow size distribution.

The control of surface chemistry is important in order to offer colloidal stability of NPs in biological media. Proper surface engineering which allows for further functionalization of UCLNPs is an indispensable prerequisite for providing them to (bio)-analytical applications. Thus, the aim of this work was to tailor UCLNPs for protein binding and labelling. In a second (bio)-analytical application the potential of UCLNPs for luminescence-controlled monitoring of enzymatic reactions upon NIR excitation should be evaluated. Up to now there is only little known about the influence of the surface coating on the photophysical properties of UCLNPs. Hence, one task of this work was to systematically investigate different surface modifications in terms of their impact on the upconversion luminescence.

3.   Multicolor Upconversion Nanoparticles for Protein Conjugation

3.1.   Abstract

The preparation of monodisperse, lanthanide-doped hexagonal-phase $NaYF_4$ upconverting luminescent nanoparticles for protein conjugation is described. Their core was coated with a silica shell which then was modified with a poly(ethylene glycol) spacer and N-hydroxysuccinimide ester groups. The nanoparticles were characterized by transmission electron microscopy, Raman spectroscopy, X-ray powder diffraction, and dynamic light scattering. The N-hydroxysuccinimide ester functionalization renders them highly reactive towards amine nucleophiles (*e.g.* proteins). Such particles can be conjugated to proteins. The protein-reactive UCLNPs and their conjugates to streptavidin and bovine serum albumin display multicolor emissions upon 980 nm continuous wave laser excitation. Surface plasmon resonance studies were carried out to prove bioconjugation and to compare the affinity of the particles for proteins immobilized on a thin gold film.

This chapter has been published.

Author contributions

SW synthesized and characterized the nanoparticles; performed conjugation experiments; wrote the manuscript. SW and TH performed SPR measurements. WMP performed Raman measurements. ES and TM were involved in discussing the results. OSW supervised the project and is corresponding author.

3.2.   Introduction

The implementation of nanotechnology to healthcare holds great promise in areas such as imaging [90,95,168,171,172,], faster diagnosis [173], targeting [174], drug delivery [175], and tissue regeneration [176], as well as the development of medical products [177,178,179]. The chemical synthesis of nanoparticles (NPs) has been studied in detail during the last decade [180,181,182,183]. Substantial efforts have been made to control the dimensions, shape, composition, particle size distribution, *etc.*, of NPs, thereby creating new materials with size dependent electrical, optical, magnetic, catalytic, and chemical properties, which cannot be achieved by their bulk counterparts. Important classes of NPs are a) magnetic NPs, b) gold NPs, c) quantum dots, d) silica NPs, *etc.* [184,185,186,187,188,189,190]. In recent years, upconverting luminescent nanoparticles (UCLNPs) joined this classification. Photon upconversion has been researched ever since the 1960s. It is a process where two or more photons are sequentially absorbed, resulting in the emission of light at a shorter wavelength than the excitation light. For instance, infrared or near-infrared (NIR) light can be converted to shorter-wavelength radiation, usually in the visible range of the electromagnetic spectrum (anti-Stokes type emission) [191].

The mechanisms behind photon upconversion were first investigated in lanthanide-doped bulk materials by Auzel, Ovsyankin, and Feofilov [116]. In a sensitizer-activator system, the excitation energy is absorbed by a sensitizer ion (*e.g.* Yb^{3+}) and transferred to an activator ion (*e.g.* Er^{3+} or Tm^{3+}) *via* a non-radiative, resonant energy transfer process. Metastable, long-lived energy states are required, in which case energy transfer upconversion (ETU) is possible, where the combined energies of pump photons are stored, which can lead to the emission of a higher energy photon [192].

Anti-Stokes emissions from UCLNPs offer several advantages over conventional Stokes-shifted emissions from a) semiconductor quantum dots, b) organic- and protein-based fluorophores, and c) the multiphoton process employing fluorescent dyes. UCLNPs are very attractive phosphors in terms of bioimaging due to their non-blinking emission and remarkable photostability [145,193,194]. In biological samples or tissue, there is minimal excitation of autofluorophores, since UCLNPs are usually excited by NIR (980 nm) continuous wave (CW) laser light. This scheme enables luminescence to be imaged with a

high signal to noise ratio, minimizes possible photodamage in biological systems, and allows deeper tissue penetration [169,195]. Upconversion microparticles have been used before in immunoassays [196], and enzyme activity assays [197], but their size (1 – 10 µm) and large size distribution makes their use less attractive. With respect to the relative size of a protein and upconversion *micro*particles, one may not speak of a label in its classical sense.

High-quality UCLNPs (with respect to crystal phase, monodispersity, geometry, *etc.*) are usually synthesized in high-boiling organic solvents (*e.g.* 1-octadecene) using ligand molecules with long alkyl chains (*e.g.* oleic acid), which renders them inherently functionalized with hydrophobic alkyl groups and only dispersible in non-polar organic solvents such as toluene, hexane, and the like [198,199]. In order to make them amenable to (bio)-analytical applications, surface modification is required, to make the UCLNPs water dispersible, offering a platform for further conjugation of functional chemical groups and/or (bio)-molecules. Silica is known for its biocompatibility [200], and silica coating of UCLNPs therefore offers an attractive way of functionalization [201,202]. This has already been applied to a multitude of nanoparticle systems, including gold and silver NPs [203], magnetic NPs [204], and quantum dots [205]. In addition, silica coating is a flexible coating technique that is applicable to both hydrophilic and hydrophobic NPs [206,207,208]. The coating process of hydrophilic NPs relies on the Stöber method, while a reverse-microemulsion method is typically used for coating hydrophobic NPs [128].

We describe the synthesis of protein-reactive, multicolor UCLNPs. First, monodisperse, lanthanide-doped hexagonal-phase $NaYF_4$ nanoparticles were prepared, which were coated with oleic acid, as can be seen in Scheme 4. In the second step, the particles were silica coated using a reverse-microemulsion method, and subsequently functionalized with an amino-reactive silanization reagent. This reagent consists of a triethoxysilane conjugated to a poly(ethylene glycol) spacer (PEG) and a carboxyl group activated with an N-hydroxysuccinimide (NHS) ester. The NHS ester of the silica-coated UCLNPs renders them highly reactive towards proteins. The protein-reactive UCLNPs exhibit multicolor luminescence emission after 980 nm laser excitation. Finally, surface plasmon resonance (SPR) studies were carried out to study the binding affinity of NHS-activated nanoparticles to proteins that previously were immobilized on a gold film.
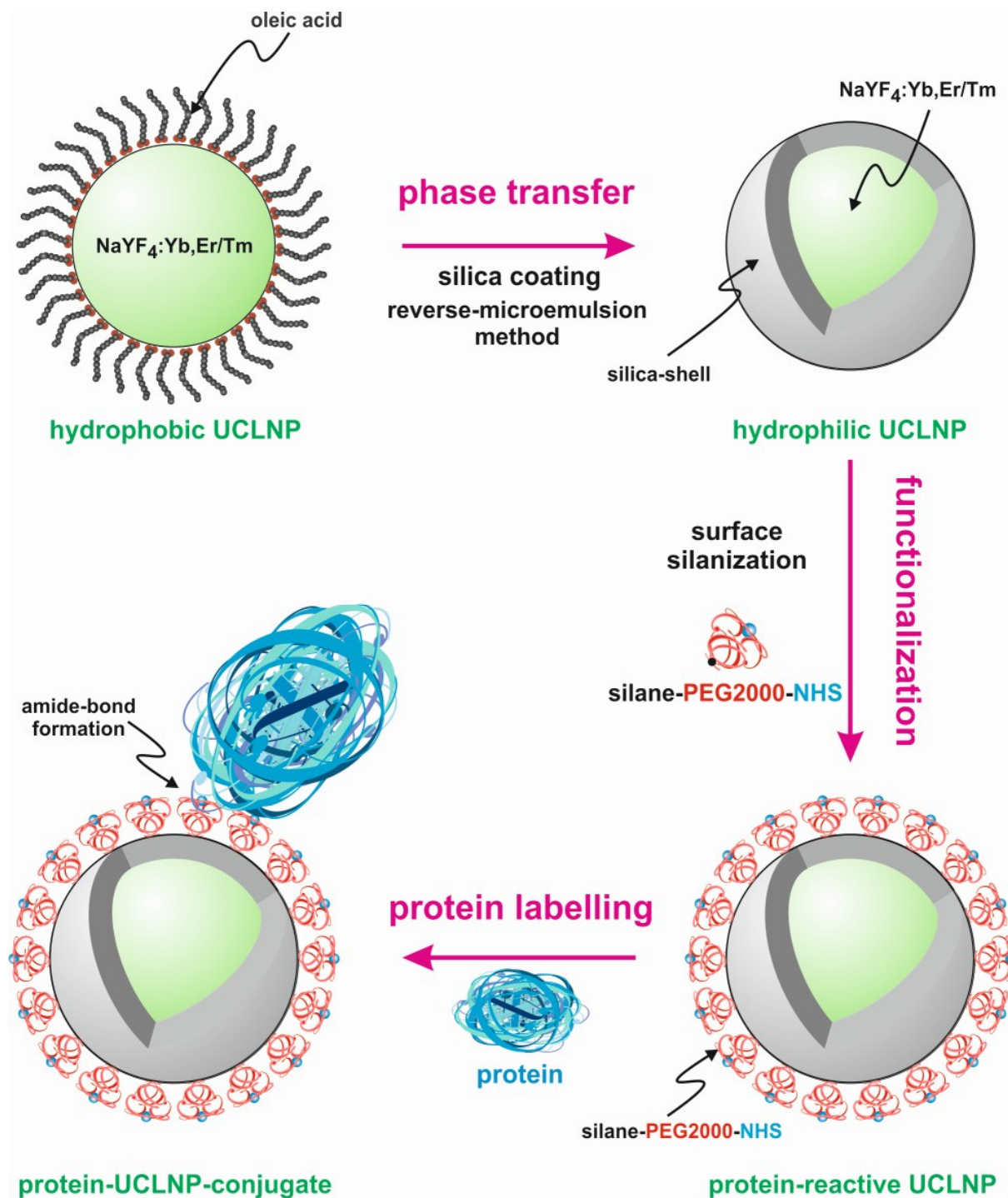
Scheme 4 | Surface engineering (including phase transfer, functionalization, and protein labelling) of initially hydrophobic UCLNPs towards protein-reactive, multicolor upconverting labels.

3.3.   Materials and Methods

3.3.1.   Chemicals

Yttrium(III) chloride hexahydrate (99.99 %), ytterbium(III) chloride hexahydrate (99.9 %) erbium(III) chloride hexahydrate (99.9 %), thulium(III) chloride hexahydrate (99.99 %), ammonium fluoride (ACS reagent ≥ 98.0 %), sodium hydroxide (reagent grade ≥ 98.0 %) , Igepal® CO-520, tetraethyl orthosilicate (TEOS), bovine serum albumin (BSA) fraction V (purity > 96 %), 16-mercapto-hexadecanoic acid (95 %), N-(3-dimethylaminopropyl)-N'-ethylcarbodiimide hydrochloride (EDC) commercial grade, and sodium chloride (p.A.) were purchased from Sigma-Aldrich (www.sigmaaldrich.com), oleic acid (technical grade 90 %) and 1-octadecene (technical grade 90 %) from Alfa Aesar (www.alfa.com), triethoxysilane poly(ethylene glycol) 2000 succinimidyl ester from Nanocs (www.nanocs.com), ammonia solution (32 %), 2-propanol (p.A.), 2-amino-2-hydroxymethyl-propane-1,3-diol (TRIS, molecular biology grade), from Merck (www.merckgroup.com), sodium hydrogen carbonate (p.A.) from Ferak (www.ferak.de), ethanol (p.A.) from Roth (www.carlroth.de), and streptavidin-modified magnetic beads (PureProteome™) from Millipore (www.millipore.com). All other reagents and organic solvents were of the highest grade available.

3.3.2.   Instrumentation

Transmission electron microscopy (TEM) was performed using a 120 kV Philips CM12 (www.fei.com) microscope. Samples were prepared by dropping colloidal dispersions (~ 10 µL) on carbon-coated copper grids (400 mesh) from Plano (www.plano-em.de) and subsequent evaporation of the solvent. Upconversion luminescence spectra were recorded using a luminescence spectrometer (LS 50 B) from Perkin Elmer (www.perkinelmer.com), modified with a 980 nm CW laser (120 mW, ~ 15 W·cm^{-2}) from Roithner (www.roithner-laser.com) for upconversion photo-excitation. All centrifugation steps were carried out in a Hettich Universal 320 centrifuge (www.hettichlab.com). Raman spectroscopy was performed using a DXR Raman microscope from Thermo Scientific (www.thermoscientific.com) with 532 nm CW laser excitation (8 mW). The Zetasizer Nano ZS from Malvern

(www.malvern.com) was used for dynamic light scattering (DLS) experiments. X-ray powder diffraction (XRD) patterns with a resolution of 0.02° (2θ) were collected using a Stoe Stadi P diffractometer (www.stoe.com) with a Cu source (Kα radiation, λ=1.54060 Å) operating at 40 kV and 42 mA. All SPR experiments were performed using a Biosuplar 6 instrument from Mivitec GmbH, (www.biosuplar.com). Typically, glass slides covered by a 50 nm thick gold film were used, and intensity measurements were performed at constant angle. The signal intensity was calibrated in refractive index units (RIU) with solutions of sodium chloride of different concentrations and known refractive index.

3.3.3. Synthesis of Hydrophobic β-NaYF₄ Nanoparticles doped with Yb³⁺/Er³⁺ or Yb³⁺/Tm³⁺ ions

Two systems of hydrophobic, lanthanide-doped $NaYF_4$ nanocrystals were prepared *via* a modified procedure as reported by Zhang *et al.* [209]. For the first system $YCl_3 \cdot 6H_2O$ (0.747 mmol), $YbCl_3 \cdot 6H_2O$ (0.25 mmol), $TmCl_3 \cdot 6H_2O$ (0.003 mmol) were employed. In the second system $YCl_3 \cdot 6H_2O$ (0.78 mmol), $YbCl_3 \cdot 6H_2O$ (0.20 mmol), $ErCl_3 \cdot 6H_2O$ (0.02 mmol) were used. The salts were dissolved in approximately 5 mL of methanol by sonication. The respective clear and optically transparent solution of rare earth chlorides in methanol was transferred into a 50 mL flask, mixed with 8 mL of oleic acid and 15 mL of 1-octadecene under an atmosphere of nitrogen and heated to 160 °C. A homogeneous, clear solution was formed after 30 minutes at 160 °C under vacuum. The reaction mixture was then cooled to room temperature and 10 mL of methanol containing NaOH (0.25 M) and NH_4F (0.4 M) were added at once. The colloidal dispersion was heated to 120 °C and stirred for 30 minutes. The resulting colloid was refluxed at approximately 325 °C for 15 minutes. After cooling to room temperature, the UCLNPs were precipitated by addition of approximately 20 mL of ethanol and isolated *via* centrifugation at a relative centrifugal force (RCF) of 1000 g for 5 minutes. The pellet was washed several times by dispersing it in small amounts (approximately 0.5 mL) of chloroform and cyclohexane, then precipitating them by the addition of a large excess (approximately 15 mL) of ethanol and acetone. A white solid was obtained, which can be easily re-dispersed in cyclohexane to form a clear dispersion. This was used for further silica coating.

3.3.4.   Silica Coating of Hydrophobic UCLNPs

The surface of hydrophobic UCLNPs was coated with silica using a modified reverse-microemulsion technique [200]. First, 10 mg of the UCLNPs were dispersed in 10 mL of cyclohexane in a 25 mL round bottom flask. Then, 500 µL of Igepal® CO-520 and 80 µL of an aqueous ammonia solution (32 %) were added. This yielded a clear and stable emulsion after 30 minutes of sonication, which was supplemented with 60 µL (0.2 mmol) of TEOS and kept for 24 hours at room temperature under magnetic stirring (600 rpm). Silica-coated UCLNPs were collected *via* centrifugation (RCF: 3000 g; 5 minutes). Three cycles of re-dispersion and centrifugation were performed to wash the pellet with an ethanol/water mixture (1:1 v/v). Nanoparticles were filtered through a syringe filter with a pore size of 200 nm and stored in ethanol.

3.3.5.   Functionalization of Silica-coated UCLNPs

A fresh solution of 10 mg of triethoxysilane poly(ethylene glycol) 2000 succinimidyl ester in 500 µL of ethanol was added to a dispersion of 3 mg of silica-coated UCLNPs in 200 µL ethanol. The mixture was magnetically stirred for 2 hours at room temperature. The succinimidyl-functionalized UCLNPs were collected *via* centrifugation (RCF: 17000 g; 10 minutes), and the unreacted materials were washed away with cold distilled water. Thereafter, the succinimidyl-functionalized UCLNPs were stored in 2-propanol at 4 °C.

3.3.6.   Conjugation of Succinimidyl-functionalized UCLNPs to Streptavidin-Modified Magnetic Beads

An aliquot (100 µL) of a dispersion of the magnetic beads was placed in a micro-centrifuge tube. The magnetic beads were collected with a permanent magnet and washed two times with a hydrogen carbonate buffer (HCB) solution (0.1 M) adjusted to pH 9 with 1 M NaOH. After washing, the magnetic beads were dispersed in 500 µL of HCB. In parallel, 1 mg of succinimidyl-functionalized UCLNPs in 500 µL of 2-propanol was collected *via* centrifugation (RCF: 17000 g; 10 minutes). The supernatant was discarded and 500 µL of

HCB were added to the pellet. An optically transparent dispersion was obtained after sonication. The dispersions of streptavidinylated magnetic beads and protein-reactive UCLNPs were combined and magnetically stirred at room temperature for 2 hours. The streptavidin-modified magnetic bead UCLNPs conjugate was collected with a permanent magnet and washed two times with HCB.

3.3.7. Conjugation of Succinimidyl-functionalized UCLNPs to Bovine Serum Albumin

A self-assembled monolayer of a carboxyl-terminated alkane thiol was prepared by immersing a gold glass slide overnight in a solution of 16-mercapto-hexadecanoic acid (400 µM) in ethanol. The protein (BSA) was bound to this surface *via* EDC coupling [210]. First, 20 mg of BSA were dissolved in 10 mL aqueous NaCl solution (140 mM). Second, 480 mg of EDC were added and mixed by vortexing. This solution was applied to the SPR chip. The binding of BSA to the activated carboxyl groups was monitored in real time by SPR. Changes in the intensity of the reflected light were recorded at constant angle. An increase in the intensity of the SPR signal over time indicated binding of BSA. Saturation had occurred after approximately 30 minutes. The chip was washed with a solution of sodium chloride (140 mM). Again, BSA together with EDC was loaded onto the chip. Only a slight increase in the signal could be observed. After washing, the signal returned to the starting values (prior to the second immobilization). This indicates that surface modification with BSA was successful. Next, the solution in the SPR cell was changed to HCB. When the signal reached a constant value, protein-reactive UCLNPs (1 mg·mL^{-1}) in HCB were added. After 80 minutes, no significant increase in the SPR signal was observed. Washing steps with hydrochloric acid (0.1 M) for 10 minutes and with HCB for 10 minutes led to a decrease in the signal by approximately 20 %.

3.4.   Results and Discussion

3.4.1.   Synthesis and Characterization

Hydrophobic $NaYF_4$ nanoparticles doped with Yb^{3+}/Er^{3+} and Yb^{3+}/Tm^{3+} possess good monodispersity and hexagonal crystal phase. They were prepared *via* a modification of a known method [209]. Doping concentrations of lanthanide ions are 20/2 mol% for doping with Yb^{3+}/Er^{3+}, and 25/0.3 mol% for doping with Yb^{3+}/Tm^{3+}. Lanthanide-doped β-phase $NaYF_4$ displays superior brightness compared to other host materials [118], which is about one order of magnitude better than comparable cubic α-phase $NaYF_4$ UCLNPs [209,211]. Upconversion luminescence spectra of corresponding Yb^{3+}/Er^{3+} and Yb^{3+}/Tm^{3+}-doped samples acquired from dispersions in cyclohexane are displayed in Figure 7. Under 980 nm CW laser excitation (~ 15 W·cm^{-2}), the β-$NaYF_4$(20 % Yb^{3+}/2 % Er^{3+}) nanocrystals yield three distinct emission peaks at 522 nm, 541 nm, and 655 nm. These are assigned to the $^4H_{11/2}$ - $^4I_{15/2}$, $^4S_{3/2} - ^4I_{15/2}$, and $^4F_{9/2} - ^4I_{15/2}$ transitions of Er^{3+} ions, respectively [128].

The upconversion spectrum of β-$NaYF_4$(25 % Yb^{3+}/0.3 % Tm^{3+}) displays two blue emission peaks (450 nm and 475 nm), which correspond to the $^1D_2 - ^3F_4$ and $^1G_4 - ^3H_6$ transitions of the Tm^{3+} ions, respectively. Additionally, there are two weaker peaks at 646 nm ($^3F_2 - ^3F_3$) and 696 nm ($^3H_6 - ^1G_4$) [128]. Predominant blue and green emissions of optically transparent colloidal dispersions of corresponding multicolor nanoparticles in cyclohexane upon 980 nm CW laser excitation (~ 10 W·cm^{-2}) can be seen in Figure 7. It shall be mentioned here that the luminescence of UCLNPs strongly depends on temperature and, in fact, has been used to sense it on a nanoscale [212].

Dispersions of UCLNPs in cyclohexane exhibit very good colloidal stability. No sedimentation or agglomeration was found even after several weeks. Dynamic light scattering (DLS) experiments performed at 25 °C with a 632.6 nm laser and a non-invasive backscatter technique confirmed this observation. The average hydrodynamic diameter of Yb^{3+}/Er^{3+}-doped nanoparticles is 34.4 nm, with a full width at half maximum (FWHM) of 5 nm, this yielding a polydispersity index (PI) of 0.072. The respective values of Yb^{3+}/Tm^{3+}-doped UCLNPs are 31.8 nm for the diameter, 5.3 nm FWHM, and a PI of 0.048. Excellent correlation statistics and fits (data not shown) were obtained using a non-negative least squares analysis algorithm.
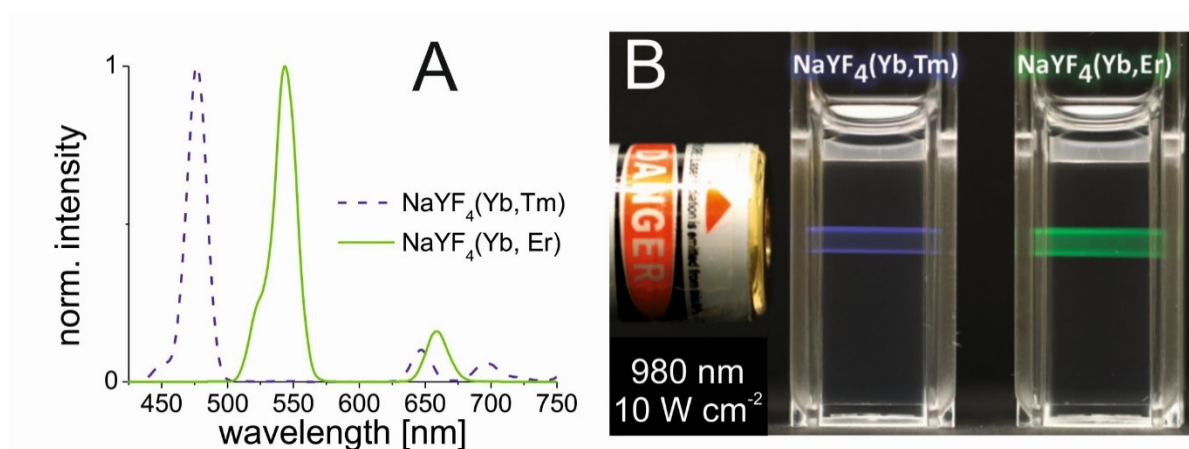
Figure 7| (**A**) Normalized upconversion luminescence spectra of Yb^{3+}/Tm^{3+} (dashed blue line) and Yb^{3+}/Er^{3+}-doped (solid green line) multicolor β-$NaYF_4$ nanocrystals. UCLNPs were dispersed in cyclohexane (1 mg/mL) and excited by a 980 nm CW laser (~ 15 W·cm^{-2}). (**B**) Digital photograph of optically transparent colloidal dispersions of corresponding UCLNPs (1 mg/mL) in cyclohexane. The predominant blue and green emissions of Yb^{3+}/Tm^{3+} and Yb^{3+}/Er^{3+}-doped UCLNPs upon 980 nm CW laser excitation (~ 10 W·cm^{-2}) can easily be seen by the bare eye.

TEM images of corresponding nanocrystals are shown in Figure 8. A dispersion of UCLNPs in cyclohexane was dried on a carbon-coated copper grid. The roughly spherical nanoparticles form a 2D hexagonal closed packing, as can be seen from the TEM images. This behavior may be due to van-der-Waals interaction of oleic acid (OA) molecules on the particles' surface and the solid carbon support of TEM grids. The average particle diameters as determined *via* TEM are 27 nm for the Yb^{3+}/Er^{3+}-doped sample and 25 nm for the Yb^{3+}/Tm^{3+}-doped sample. These results are in good agreement with the DLS data, since DLS experiments take account of the hydrodynamic diameter of the particles rather than their sheer particle size.

The results of XRD crystal phase analyses are shown in Figure 8, and demonstrate the high crystallinity of UCLNPs. XRD patterns of the two samples of nanocrystals are in good agreement with the standard pattern of β-$NaYF_4$ (ICDD PDF #16-334). Raman spectroscopy was used to characterize the phonon bands of $NaYF_4$ nanocrystals (see Figure 9). They are clearly visible and distinct between 225-450 cm^{-1}. The weighed average of the phonon modes is 304 cm^{-1} for the Yb^{3+}/Er^{3+}-doped sample, and 320 cm^{-1} for the Yb^{3+}/Tm^{3+}-doped sample. This phonon energy is considerably lower than

that of comparable fluoride host lattices such as LiYF$_4$ (570 cm^{-1}) [213,214]. Additionally, it is predictably lower than that of bulk, un-doped NaYF$_4$ (360 cm^{-1}) [215] due to the modified phonon density of states [216].
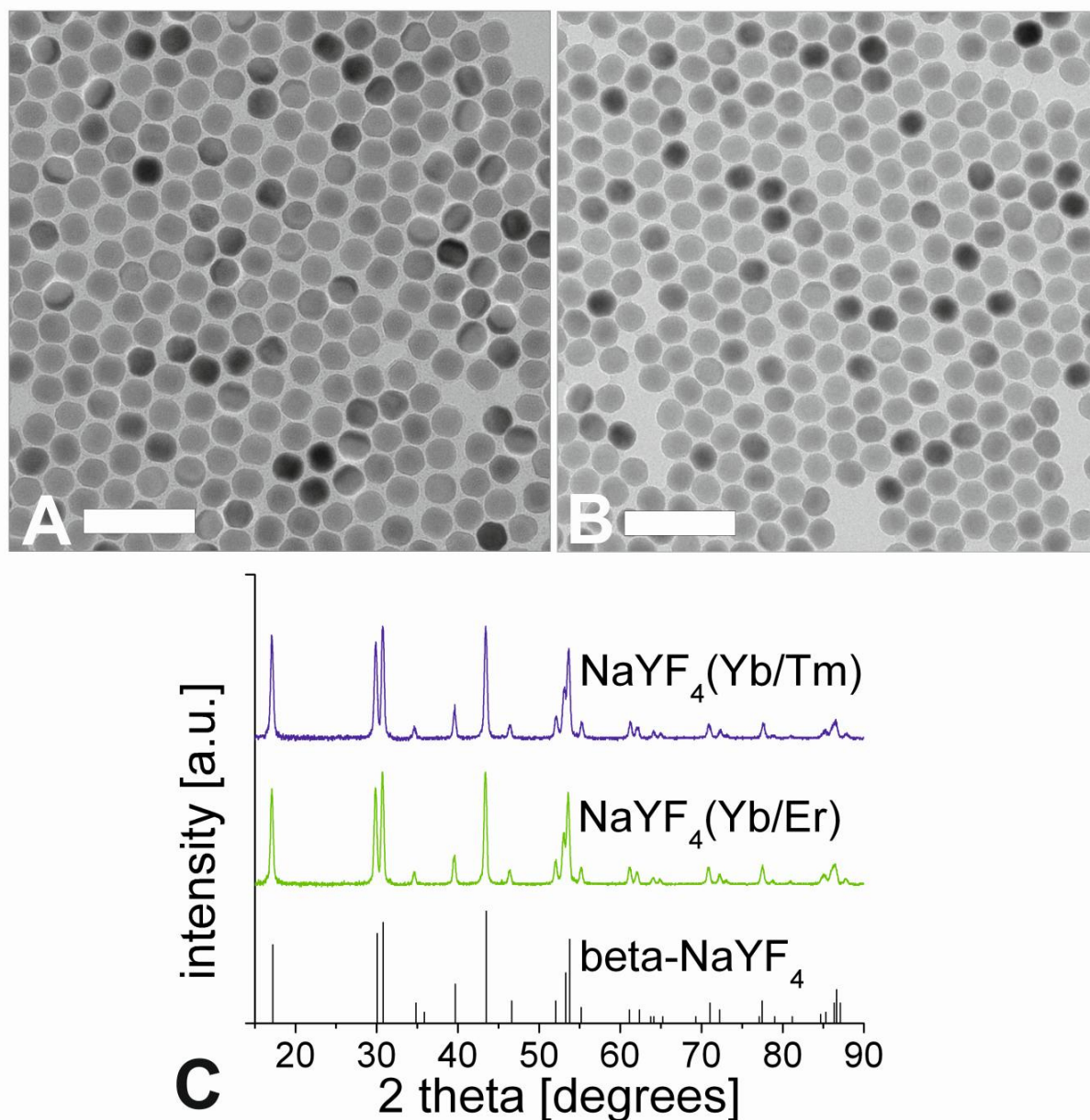
Figure 8| TEM images of NaYF$_4$(20 % Yb^{3+}/2 % Er^{3+}) (**A**) and NaYF$_4$(25 % Yb^{3+}/0.3 % Tm^{3+}) (**B**) upconversion luminescent nanoparticles, respectively. Scale bars indicate 100 nm. Graph (**C**) shows corresponding XRD patterns and the standard XRD pattern of β-NaYF$_4$ (ICDD PDF #16-334).

Oleic acid has a distinct Raman spectrum in the 2830-2960 cm^{-1} region where CH$_2$ stretching modes are observed. These are particularly susceptible to thermal changes, and slight spectral variations are expected from sample to sample for this reason [217]. Raman spectra for this spectral region are shown in Figure 9. Additional evidence of the presence of OA is exhibited by the strong CH$_2$ scissoring modes in the 1438-1456 cm^{-1} region (not shown here). Other (but much weaker) Raman peaks for oleic acid can be observed in the 600-1800 cm^{-1} region.
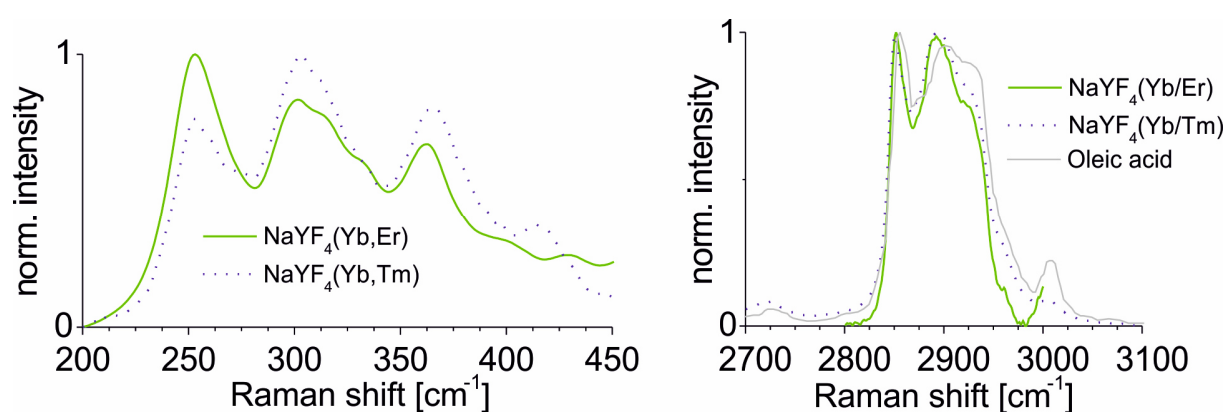
Figure 9 | Raman spectra of UCLNPs focusing on the NaYF$_4$ phonon region (**A**), and the CH$_2$ stretching corresponding to the functionalized OA (**B**). The dotted blue line corresponds to Yb^{3+}/Tm^{3+}-doped sample and the solid green line to Yb^{3+}/Er^{3+}-doped UCLNPs. The Raman spectrum of pure, non-functionalized OA (solid grey line) is shown in (**B**) for comparison. The slight peak shifts and difference in peak widths between the non-functionalized OA and the OA-functionalized UCLNPs indicate that OA is likely to be bound to the surface of UCLNPs.

3.4.2.   Surface Engineering

Hydrophobic, oleic acid-coated UCLNPs were then silica coated *via* a reverse-microemulsion technique according to a modified literature method [200]. This makes them water dispersible and biocompatible, which is a prerequisite for almost any (bio)-applications. TEM images in Figure 10 demonstrate that this technique yields a thin and uniform silica coating on the hydrophobic nanoparticles. The formation of a silica shell can be clearly deduced from the TEM images, because silica exhibits an electron optical contrast which is quite different from that of rare earth-doped nanocrystals. The size of Yb^{3+}/Er^{3+}-doped nanoparticles increased from 27 nm to 38 nm after silica coating, implying a shell thickness of approximately 5 nm.

The diameter of respective Yb^{3+}/Tm^{3+}-doped particles increased from 25 nm to 38 nm, and this corresponds to a shell thickness of about 6 nm.
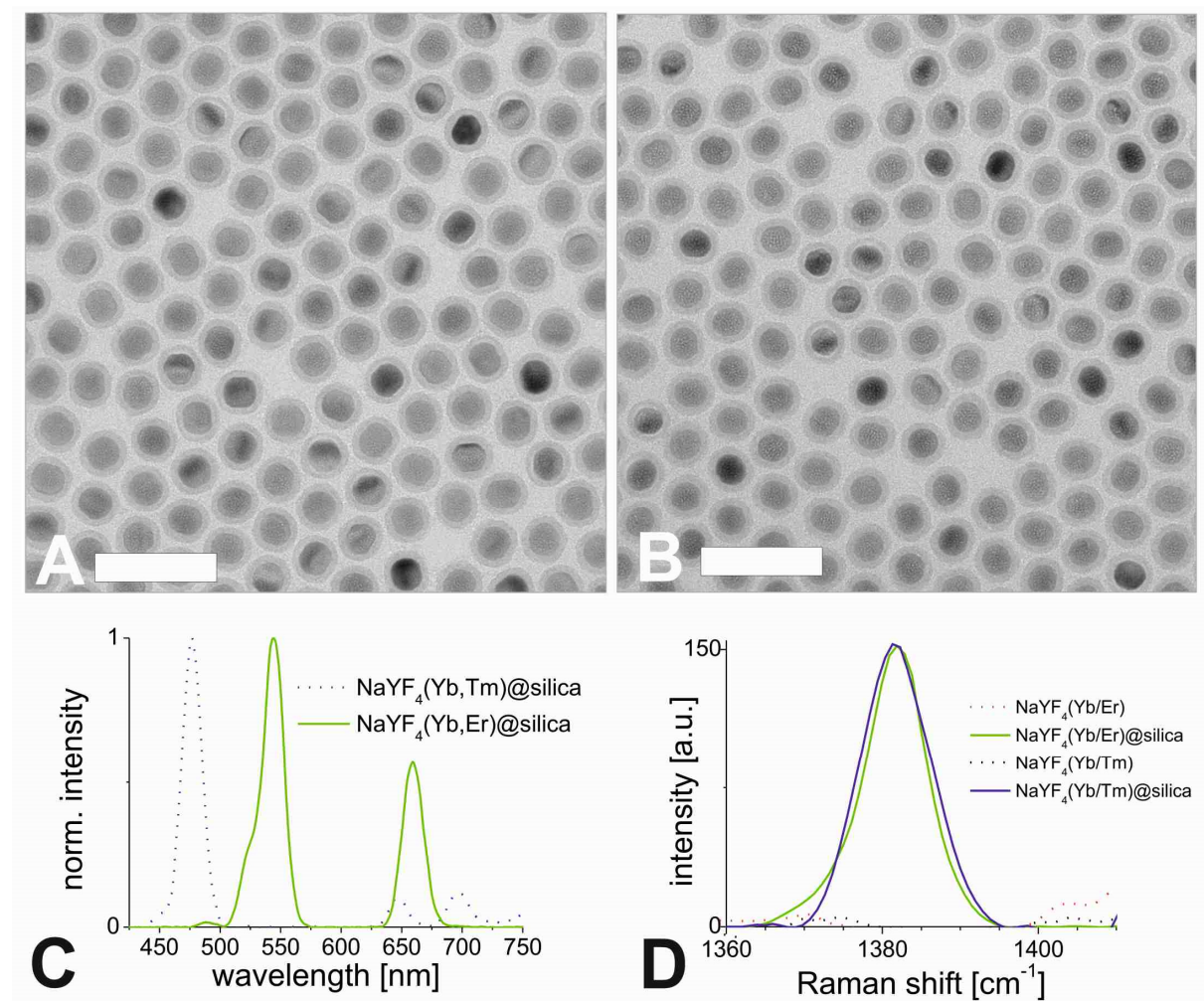
Figure 10 | TEM images of silica-coated UCLNPs of the type β-NaYF$_4$(20 % Yb^{3+}/2 % Er^{3+})@silica (**A**) and of the type β-NaYF$_4$(25 % Yb^{3+}/0.3 % Tm^{3+})@silica (**B**) in water (1 mg/mL) before functionalization with PEG2000-NHS. The sample was prepared by dropping an aliquot of approximately 2 µL of silica-coated UCLNPs dispersion onto the surface of a carbon-coated copper grid. Scale bars indicate 100 nm. Normalized upconversion luminescence spectra of silica-coated Yb^{3+}/Tm^{3+} (dotted blue line) and Yb^{3+}/Er^{3+}-doped, β-NaYF$_4$ nanocrystals (solid green line) upon 980 nm CW laser excitation (~ 15 W·cm^{-2}) are shown in (**C**). Raman spectra of UCLNPs with silica (solid lines) and without silica (dotted lines) are shown in (**D**). The same conditions were maintained in all experiments.

Normalized upconversion luminescence spectra of Yb^{3+}/Er^{3+} and Yb^{3+}/Tm^{3+}-doped, silica coated, multicolor particles dispersed in deionized water solution are shown in Figure 10. Silica-coated nanocrystals also exhibit a Raman peak at 1381 cm^{-1} as displayed in Figure 10. This band is not present for the uncoated nanoparticles, and is likely to be due to the Si-CH$_2$ scissoring mode [218]. In the next step, a silane reagent with a PEG2000 spacer and activated as an N-hydroxysuccinimide (NHS) ester was covalently bound to the surface *via* a silanization technique [219]. The PEG spacer is beneficial in that it can prevent agglomeration, reduce unspecific binding, and improve solubility in water. The NHS ester groups render the silica-coated UCLNPs highly reactive towards proteins, as shown by labeling of streptavidin-modified magnetic beads.

We have attempted to calculate the number of NHS groups on a nanocrystal. In order to do so, the following assumptions have been made: (a) The average radius of the nanocrystals is ~ 19 nm. (b) The average radius of a (spherical) PEG2000 molecule is approximately 1.5 nm [220]. The volume of a spherical nanocrystal with a radius of 19 nm can be calculated to be 29 µm³, and the volume of a spherical PEG2000 molecule with a radius of 1.5 nm to be 14 nm³. The total volume of a spherical nanocrystal loaded with PEG2000 is 45 µm³. The number of PEG2000 molecules can be calculated if the difference (45 µm³ - 29 µm³) is divided by 14 nm³ and yields about 1100 NHS groups per (spherical) silica-coated nanocrystal. We have to stress here that this is a rough number only and also presume that the number of NHS groups per nanocrystal can be governed (reduced) by using mixtures of PEG2000-NHS reagent and PEG2000-modified silyl reagent (without NHS groups), but this has not been verified experimentally.

3.4.3.   Protein Conjugation and SPR Measurements

Two sets of experiments were carried out. In a first (positive control) experiment, streptavidinylated magnetic beads were mixed with UCLNP NHS esters in a conjugation buffer (HCB) of pH 9. After 2 hours at room temperature, the magnetic beads were collected with a permanent magnet and washed with HCB. The collected spot of streptavidin-modified magnetic beads was identified by its upconversion luminescence upon 980 nm CW laser excitation (see Figure 11). This proves that the protein-reactive multicolor UCLNPs bind to

streptavidin. In a second (negative control) experiment, the UCLNP NHS esters were previously deactivated by reacting them with the amino groups of TRIS buffer solution (2 mM, pH 8.5) overnight at room temperature. The first experiment was then repeated with the deactivated nanoparticles. Indeed, the upconversion luminescence of the collected cluster of streptavidin-modified magnetic beads was not observed. This fact proves that the deactivated particles are not bound to the streptavidinylated magnetic beads. On the other hand, a dispersion of the unreactive particles also display upconversion emission upon 980 nm CW laser excitation (see Figure 11).

In order to quantitatively verify the functionality of protein-reactive nanoparticles, their binding to surface-immobilized BSA was monitored by surface plasmon resonance (SPR) measurements in real time. SPR provides a well-known label free method to study interaction of biomolecules on thin gold films [221]. We coated the thin gold surface with a monolayer of a carboxyl-terminated alkanethiol.

The protein was immobilized *via* EDC coupling onto this surface. The binding of protein-reactive NPs to BSA was studied by measuring the shift in the surface plasmon resonance. Therefore, one can either measure the angle of minimum reflection of the light as a function of time, or monitor the time-dependent change in the intensity of the reflected light at a constant angle of incidence. The kinetics for binding of the nanoparticles to the protein layer can be seen in Figure 11. Both the protein-reactive and the deactivated UCLNPs bind to BSA. After washing with 0.1 mM hydrochloric acid for 10 minutes and then with hydrogen carbonate buffer for another 10 minutes, it can be clearly seen that the protein-reactive particles still bind quite strongly. Some deactivated particles also bind due to non-specific binding. On the other hand, when using nanoparticles with a silica shell without NHS groups, we also see unspecific binding, but the particles can be simply washed off with buffer.
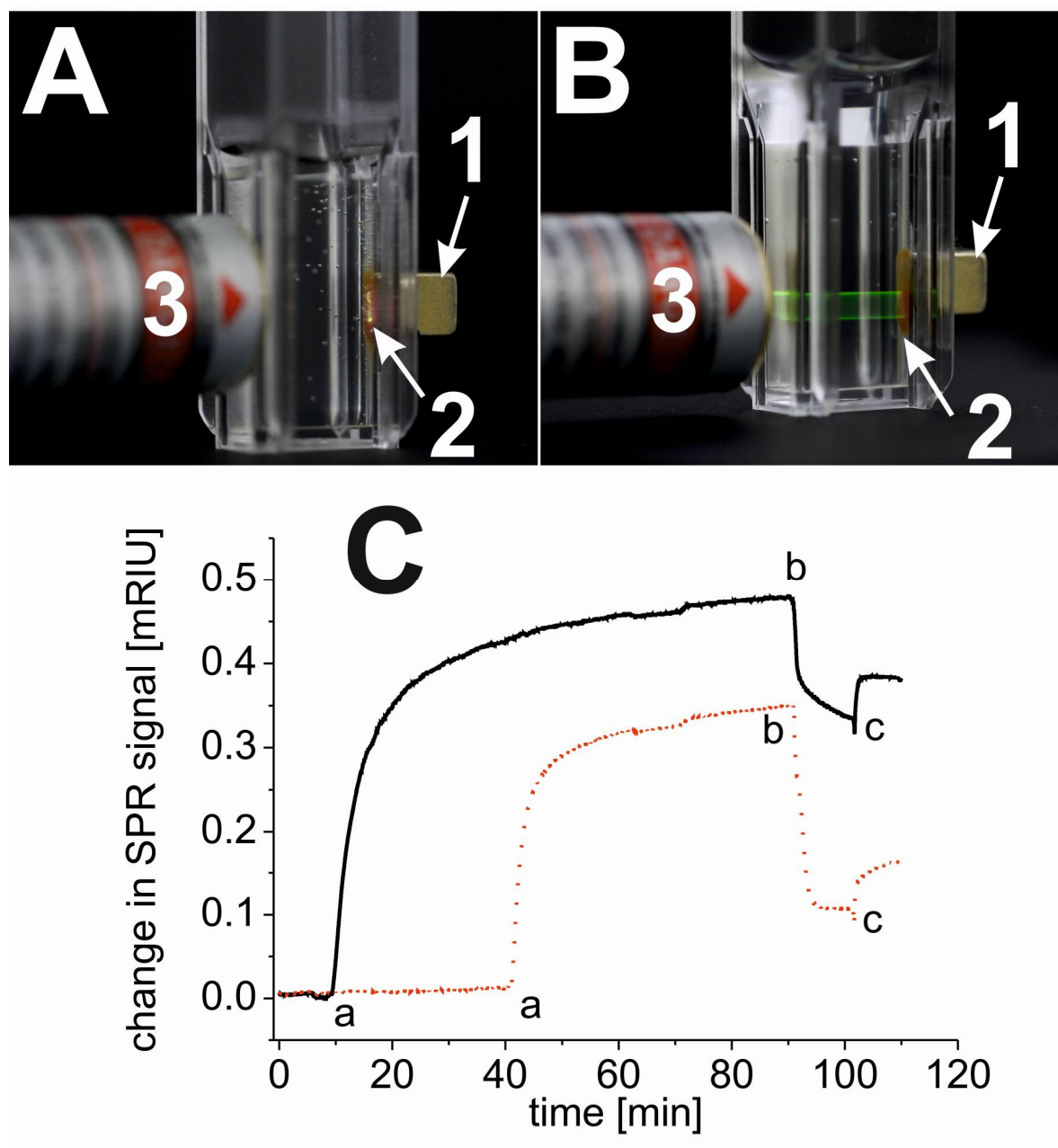
Figure 11 | (**A;** top) Digital photograph of protein-reactive UCLNPs bound to streptavidin-modified magnetic beads (**2**), collected with a permanent magnet (**1**) upon 980 nm CW laser (**3**) excitation (280 mW; ~ 10 W·cm^{-2}) in a hydrogen carbonate buffer. (**B;** top) Photograph illustrating that UCLNP NHS esters that were deactivated by reaction with Tris buffer and dispersed in a hydrogen carbonate buffer do not bind to streptavidinylated magnetic beads (**2**). (**C;** bottom) SPR results showing the unspecific binding of deactivated UCLNPs (dotted red line) and specific binding of protein-reactive UCLNPs (solid black line) to BSA immobilized on a gold substrate. The curves show the addition of the respective UCLNPs in a hydrogen carbonate buffer (**a**), and the washing steps with hydrochloric acid (0.1 M, **b**), and hydrogen carbonate buffer solution (**c**).

3.5.   Conclusion

The preparation of monodisperse, multicolor UCLNPs with controlled diameters of ~ 26 nm using a modified solvothermal method is reported. In order to make them amenable to (bio)-analytical applications, surface modification was performed by first depositing a thin silica shell (~ 5 nm thick) on the hydrophobic nanoparticles, this followed by coating it with a poly(ethylene glycol) spacer carrying N-hydroxysuccinimide groups. The resulting particles form stable dispersions in aqueous solution and are highly reactive towards proteins such as streptavidin and bovine serum albumin. Such amino-reactive labels form an attractive alternative to thiol-reactive UCLNPs [222]. Specifically, the reactive UCLNPs were conjugated to streptavidin-modified magnetic beads. The streptavidinylated magnetic beads labeled with UCLNPs were separated by magnetic force and displayed upconversion luminescence upon 980 nm CW laser excitation. We believe that such amino-reactive multicolor nanoparticles can be employed as luminescent labels for various kinds of (organic) amines, biogenic amines, proteins, or amino-modified oligomers. Labeled proteins have numerous applications such as in immunoassays, enzymatic assays, and in imaging. All these will strongly benefit from the use of labels with photon upconversion capability.

4. Spectrally Matched Upconverting Luminescent Nanoparticles for Monitoring Enzymatic Reactions

4.1. Abstract

The preparation of upconverting luminescent nanoparticles (UCLNPs) that are spectrally tuned such that their emission matches the absorption bands of the two most important species associated with enzymatic redox reactions is reported. The core-shell UCLNPs consist of a β-NaYF$_4$ core doped with Yb^{3+} and Tm^{3+} ions and a shell of pure β-NaYF$_4$. Upon 980 nm excitation, they display emission bands peaking at 360 nm and 475 nm which is a perfect match to the absorption bands of the enzyme cosubstrate NADH and the coenzyme FAD, respectively. By exploiting these spectral overlaps, fluorescent detection schemes have for NADH and FAD been designed that are based on the modulation of emission intensities of UCLNPs by FAD and NADH *via* an inner filter effect.

This chapter has been submitted.

Stefan Wilhelm, Melisa del Barrio, Josef Heiland, Sandy F. Himmelstoß, Javier Galbán, Otto S. Wolfbeis, and Thomas Hirsch. *Submitted.*

Author contributions

SW synthesized and characterized the nanoparticles; wrote the manuscript. SW, JH performed lifetime measurements. SW and SFH performed surface modification of nanoparticles and proof-of-concept experiments. SW, MB, JG, OSW, and TH discussed the results. TH supervised the project and is corresponding author.

4.2.   Introduction

Upconverting luminescent nanoparticles (UCLNPs) are capable of converting near-infrared (NIR) excitation light into visible light [166]. The most efficient UCLNPs consist of lanthanide-doped $NaYF_4$ as a host material [118]. Ytterbium(III) ions, which act as sensitizers, absorb excitation light (usually with a wavelength of 980 nm) and then transfer energy to activator ions such as thulium(III). The relaxation of the excited state of activator ions to their ground states leads to the emission of photons shorter in wavelength than the excitation wavelength. This process is known as energy transfer upconversion (see Scheme 3) [116]. Sensitizer and activator ions are usually incorporated into an inorganic host lattice consisting of hexagonal (β-phase) $NaYF_4$. This host is considered to be an ideal material for highly efficient UCLNPs due to its low phonon energy, which reduces multiphonon relaxation steps and due to excited state lifetimes of up to a few milliseconds [155]. These highly photostable UCLNPs have been widely applied as contrast agents in biomedical imaging and biochemical sensing recently because autofluorescence of biological matter is largely reduced when using NIR light as an excitation source [206,223]. Moreover, UCLNPs exhibit tunable emissions with narrow emission bandwidth, low cytotoxicity, and they can be incorporated into living cells, and used as nanolamps for the excitation of fluorophores [224,225,226].Their unique optical properties also have resulted in the design of quite new chemical sensing schemes [169].

Flavin adenine dinucleotide (FAD; a coenzyme) and nicotinamide adenine dinucleotide (NADH; a cosubstrate of all dehydrogenases) are essential coreactands in numerous enzymatic redox reactions and in biological electron transport [227]. For example, the $NADH/NAD^+$ system transfers hydrogen atoms and electrons from one metabolite to another in many cellular redox reactions and is a known cofactor in more than 300 types of enzymatic reactions [228]. Electrochemical methods have been reported to monitor NADH *via* oxidation to NAD^+ during an enzymatic reaction [229,230]. However, interferences by easily oxidizable other species are compromising their selectivity since direct electrochemical oxidation of NADH at a bare electrode requires a high overpotential [231,232]. Electrode fouling due to the adsorption of stable reaction intermediates formed during the oxidation process is another issue [233].

To overcome these concerns, the electrode surface can be chemically modified, or mediators are being introduced. Lisdat *et al.* have reported on the concentration-dependent detection of NADH in the 20 µM to 2 mM range by immobilizing CdSe/ZnS nanocrystals (quantum dots, QDs) on gold. Such a photoswitchable interlayer of QDs on a gold electrode allows for a spatially resolved read-out of the sensor surface at low electrode potentials (at ~ 0 V vs. Ag/AgCl, 1 M KCl) [234]. Most NADH-based enzymatic reactions are monitored *via* UV spectroscopy at 345 nm where NADH (in contrast to NAD$^+$) displays fairly strong absorption. Numerous (clinical) assays rely on this scheme that can be operated in the kinetic and in the endpoint mode [235]. Both FAD and NADH display intrinsic fluorescence. They can be excited by 450 nm light in case of FAD (emission peaking at 512 nm) and by 350 nm light in case of NADH (emission peaking at 450 nm) [236,237]. Scheper *et al.* developed a method and instrument for the on-line monitoring of the cultivation of various kinds of cells typically grown in bioreactors. It is based on the detection of the fluorescence of NAD(P)H *in situ* [238]. Unfortunately, NADH has a low quantum yield, and excitation in the UV causes biological samples such as serum or bioreactor fluids to display strong autofluorescence [239,240].

In addition, excitation light (350 nm) often is screened off due to an inner filter effect so that methods that work at much longer wavelengths are preferred. It was shown, for example, that NADH can be determined with the help of optical probes. Recently, Su *et al.* reported on albumin-coated CuInS$_2$ QDs emitting in the NIR for the determination of pyruvate using lactate dehydrogenase and NADH [241]. The fluorescence of the QDs with their emission peak at 680 nm is quenched by NADH. Willner *et al.* introduced CdSe/ZnS QDs modified with Nile Blue to monitor NADH-associated biocatalytic transformations [242]. They were applied to metabolic studies on cancer cells, and anticancer agents were screened with respect to their effect on metabolism. Recently, Natrajan *et al.* reported on the application of upconverting two-wavelength phosphors (of unspecified size) to ratiometric monitoring of the enzyme pentaerythritol tetranitrate reductase *via* FRET (which we seriously doubt to occur given the distances involved in their system) [243].

Here, we present an enzymatic detection scheme for the two most common cosubstrate and coenzyme in enzymatic reactions, *viz.* NADH and FAD. It relies on the modulation of either the blue or the UV emission of specifically designed UCLNPs by NADH

and FAD, respectively. Most notably, NIR excitation (980 nm) can be applied, which is in striking contrast to practically all existing fluorometric methods.

4.3.   Materials and Methods

4.3.1.   Chemicals

Yttrium(III) chloride hexahydrate (99.99 %), ytterbium(III) chloride hexahydrate (99.9 %) were from Treibacher (www.treibacher.com). Thulium(III) chloride hexahydrate (99.99 %), ammonium fluoride (ACS reagent $\geq$ 98.0 %), sodium hydroxide (reagent grade $\geq$ 98.0 %), poly(isobutylene-*alt*-maleic anhydride) (PMA) average Mw ~ 6 kDa, dodecylamine (98 %), glucose oxidase from *Aspergillus niger* (type X-S, lyophilized powder, with an activity of 147.9 U·mg^{-1} of lyophilized solid, EC 1.1.3.4), alcohol dehydrogenase from *Saccharomyces cerevisiae* (lyophilized powder, $\geq$ 300 units·mg^{-1} protein), β-nicotinamide adenine dinucleotide hydrate ($\geq$ 99 %), tris(hydroxymethyl)aminomethane (ACS reagent, $\geq$ 99.8 %), semicarbazide hydrochloride ($\geq$ 99 %), β-D(+)-glucose, 2-(N-morpholino)-ethanesulfonic acid (MES), glycine (ACS reagent, $\geq$ 98.5 %), boric acid (99.999 %), flavin adenine dinucleotide (FAD) disodium salt ($\geq$ 95 %), β-Nicotinamide adenine dinucleotide (NADH), reduced dipotassium salt were purchased from Sigma-Aldrich (www.sigmaaldrich.com). Oleic acid (technical grade 90 %) and 1-octadecene (technical grade 90 %) were from Alfa Aesar (www.alfa.com). All other reagents and organic solvents were of the highest grade available. Unless otherwise noted, all chemicals were used as received without further purification.

4.3.2.   Instrumentation

Transmission electron microscopy (TEM) was performed using a 120 kV Philips CM12 microscope (www.fei.com). Samples were prepared by dropping colloidal dispersions (~ 10 µL) on carbon-coated copper grids (400 mesh) from Plano (www.plano-em.de) and

subsequent evaporation of the solvent. The particle size distributions of the nanocrystals were evaluated from the TEM images using the ImageJ software (http://rsbweb.nih.gov/ij/). The Zetasizer Nano-ZS from Malvern (www.malvern.com) was used for dynamic light scattering experiments (DLS) with intensity distribution weighed mode and for the measurement of the zeta potential. X-ray powder diffraction (XRD) patterns with a resolution of $0.005°$ (2θ) were collected using a Huber Guinier G670 diffractometer (www.xhuber.com) with a Cu source (Kα radiation, $\lambda = 1.54060$ Å) operating at 40 kV and 30 mA. A Flame-EOP inductively coupled plasma optical emission spectrometer (ICP-OES) from Spectro (www.spectro.com) was used for the determination of the amount of rare-earth ions in the UCLNPs. All centrifugation steps were carried out using a Hettich Universal 320 centrifuge (www.hettichlab.com). A Sonorex Digitech DT255H ultrasonic bath from Bandelin (www.bandelin.com) was used. The upconversion luminescence spectra were recorded at room temperature with a luminescence spectrometer (LS 50 B) from Perkin Elmer (www.perkinelmer.com) modified with a 980 nm CW laser module (120 mW, ~ 15 W·cm^{-2}) from Roithner (www.roithner-laser.com) for upconversion photo-excitation. The upconversion luminescence lifetimes of the UCLNPs were measured using a home-built setup (see Scheme 5). Wires, cooling hoses, the optical fiber inlet for the photomultiplier tube (PMT)-detector (PreSens LED Photomultiplier Unit, www.presens.com) and the housing are not depicted in Scheme 5. The optical bandpass filter (FF02-470/100-25) for measuring a single emission band was bought from Semrock (www.semrock.com). The optical chopper system (MC2000 with two slot chopper blade MC1F2) was purchased from Thorlabs (www.thorlabs.com). The laser module (DH-980-200-3, 200 mW, ~ 130 W·cm^{-2}) was bought from Picotronic (www.picotronic.com). To store and analyze the amplified signal a digital oscilloscope DSO 8204 from Voltcraft (www.voltcraft.ch) and LabVIEW-code (www.ni.com/labview) were used.
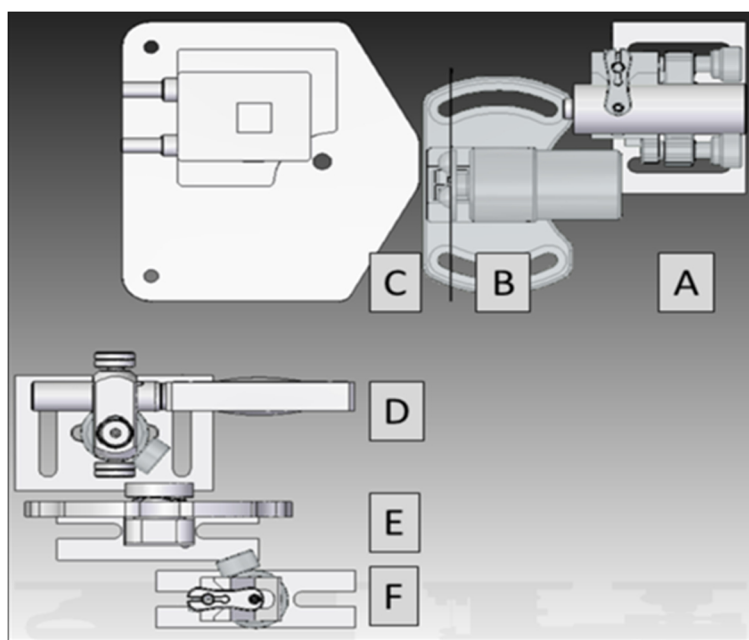
Scheme 5 | Top-view of the setup used for the measurement of upconversion luminescence lifetimes, consisting of (**A**) a 980 nm CW laser module (200 mW, ~ 130 W·cm^{-2}), (**B**) an optical chopper, (**C**) a temperature controlled cuvette holder with integrated magnetic stirring, (**D**) a flexibly mounted collecting lens, (**E**) a filter wheel for bandpass filters and (**F**) a clamp holder for an optical fiber connected to a subsequent photomultiplier tube (PMT).

4.3.3. Synthesis of Nanoparticles based on α-NaYF$_4$

Cubic-phase α-NaYF$_4$ nanocrystals were prepared by dissolving YCl$_3$·6H$_2$O (5 mmol) in ~ 5 mL of methanol using sonication. This solution was transferred into a 250 mL flask, mixed with 80 mL of oleic acid and 150 mL of 1-octadecene under an atmosphere of nitrogen and heated to 160 °C. A homogeneous, clear solution was formed after 30 minutes at 160 °C under vacuum. The reaction mixture was then cooled to room temperature and 50 mL of methanol containing NaOH (0.25 M) and NH$_4$F (0.4 M) were added at once. After stirring for 30 minutes at 120 °C, the resulting colloid suspension was heated to 240 °C for 30 minutes. After cooling to room temperature, the UCLNPs were precipitated by addition of ~ 100 mL of ethanol and isolated *via* centrifugation at a relative centrifugal force (RCF) of 1000 g for 5 minutes. The pellet was washed several times by dispersing it in small amounts (~ 2 mL) of chloroform and cyclohexane, then precipitating them by the addition of a large excess (~ 20 mL) of ethanol and acetone. Finally, the purified UCLNPs were dispersed in 6 mL of oleic acid/1-octadecene (1/2 v/v) and used as shell material for the preparation of core-shell UCLNPs.

4.3.4. Synthesis of UCLNPs based on β-NaYF₄ doped with Yb³⁺/Tm³⁺ ions

Hexagonal-phase, Yb^{3+}/Tm^{3+}-doped β-$NaYF_4$ nanoparticles were prepared by dissolving the salts $YCl_3 \cdot 6H_2O$ (3.735 mmol), $YbCl_3 \cdot 6H_2O$ (1.25 mmol), and $TmCl_3 \cdot 6H_2O$ (0.015 mmol) in 5 mL of methanol by sonication. This solution was transferred into a 250 mL flask, mixed with 40 mL of oleic acid and 75 mL of 1-octadecene under an atmosphere of nitrogen and heated to 160 °C. A homogeneous, clear solution was formed after 30 minutes at 160 °C under vacuum. The reaction mixture was then cooled to room temperature and 50 mL of methanol containing NaOH (0.25 M) and NH_4F (0.4 M) were added at once. After stirring for 30 minutes at 120 °C, the resulting colloid suspension was heated to reflux (~ 325 °C) for 20 minutes. UCLNPs were precipitated by addition of ~ 100 mL of ethanol after cooling to room temperature. The procedure for cleaning was the same as described for the alpha-$NaYF_4$ nanocrystals. Finally, purified UCLNPs were dispersed in 10 mL of cyclohexane and used as core material for the preparation of core-shell UCLNPs.

4.3.5. Synthesis of Core-Shell UCLNPs based on β-NaYF₄(Yb³⁺/Tm³⁺)@NaYF₄

Hexagonal-phase core-shell UCLNPs based on β-$NaYF_4(Yb^{3+}/Tm^{3+})@NaYF_4$ were prepared as follows [244]: 40 mL of oleic acid and 75 mL of 1-octadecene were mixed in a 250 mL flask and heated to 160 °C under an atmosphere of nitrogen. The mixture was cooled to 80 °C after 30 minutes at 160 °C under vacuum. β-$NaYF_4(Yb^{3+}/Tm^{3+})$ core UCLNPs dispersed in 10 mL cyclohexane were added and the mixture was heated to 120 °C in order to evaporate the cyclohexane. After 30 minutes at 120 °C, the resulting colloid suspension was heated to reflux (~ 325 °C). α-$NaYF_4$ nanocrystals dispersed in 6 mL of oleic acid/1-octadecene (1/2 v/v) were quickly injected. Thereupon, the temperature dropped to ~ 300 °C. The mixture was stirred for another 15 minutes at reflux and cooled to room temperature. The core-shell UCLNPs based on β-$NaYF_4(Yb^{3+}/Tm^{3+})@NaYF_4$ were precipitated by addition of ~ 100 mL of ethanol after cooling to room temperature. The procedure for cleaning was the same as described for the alpha-$NaYF_4$ nanocrystals. Finally, the purified UCLNPs were dispersed in 10 mL of cyclohexane.

4.3.6. Surface Modification using an Amphiphilic Polymer Coating Strategy

The hydrophobic, oleate-coated, core-shell UCLNPs based on β-NaYF$_4$(Yb^{3+}/Tm^{3+})@NaYF$_4$ were coated with an amphiphilic polymer poly(isobutylene-*alt*-maleic anhydride) (PMA) modified with dodecylamine in order to render them water dispersible. The synthesis of the amphiphilic polymer was reported previously [245,246]. Hydrophobic core-shell UCLNPs (500 µL; number of core-shell UCLNPs is ~ 10^{14} as determined by ICP-OES) dispersed in chloroform were mixed together with 100 µL of amphiphilic polymer solution (0.5 M) in a round bottom flask. Afterwards, 5 mL of chloroform were added, and sonication for 5 minutes was applied. Then, the chloroform was slowly evaporated under reduced pressure until the sample was completely dry. The remaining solid film in the flask was re-dispersed in ~ 5 mL of sodium borate buffer (SBB12; 50 mM, pH 12) under vigorous stirring until the solution turned clear. The resulting polymer-coated core-shell UCLNPs were pre-concentrated using centrifuge filters (membrane: 100 kDa Mw cut off, PES, RCF: 870 g; 15 minutes). Centrifugation was carried out until the sample solution had been concentrated to a volume of less than 250 µL. The pre-concentrated core-shell UCLNPs were further purified by centrifugation (17000 g for 30 minutes) and the resulting pellet redispersed in MES buffer (100 mM, pH 6.1).

4.3.7. Quantification of Ethanol

A TRIS buffer solution (pH 8.7, 75 mM) containing 75 mM semicarbazide hydrochloride, 21 mM glycin, 24 mM NAD$^+$, 300 U·mL^{-1} alcohol dehydrogenase and 1 µM amphiphilic polymer-coated core-shell UCLNPs based on β-NaYF$_4$(Yb^{3+}/Tm^{3+})@NaYF$_4$ was prepared. The upconversion emission intensity at 360 nm was measured (I_0). Thereafter, different amounts of ethanol in TRIS buffer solution were added. The enzymatic oxidation of the ethanol took place immediately which resulted in a decrease of the emission intensity at 360 nm due to the production of NADH. The intensity (I) (after the enzymatic reaction stopped) was divided by I_0 and plotted against the mass concentration of ethanol.

4.3.8. Quantification of β-D(+)-Glucose

A MES buffer solution (pH 6.1, 100 mM) containing 600 U·mL^{-1} glucose oxidase (GOx) and 1 µM polymer-coated core-shell UCLNPs based on β-NaYF$_4$(Yb^{3+}/Tm^{3+})@NaYF$_4$ was prepared under nitrogen atmosphere. The solution was transferred into a cuvette and sealed with a layer of paraffin oil. The upconversion emission intensity at 475 nm was measured (I_0). Afterwards, different amounts of glucose in MES buffer solution were added. The enzymatic oxidation of the glucose took place immediately which resulted in an increase of the emission intensity at 475 nm due to the production of FADH$_2$. The intensity (I) (after the enzymatic reaction stopped) was divided by I_0 and plotted against the molar concentration of glucose.

4.4. Results and Discussion

4.4.1. Preparation and Characterization of Core-Shell UCLNPs

UCLNPs consisting of a Yb^{3+}/Tm^{3+}-doped β-NaYF$_4$ core (with an inner diameter of 31.1 ± 1.0 nm) that was covered with a 3 nm shell of pure β-NaYF$_4$ were prepared [211, 244,247,] TEM images of α-NaYF4, which were used as sacrificial nanoparticles for the synthesis of the shell [244], β-NaYF$_4$(Yb^{3+}/Tm^{3+}) core UCLNPs, and β-NaYF$_4$(Yb^{3+}/Tm^{3+})@NaYF$_4$ core-shell UCLNPs are shown in Figure 12. Both the core-only and the core-shell UCLNPs exhibit a narrow size distribution (see Figure 13) and a purely hexagonal (β-phase) crystal structure (see Figure 14) according to the reference pattern (ICDD PDF 16-334). The average diameter of the core-shell UCLNPs based on β-NaYF$_4$(Yb^{3+}/Tm^{3+})@NaYF$_4$ is 36.9 ± 1.4 nm as determined *via* evaluation of TEM images (see Figure 13). In addition, the average nanocrystal size was calculated by evaluating the XRD data using Scherrer's equation to be ~ 3 nm for α-NaYF$_4$, ~ 30 nm for β-NaYF$_4$(Yb^{3+}/Tm^{3+}) core UCLNPs, and ~ 36 nm for β-NaYF$_4$(Yb^{3+}/Tm^{3+})@NaYF$_4$ core-shell UCLNPs. These results are in good agreement with the TEM images. Scherrer's equation, Formula (1), relates the size of sub-micrometer particles, or crystallites, in a solid to the broadening of a peak in a diffraction pattern [248].

$$\tau = \frac{K \cdot \lambda}{\beta \cdot \cos\theta} \tag{1}$$

With τ is the mean size of the ordered (crystalline) domains;

K is a dimensionless shape factor;

λ is the X-ray wavelength;

β is the line broadening at half of the maximum intensity (FWHM), after substracting the instrumental line broadening, in radians;

θ is the Bragg angle.

The solvodynamic diameter of β-NaYF$_4$(Yb^{3+}/Tm^{3+})@NaYF$_4$ core-shell UCLNPs dispersed in cyclohexane was determined by dynamic light scattering experiments to be ~ 35 nm with a polydispersity index (PdI) of 0.134, which is also in good agreement with the results of the TEM images and the XRD data. The concentration of UCLNPs in solution was determined by ICP-OES measurements. The calculation of the elemental composition agrees well with the data calculated from the amounts of lanthanide ions applied in synthesis (see Table 2).

A core-shell architecture was chosen because it increases the intensity of the upconversion luminescence (compared to the emission peak at 475 nm normalized to an Yb^{3+} concentration of ~ 8 mM) by a factor of ~ 60 (see Figure 15).
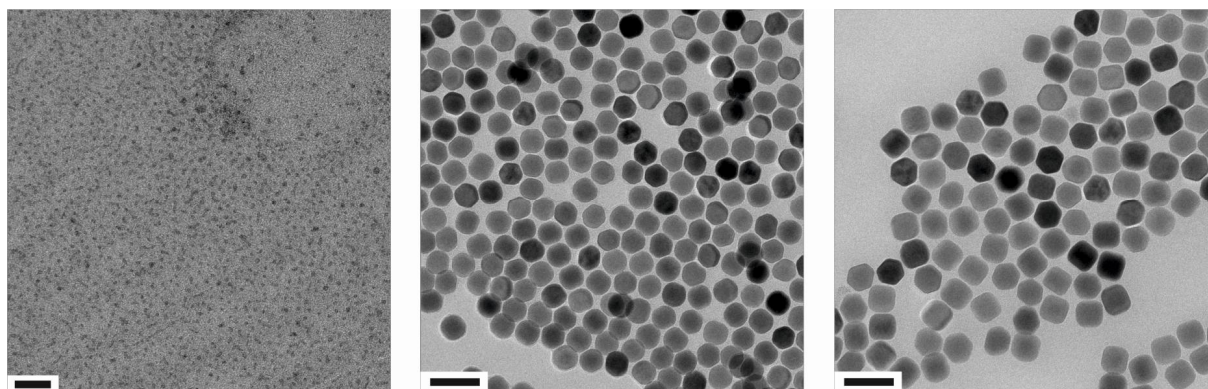
Figure 12 | TEM images of: (*left*) pure un-doped α-NaYF$_4$ nanoparticles (Scale bar indicates 20 nm); (middle) β-NaYF$_4$(Yb^{3+}/Tm^{3+}) core-only UCLNPs (Scale bar indicates 60 nm); and (right) β-NaYF$_4$(Yb^{3+}/Tm^{3+})@NaYF$_4$ core-shell UCLNPs (Scale bar indicates 60 nm).

Table 2 | Elemental composition of α-NaYF$_4$, β-NaYF$_4$(Yb^{3+}/Tm^{3+}), and β-NaYF$_4$(Yb^{3+}/Tm^{3+})@NaYF$_4$ nanocrystals determined by ICP-OES measurements.

Element	α-NaYF$_4$ [mol%]	β-NaYF$_4$(Yb^{3+}/Tm^{3+}) [mol%]	β-NaYF$_4$(Yb^{3+}/Tm^{3+})@NaYF$_4$ [mol%]
Yttrium	100	75.4 ± 0.1	85.2 ± 0.1
Ytterbium	-	24.1 ± 0.1	14.5 ± 0.1
Thulium	-	0.5 ± 0.1	0.3 ± 0.1
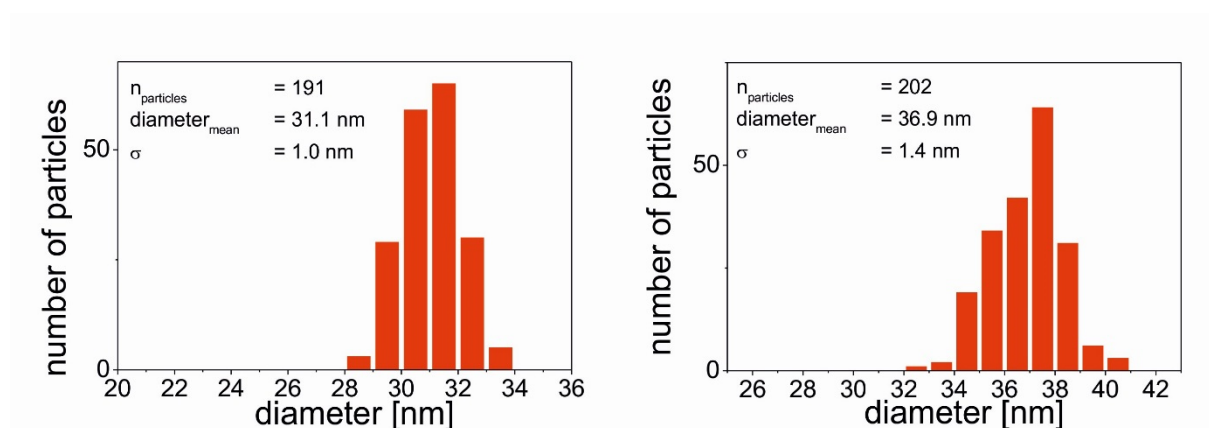
Figure 13 | Size distribution histograms of (*left*) core-only UCLNPs based on β-NaYF$_4$(Yb^{3+}/Tm^{3+}), and (*right*) core-shell UCLNPs based on β-NaYF$_4$(Yb^{3+}/Tm^{3+})@NaYF$_4$ as revealed from the corresponding TEM images.
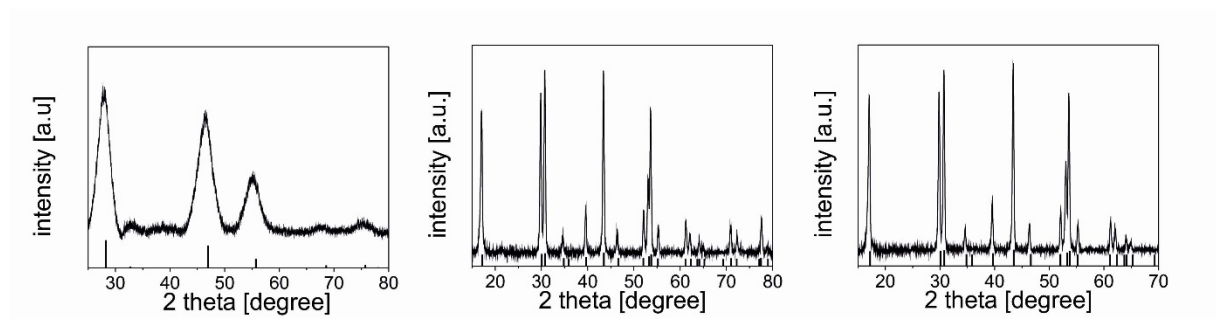
Figure 14 | XRD patterns of: *(left)* pure un-doped α-NaYF$_4$ nanoparticles (reference pattern ICDD PDF 77-2042, cubic phase); *(middle)* β-NaYF$_4$(Yb^{3+}/Tm^{3+}) core-only UCLNPs; and *(right)* β-NaYF$_4$(Yb^{3+}/Tm^{3+})@NaYF$_4$ core-shell UCLNPs (reference pattern ICDD PDF 16-334, hexagonal phase)

The luminescence lifetime of core-only UCLNPs doped with Yb^{3+}/Tm^{3+} (with their emission peaking at 470 nm in cyclohexane dispersion) increased from ~ 0.5 ms to ~ 0.9 ms in case of the core-shell UCLNPs (see Figure 16). A single exponential decay fitting based on the single exponential decay law was used, Formula (2):

$$I(t) = I_0 \cdot e^{-\frac{t}{\tau}} \qquad (2)$$

With $\qquad$ $I(t)$ is the luminescence intensity as a function of time;

$\qquad\qquad\qquad$ I_0 is the luminescence intensity at t = 0;

$\qquad\qquad\qquad$ t is the time after the absorption;

$\qquad\qquad\qquad$ τ is the lifetime.

The increase in the average particle diameter, in luminescence intensity, and in luminescence lifetime along with the results of the ICP-OES measurements prove the presence of a core-shell architecture of the UCLNPs used here [249]. In addition, the results demonstrate the beneficial effect of an un-doped shell of pure NaYF$_4$ around the Yb^{3+}/Tm^{3+}-doped core UCLNPs in terms of quantum yields. This was attributed to the non-radiative deactivation of the excited electronic states of the lanthanide ions [244].
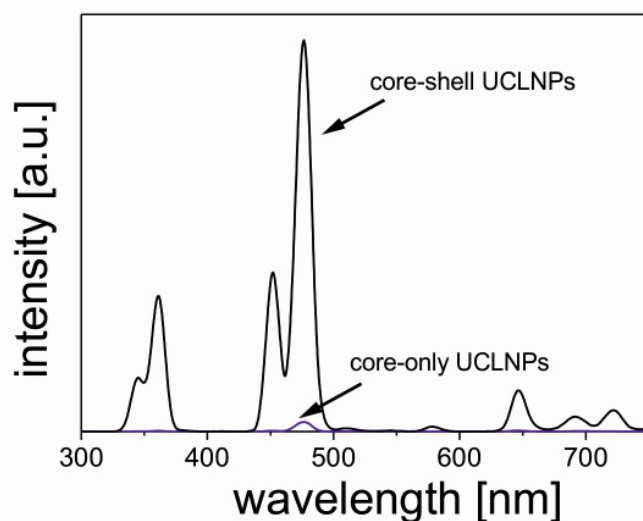
Figure 15 | Upconversion luminescence spectra of β-NaYF$_4$(Yb^{3+}/Tm^{3+}) core-only and β-NaYF$_4$(Yb^{3+}/Tm^{3+})@NaYF$_4$ core-shell UCLNPs dispersed in cyclohexane upon 980 nm CW laser excitation ($\sim$ 15 W·cm^{-2}). Both spectra are normalized to an equal Yb3+ concentration (8.4 mM) as determined by ICP-OES analysis. An enhancement of the upconversion luminescence intensity (peak at 475 nm) by a factor of $\sim$ 60 can be calculated.
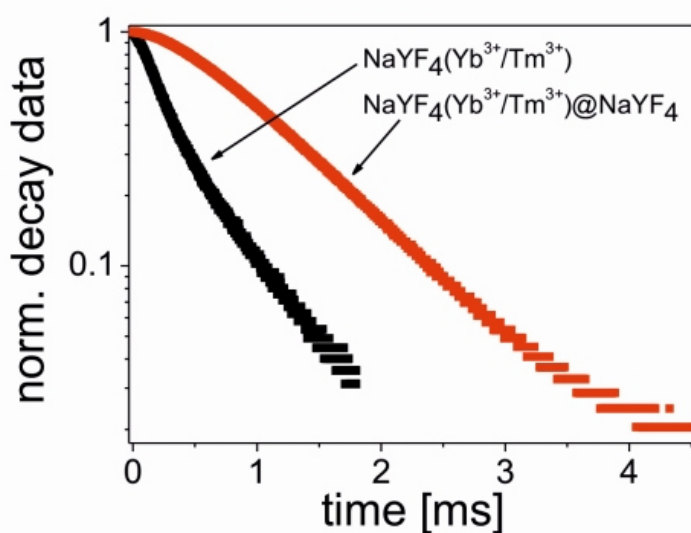
Figure 16 | Upconversion luminescence lifetimes (emission at 470 nm) obtained for β-NaYF$_4$(Yb^{3+}/Tm^{3+}) core-only ($\sim$ 0.5 ms; black line) and β-NaYF$_4$(Yb^{3+}/Tm^{3+})@NaYF$_4$ core-shell UCLNPs ($\sim$ 0.9 ms; red line) dispersed in cyclohexane upon 980 nm CW laser excitation (excitation power density $\sim$ 130 W·cm^{-2}). The upconversion luminescence lifetime of core-shell UCLNPs dispersed in MES buffer (100 mM, pH 6.1) was the same as measured in cyclohexane *viz.* $\sim$ 0.9 ms.

4.4.2. Surface Modification

Core-shell UCLNPs obtained in this way are hydrophobic and carry an oleate coating. In the next step, they were covered with the amphiphilic polymer poly(isobutylene-*alt*-maleic anhydride; PMA) that was previously modified with dodecylamine. This coating is remarkable stable, probably due to the strong van-der-Waals interaction of the hydrophobic chains of the polymer with the hydrocarbon chains of oleate-coated UCLNPs. In addition, this coating renders the UCLNPs water dispersible, obviously because its outward-directed polar side chains increase hydrophilicity.

The hydrophilic UCLNPs can be colloidally dispersed in aqueous media after drying and purification. The hydrodynamic diameter of β-NaYF$_4$(Yb^{3+}/Tm^{3+})@NaYF$_4$ core-shell UCLNPs (coated with PMA modified with dodecylamine) dispersed in 2-(N-morpholino)ethanesulfonate (MES; 100 mM) buffer of pH 6.1 is ~ 61 nm (PdI 0.124). Their zeta-potential is ~ 47 mV in MES buffer (100 mM, pH 6.1), and the colloid is stable for months [245,246]. This indicates that the surface-modified UCLNPs do not aggregate under these conditions.

4.4.3. (Bio)-analytical Applications

Core-shell UCLNPs used in this work exhibit emission bands matching the absorption bands of both NADH and FAD. The normalized UV luminescence (peaking at 360 nm) of the Yb^{3+}/Tm^{3+}-doped core-shell UCLNPs upon 980 nm continuous wave (CW) laser excitation at a power density of ~ 15 W·cm^{-2} is shown in Figure 17. It can be seen that it nicely matches the absorption band of NADH. The normalized visible (blue) luminescence of UCLNPs (peaking at 475 nm) in Figure 17(B) along with the absorption band of FAD. The two upconversion luminescence bands are the result of electronic transitions from the ^{1}D$_2$ to the ^{3}H$_6$, and from the ^{1}G$_4$ to the ^{3}H$_6$ state, respectively, of Tm^{3+} activator ions of UCLNPs.

Figure 18 shows the decrease in the intensity of the upconversion emission at 360 nm with increasing concentration of NADH, and also at 475 nm with increasing concentrations of FAD. This can be attributed to an inner filter effect, not the least because the decay time of the 470 nm emission (~ 0.9 ms) does not change on addition of FAD. An

energy transfer between the UCLNPs and FAD and NADH can be excluded. Rather, the core-shell UCLNPs are acting as nanolamps whose emission is screened off. NADH can be detected in this way in the 30 to 150 μM concentration range, and FAD in the 30 to 100 μM range.
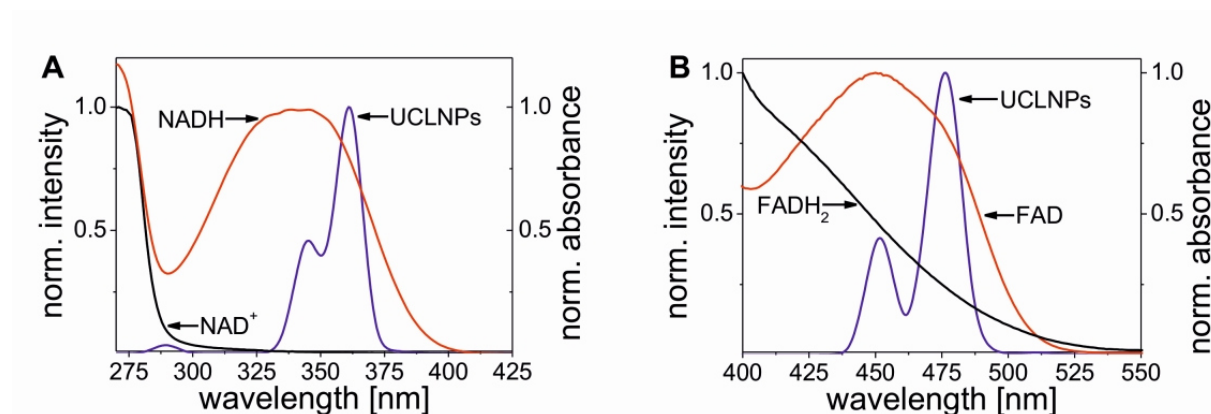
Figure 17 | Normalized upconversion luminescence spectra of hydrophilic β-NaYF$_4$(Yb^{3+}/Tm^{3+})@NaYF$_4$ core-shell UCLNPs dispersed in MES buffer (100 mM, pH 6.1) upon 980 nm CW laser excitation (~ 15 W·cm^{-2}, blue line). (A) Normalized absorption spectra of NAD$^+$ (black line) and NADH (red line) in MES buffer. (B) Normalized absorption spectra of FADH$_2$ (black line) and FAD (red line) in MES buffer.
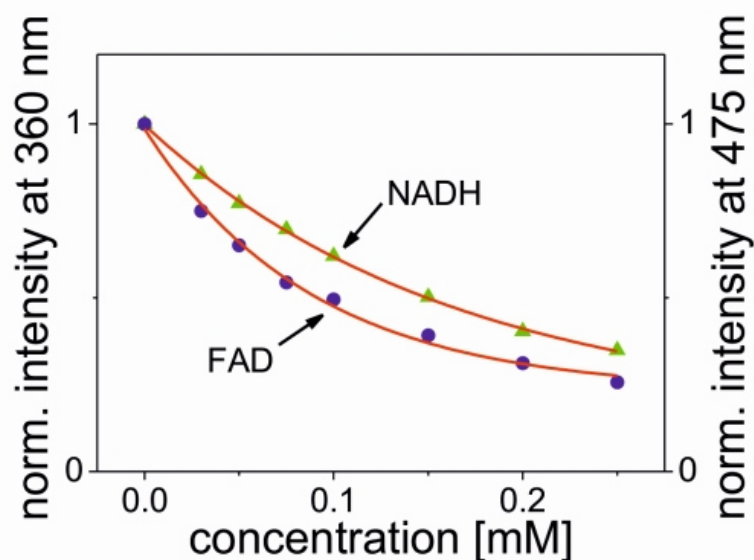
Figure 18 | Decrease of upconversion luminescence intensities at 360 nm with increasing concentration of NADH and at 475 nm with increasing concentration of FAD due to the absorption of the redox cofactors upon 980 nm CW laser excitation (~ 15 W·cm^{-2}).

Next, two enzymatic reactions were studied in order to demonstrate the potential of this detection scheme. In the first experiment, the NAD^+-associated oxidation of ethanol by alcohol dehydrogenase in Tris buffer solution of pH 8.7 was monitored in the presence of UCLNPs which were found to remain completely inert. This reaction involves the oxidation of ethanol to form acetaldehyde (ethanal) along with NADH. While NAD^+ does not absorb light at 360 nm, NADH is a strong absorber that can attenuate the emission at 360 nm as can be seen in Figure 19(A). Ethanol can be quantified by this method in the concentration range from 0.5 to 2.7 mg·L^{-1}.

In an experiment involving the coenzyme FAD, we have monitored the enzymatic oxidation of β-D-glucose by glucose oxidase (GOx) to form D-glucono-1,5-lactone in MES buffer solution of pH 6.1 in the presence of UCLNPs. In this case, the situation is reversed in that the absorber (FAD) initially is present in high concentration but is converted to a non-absorbing species ($FADH_2$) in the course of the reaction. As a result, the emission peaking at 475 nm increases over time. Glucose can be determined by this method in the 20 to 200 µM glucose concentration range as can be seen in Figure 19(B).
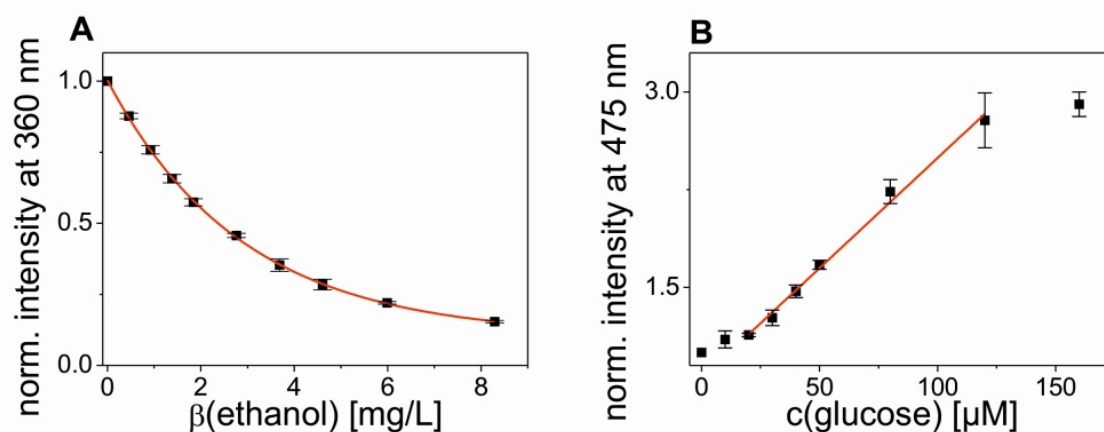
Figure 19 | Quantification of (A) ethanol and (B) glucose using NADH- and FAD-related enzymatic reactions. Each data point reflects the average of three measurements, operated in the endpoint mode.

It was shown in substantial work by Chance *et al.* that the fluorescence of NADH is a measure for the cellular oxidation-reduction state *in vivo*, and this has found clinical uses [250]. The detection of mitochondrial NADH, in turn, was reported to assist in

cancer diagnosis [251]. The NAD^+/NADH ratio represents an important parameter of what is (unprecisely) called the "redox state" of a cell, a ratio that reflects both the metabolic activities and the health of a cell [252]. Two-photon excited (2-PE) fluorescence and microscopy can eliminate most of the background that is generated by UV excitation of NAD(P)H and flavoproteins and therefore represents a powerful tool to determine intracellular redox state of cells [253]. However, classical 2-PE is prone to photo-bleaching [254]. The approach presented here (*via* upconversion luminescence) offers a highly attractive alternative to any kind of 2-PE but without the need for high-energy pulsed lasers and the generation of any background luminescence in the UV or visible.

4.5.   Conclusion

In summary, it is demonstrated that core-shell UCLNPs based on β-NaYF$_4$(Yb^{3+}/Tm^{3+})@NaYF$_4$ with their two emission peaks at 360 nm and 475 nm can be used to fluorescently monitor the formation of NADH and the consumption of FAD during enzymatic reactions using 980 nm photoexcitation. Given the average distances between the nanoparticles (where luminescence is created) and the coenzymes in solution (which is far beyond any Förster distance) we conclude from luminescence lifetime measurements that the effect is the result of an inner filter effect. Rather, the UCLNPs act as a kind of nanolamps. The effect is exemplarily shown to enable enzymatic assays for glucose and ethanol in that the intensity of the emission of the core-shell UCLNPs is affected by either the formation of NADH or the consumption of FAD. We presume that this method is applicable to numerous other enzymatic processes based on the NAD^+/NADH (NADP$^+$/NADPH) or FAD/FADH$_2$ redox systems. Both cofactors are involved in many biochemical processes, *e.g.* oxidative phosphorylation, which may be monitored by the use of UCLNPs *in vivo*. Moreover, this approach is not limited to the determination of substrate levels but, conceivably, also to monitoring enzyme activities.

Acknowledgments

5. Improved Synthesis of Hydrophilic Upconverting Luminescent Nanoparticles, and a Study on their Luminescence Properties

5.1. Abstract

We developed a luminescence-controlled large scale synthesis protocol yielding in ~ 2 g of monodisperse upconverting luminescent nanoparticles (UCLNPs) based on hexagonal phase $NaYF_4(Yb^{3+}/Er^{3+})$, which enables the investigation of the influence of different surface chemistries on the upconversion emission. These oleate-coated UCLNPs of ~ 23 nm size exhibit a quantum yield of ~ 0.35 % dispersed in cyclohexane at an excitation power density of 150 W·cm^{-2}. Hydrophobic UCLNPs were characterized by TEM, XRD, TGA, ICP-OES, and luminescence spectroscopy and subsequently modified with nine different widely used surface coatings in order to render them water dispersible. Dynamic light scattering and electrophoretic mobility measurements proved the colloidal stability of water-dispersible UCLNPs. The ratio of the upconversion emission bands at 545 nm and 658 nm allows for a distinct classification of all surface modifications into two general groups: (1) additional (amphiphilic) layer coatings; and (2) ligand exchange strategies. This study reveals that modifications, preserving the initial oleate coating, show a reduced non-radiative deactivation of excited states of lanthanide ions by H_2O compared to UCLNPs rendered water soluble *via* ligand exchange. A similar classification could be found upon exchanging H_2O for D_2O.

Stefan Wilhelm, Martin Kaiser, Christian Würth, Josef Heiland, Carolina C. Carrion, Verena Muhr, Otto S. Wolfbeis, Wolfgang J. Parak, Ute Resch-Genger, Thomas Hirsch. *Submitted.*

Author contributions

SW synthesized and characterized the nanoparticles; wrote the manuscript. SW, MK, CW, JH performed quantum yield measurements. SW, VM, CCC performed surface modification of nanoparticles. All authors discussed the results. URG and TH supervised the project and are corresponding authors.

5.2. Introduction

Lanthanide-doped upconverting luminescent nanoparticles (UCLNPs) have gained much attention as a promising class of novel labels and probes [144,162,255,256]. The sequential absorption of multiple low energy excitation photons in the near-infrared (NIR) by lanthanide ions incorporated in an inorganic host material results in anti-Stokes emissions, referred to as upconversion luminescence [116,118]. In case of $NaYF_4$ as a host material and by using Yb^{3+} and Er^{3+} as sensitizer and activator dopant ions, respectively, excitation typically occurs at 980 nm. Advantages of NIR excitation include: (a) significant minimization of photo-damage of biological specimens, (b) maximization of the penetration depth of the excitation light in biological tissue, and (c) excellent signal-to-noise ratio along with improved detection sensitivity, since NIR illumination does not cause any auto-fluorescence of biomaterials. Upconversion luminescence is known to be more efficient than nonlinear multiphoton absorption of organic dyes because simultaneous absorption of multiple photons is not required [257]. Therefore, excitation can be performed with low-cost and low-power continuous wave (CW) laser diodes. Unlike semiconductor nanocrystals based on CdSe and related quantum dots, UCLNPs do not show intermittency (blinking) upon continuous excitation, and emission peak positions are not affected by particle size [145], both attributes making them highly attractive for bioimaging applications. Moreover, UCLNPs can be used for long-term imaging because of their high photostability. Additional doping with Gd^{3+} ions results in multimodal nanoparticles capable of magnetic resonance imaging or computed tomography [139].

Besides preferably high upconversion luminescence efficiency, there are several requirements which need to be fulfilled for the further use of UCLNPs in bio-applications and photovoltaics. Spherical monodisperse UCLNPs of pure crystallinity and exact stoichiometric composition need to become available in high quantities, because all these (physicochemical) parameters highly affect the upconversion luminescence properties and also their cellular uptake. The best synthetic strategies for high quality lanthanide-doped hexagonal (β) phase NaYF$_4$ UCLNPs are based on oil-phase methods. However, the respective UCLNPs cannot be dispersed in aqueous media, which is imperative for bio-applications [182,194]. This makes it mandatory to use post-processing surface modification protocols to allow for a phase transfer of hydrophobic UCLNPs into hydrophilic media [258]. Moreover, high colloidal stability and bio-compatibility as well as platforms for bio-conjugation are important prerequisites, which have to be satisfied in order to exploit the great potential of UCLNPs in the biophotonics field.

Variations in surface area-to-volume ratio, crystal structure, excitation power density, and lanthanide doping concentration influence the upconversion luminescence efficiency of colloidal UCLNPs [155,166]. Furthermore, surface bound compounds (*e.g.* C-H, N-H vibrational modes of stabilizing ligands) or hydroxyl groups in aqueous media are known quenchers [156,259,260]. This lowers the upconversion luminescence efficiency of UCLNPs dispersed in water significantly [261]. Photo-excitation of hydrophilic UCLNPs dispersed in aqueous media at 980 nm causes significant heating of water due to the fairly strong absorbance there ($\varepsilon = \sim 9 \cdot 10^{-3}$ M^{-1} cm^{-1}) [262]. Hence, the excitation power density for UCLNPs in bio-applications should be kept low. Despite recent progress, photophysics of UCLNPs dispersed in water with special emphasis on influences of surface ligands and water molecules are not fully understood yet.

In this work, we established a synthesis protocol yielding high quality hydrophobic UCLNPs of oleate-coated β-NaYF$_4$(Yb^{3+}/Er^{3+}) in approximately 2 g quantities for a single batch. Having in hands such large amounts of identical UCLNPs, it was possible to prepare colloidal dispersions in aqueous media using different surface modification strategies such as ligand exchange, amphiphilic coating, or silica coating. We then were able to study the effect of surface ligands and solvents on the photophysical properties of colloidally stable UCLNPs with identical optical and chemical properties.

5.3. Materials and Methods

5.3.1. Chemicals

Yttrium(III) chloride hexahydrate (99.99 %), ytterbium(III) chloride hexahydrate (99.9 %) were purchased from Treibacher Industrie AG (www.treibacher.com). Ammonium fluoride (ACS reagent ≥ 98.0 %), erbium(III) chloride hexahydrate (99.99%), sodium hydroxide (reagent grade ≥ 98.0 %), Igepal® CO-520, tetraethyl orthosilicate (TEOS), nitrosyl tetrafluoroborate (95 %), poly(isobutylene-*alt*-maleic anhydride) (PMA) average Mw ~ 6 kDa dodecylamine (98 %), 4-(aminomethyl)pyridine (98 %), N-(3-dimethylaminopropyl)-N′-ethylcarbodiimide hydrochloride (EDC), poly(acrylic acid sodium salt) (PAA) average Mw ~ 2.1 kDa, deuterium oxide (99.9 atom% D), poly(allylamine hydrochloride) (PAH) average Mw ~ 15 kDa, boric acid (99.999 %), and poly(sodium-4-styrenesulfonate) (PSS) average Mw ~ 15 kDa were purchased from Sigma-Aldrich (www.sigma-aldrich.com). α-Methoxy-ω-amino poly(ethylene glycol)-1200 (CH_3O-PEG-NH_2) average Mw ~ 1.2 kDa was from Rapp Polymere (www.rapp-polymere.com). Oleic acid (technical grade 90 %) and 1-octadecene (technical grade 90 %) were from Alfa Aesar (www.alfa.com). DSPE-mPEG(2000) (1,2-distearoyl-*sn*-glycero-3-phospho-ethanolamine-N-[methoxy(poly-ethylene glycol)-2000] (ammonium salt)) was purchased from Avanti Polar Lipids (www.avantilipids.com). Ammonia solution (32 %), tri-sodium citrate dihydrate, sulfuric acid (95-97 %), nitric acid (70 %) was from Merck (www.merckgroup.com). PEO 10 OH terminated phosphonic acid (PEG-PA) was from Specific Polymers (www.specificpolymers.fr). N,N-Dimethylformamide (DMF) (99.5 %), chloroform (99 %), tetrahydrofuran (THF) (99.8 %), and cyclohexane (99.5 %) were from Acros Organics (www.acros.com). All other reagents and organic solvents were of the highest grade available. Unless otherwise noted, all chemicals were used as received without further purification.

5.3.2. Instrumentation

Transmission electron microscopy (TEM) was performed using a 120 kV Philips CM12 microscope (www.fei.com). The size distributions of UCLNPs were evaluated from the TEM images using ImageJ software (http://rsbweb.nih.gov/ij/). We used the Zetasizer Nano-ZS

from Malvern (www.malvern.com) for dynamic light scattering experiments (DLS) with intensity-weighted distribution mode. X-ray powder diffraction (XRD) patterns with a resolution of 0.005° (2θ) were collected using a Huber Guinier G670 diffractometer (www.xhuber.com) with a Cu source (Kα radiation, λ = 1.54060 Å) operating at 40 kV and 30 mA. A Flame-EOP inductively coupled plasma optical emission spectrometer (ICP-OES) from Spectro (www.spectro.com) was used for the determination of the amount of rare-earth ions of UCLNPs. All centrifugation steps were carried out using a Hettich Universal 320 centrifuge (www.hettichlab.com). A Sonorex Digitech DT255H ultrasonic bath from Bandelin (www.bandelin.com) was used. Raman spectroscopy was performed using a DXR Raman microscope from Thermo Scientific (www.thermoscientific.com) with 532 nm CW laser excitation (8 mW). Upconversion luminescence spectra were recorded at room temperature with a calibrated luminescence spectrometer (LS 50 B) from Perkin Elmer (www.perkinelmer.com) modified with a 980 nm CW laser module (120 mW, 15 W cm^{-2}) from Roithner (www.roithner-laser.com) for upconversion photo-excitation [263]. Thermal gravimetric analysis (TGA) was performed using a Perkin-Elmer TGA 7 (www.perkinelmer.com). The synthesis was monitored using a 980 nm CW laser module (200 mW, ~ 10 W cm^{-2}) from Roithner (www.roithner-laser.com) for upconversion photo-excitation. The absolute determination of upconversion quantum yields was performed with a calibrated integrating sphere setup at the Federal Institute for Materials Research and Testing (BAM) in Berlin, Germany, equipped with an 8 W 980 nm laser diode at precisely controlled excitation power densities [264].

5.3.3. Large Scale Synthesis of Oleate-coated β-NaYF$_4$(Yb^{3+}/Er^{3+}) UCLNPs

The salts YCl$_3$·6H$_2$O (15.6 mmol), YbCl$_3$·6H$_2$O (4.0 mmol), and ErCl$_3$·6H$_2$O (0.4 mmol) were dissolved in ~ 40 mL of methanol by sonication. This solution was transferred into a 1 L three-necked flask, mixed with 160 mL of oleic acid and 300 mL of 1-octadecene under an atmosphere of nitrogen and heated to 160 °C. A homogeneous, clear solution was formed after 30 minutes at 160 °C under vacuum. The reaction mixture was then cooled to room temperature and 200 mL of methanol containing NaOH (0.25 M) and NH$_4$F (0.4 M) were added at once. The resulting colloidal suspension was stirred for 30 minutes at 120 °C under a gentle flow of nitrogen and then heated to reflux at ~ 320 °C for ~ 22 minutes. Visible green

upconversion luminescence can be observed by the bare eye at this point. Subsequently, the mixture was cooled to 200 °C. An additional heating step (> 300 °C for ~ 5 minutes) was applied. Afterwards, the mixture was cooled to room temperature. Oleate-coated hexagonal-phase UCLNPs were precipitated by addition of ~ 400 mL of ethanol after cooling to room temperature and isolated *via* centrifugation at a relative centrifugal force (RCF) of 1000 g for 5 minutes. The white pellet was washed three times by dispersing it in ~ 10 mL of chloroform and cyclohexane, and then precipitated by the addition of ~ 150 mL of ethanol and acetone. Finally, the purified OA-coated UCLNPs were dispersed in 160 mL of cyclohexane.

5.3.4.   Surface Modifications

5.3.4.1.   Modification with DSPE-mPEG2000

A method reported by Li *et al.* was used [265]. In detail, 2 mL of UCLNPs ($4 \cdot 10^{15}$ UCLNPs mL^{-1}) dispersed in cyclohexane were transferred into a 50 mL round bottom flask. Subsequently, the cyclohexane was evaporated under reduced pressure and the UCLNPs redispersed in 4 mL of chloroform. DSPE-mPEG(2000) (10 µmol) dissolved in 4 mL of chloroform was added, and the resulting mixture was sonicated for 3 minutes at room temperature. Then, the chloroform was evaporated under reduced pressure, which resulted in the formation of a colorless, transparent film on the bottom of the flask. Afterwards, the film was hydrated by addition of 10 mL of double-distilled water (dd water). A clear dispersion of UCLNPs coated with DSPE-mPEG(2000) was obtained. The dispersion was purified by three steps of centrifugation (RCF: 17000 g; 15 minutes) and subsequent redispersion in dd water. Finally, the coated UCLNPs were dispersed in 10 mL of dd water.

5.3.4.2.   Modification with Silica

A modified reverse-microemulsion technique for the silica coating of hydrophobic UCLNPs was used [266]. First, 2 mL of UCLNPs ($4 \cdot 10^{15}$ UCLNPs mL^{-1}) dispersed in cyclohexane were transferred into a 50 mL round bottom flask and diluted with 8 mL cyclohexane. Then, 500 µL of IGEPAL® CO-520 were added. The flask was sealed with a ground-in glass stopper and the clear dispersion was sonicated for 10 minutes. Afterwards, 80 µL of an aqueous ammonia solution (32%) were added and again sonicated for 10 minutes. Finally,

80 µL (0.27 mmol) of TEOS were added and the dispersion was magnetically stirred
(~ 600 rpm) for 24 hours at room temperature. The resulting silica-coated UCLNPs were
precipitated by adding 40 mL of acetone and collected *via* centrifugation (RCF: 1000 g;
5 minutes). The pellet was redispersed in 1 mL of chloroform, again precipitated with 10 mL
of acetone and collected *via* centrifugation. This step was repeated. The pellet was then
redispersed in 2 mL of sodium borate buffer (SBB; 50 mM, pH 12), precipitated again with
20 mL of acetone and collected *via* centrifugation. The UCLNPs were redispersed in 2 mL dd
water, precipitated with 20 mL of acetone and collected *via* centrifugation. This step was
repeated two times. Finally, the silica-modified UCLNPs were dispersed in 10 mL of
dd water.

5.3.4.3.   *Modification with Amphiphilic Polymer PMA*

The synthesis of the amphiphilic polymer (AP) has been reported previously [245,246]. In
more detail, 2.70 g (15 mmol) of dodecylamine (which acts as a hydrophobic side chain) were
dissolved in 100 mL of THF in a 250 mL round bottom flask. Once, dodecylamine dissolved
completely, all of the clear solution was poured into another 250 mL round bottom flask
containing 3.084 g of poly(isobutylene-*alt*-maleic anhydride), PMA, (20 mmol monomer;
corresponding to ~ 39 monomer units per polymer chain). PMA acts as a hydrophilic
backbone. The ratio of dodecylamine to the anhydride rings of PMA was chosen in a way that
~ 75 % of anhydride rings of the amphiphilic polymer backbone react with the amino groups
of hydrophobic side chain leaving ~ 25 % of anhydride rings intact for further modification
with other functionalities. The cloudy mixture was sonicated for a few seconds (~ 20 s) and
then refluxed at 55-60 ℃ for about three hours under magnetic stirring. Afterwards, the
solution was concentrated to 30-40 mL by evaporation of THF to enhance the reaction
between maleic anhydride rings of PMA backbones and the amino group of dodecylamine
side chains. Then, the solution was refluxed overnight under continuous stirring. The next
day, the solvent was completely evaporated under reduced pressure and the product was re-
dissolved in 400 mL anhydrous chloroform to give a final molar concentration of 0.05 M of
monomer units. This solution was used as a polymer stock solution (PSS).

Approximately 100 monomer units per nm^2 of UCLNP surface should be
applied [267,268]. The average particle diameter of oleate-coated UCLNPs is ~ 22.7 nm,
which was determined by the TEM analysis. The thickness of the organic shell, which

consists of oleate ions, around the inorganic β-NaYF$_4$(Yb^{3+}/Er^{3+}) core, is estimated as $\sim$ 1.1 nm [269,270]. The effective diameter (d_{eff}) is calculated to be $\sim$ 24.9 nm:

$$d_{eff} = (22.7\ nm) + (2 \cdot 1.1\ nm) = 24.9\ nm$$

Hence, the volume of PSS (V_{PSS}) needed for the amphiphilic polymer coating can be calculated according to Formula (3):

$$V_{PSS} = R_P \cdot \pi \cdot c_{UCLNPs} \cdot V_{UCLNPs} \cdot d_{eff}^2 \cdot c_{PSS}^{-1} \tag{3}$$

With:

R_P is the number of monomer units per nm^2 of UCLNP's surface area, which is in our case 100;

c_{UCLNPs} is $\sim$ 6.8$\cdot$10^{-7} M;

V_{UCLNPs} is 2$\cdot$10^{-3} L;

d_{eff} is $\sim$ 24.9 nm

c_{PSS} is 0.05 M

A volume (V_{PSS}) of $\sim$ 5 mL of PSS is needed in order to coat 2 mL of UCLNPs ($\sim$ 6.8$\cdot$10^{-7} M) with AP, resulting in $\sim$ 100 monomer units of AP per nm^2 of nanoparticle surface area.

The PSS polymer stock solution (5 mL; 0.05 M in chloroform) was mixed with 2 mL of oleate-coated UCLNPs ($\sim$ 6.8$\cdot$10^{-7} M) dispersed in cyclohexane. Immediately after mixing, sonication for 1 minute was applied. Afterwards, the solvent was slowly evaporated under reduced pressure until the sample was completely dry. The remaining solid film was redissolved in sodium borate buffer (SBB12; 50 mM, pH 12) under vigorous stirring until the solution turned clear. The resulting polymer-coated UCLNPs were purified using centrifuge filters (membrane: 100 kDa Mw cut off, PES). The dispersion of PMA-coated UCLNPs was pre-concentrated using a centrifuge filter (RCF: 870 g; 15 minutes) in order to give a volume

of less than 250 µL. At this step the reservoir of the filter was again filled with Milli-Q water to a volume of 10 mL and the pre-concentration of the diluted solution was repeated by centrifugation. The dilution/concentration sequence was repeated three times. Between each step the remaining UCLNPs dispersion was vigorously shaken in order to avoid aggregation of UCLNPs in the filter. In the final step, the sample solution was concentrated to a volume of 300 µL. Then, 150 µL of the concentrated sample were diluted with Milli-Q water giving a volume of 2 mL.

5.3.4.4.   Modification with Amphiphilic Polymer Py-PMA

The synthesis of the AP was modified in order to introduce pyridine ligands and dodecylamine into the hydrophilic backbone of PMA. 2.7 g (15 mmol) of dodecylamine were dissolved in 100 mL of THF and then 0.306 mL (3 mmol) of 4-(2-aminoethyl)pyridine were added. All further steps were the same as described in the section "5.3.4.3. Modification with Amphiphilic Polymer PMA".

5.3.4.5.   Modification with Amphiphilic Polymer PEG-PMA

The polymer coating procedure using PMA was carried out following the same procedure as described in the section "5.3.4.3. Modification with Amphiphilic Polymer PMA". Then, the amino-modified PEG (CH_3O-PEG-NH_2) was attached to the carboxyl-groups, which were present on the surface of the PMA-coated UCLNPs, by EDC chemistry [271]. In detail, a stock solution of 3 mM CH_3O-PEG-NH_2 with a molecular weight of ~ 1.2 kDa was prepared by dissolving 9 mg of PEG in 2.5 mL of sodium borate buffer (SBB9; 50 mM, pH 9). Afterwards, 227 µL of the PEG stock solution (3 mM) was added to 227 µL of the PMA-coated UCLNPs solution (7 µM), resulting in a ratio of 500 PEG molecules per UCLNP. Then, 227 µL of a freshly prepared EDC solution (384 mM in SBB9) was added, yielding a ratio of 64.000 EDC molecules per UCLNP within the reaction mixture. The samples were allowed to react for 3 hours before they were diafiltrated once with SBB9 on Centricon YM100 ultrafiltration devices. Finally, the sample solution was changed to Milli-Q water and concentrated to a volume of 300 µL. Then, 150 µL of the concentrated sample were diluted with Milli-Q water to a volume of 2 mL.

5.3.4.6. Modification with BF$_4^-$

We used a modified ligand-exchange strategy as reported by Dong *et al.* [272]. In detail, 8 mL of DMF were transferred into a 50 mL round bottom flask. Then, 10 mL of UCLNPs ($4 \cdot 10^{15}$ UCLNPs mL^{-1}) dispersed in cyclohexane were added. This resulted in a two phase system consisting of an upper layer of cyclohexane (containing the OA-coated UCLNPs) and a subjacent layer of DMF. Subsequently, 120 mg (1.0 mmol) of NOBF$_4$ were added at once under vigorous stirring. The mixture was further stirred for 10 minutes. This resulted in the phase transfer of the UCLNPs from the cyclohexane phase to the DMF phase. The UCLNPs within the slightly turbid DMF phase were precipitated by adding 20 mL of chloroform and collected *via* centrifugation (RCF: 1000 g; 5 minutes). The transparent pellet was redispersed in ~ 1 mL of DMF, precipitated again by addition of an excess of chloroform and collected *via* centrifugation. This step was repeated two times. Afterwards, the transparent pellet was redispersed in 10 mL of DMF and centrifuged (RCF: 1000 g; 3 minutes) in order to get rid of larger aggregates. This dispersion was used as a stock solution in all further ligand-exchange strategies.

5.3.4.7. Modification with Citrate

First, 2.5 g (8.5 mmol) of trisodium citrate dihydrate were dissolved in 4 mL of dd water. Then, 5 mL of the stock dispersion of UCLNPs in DMF (for preparation see section "5.3.4.6. Modification with BF$_4^-$") were slowly added under vigorous stirring. The turbid mixture was further stirred for 15 minutes. Afterwards, the dispersion was centrifuged for 5 minutes at 1000 g and the supernatant was discarded. The pellet was redispersed in 500 µL of dd water and centrifuged for 15 minutes at 14000 g. This step was repeated two times. Finally, the pellet was redispersed in 5 mL of dd water and centrifuged for 3 minutes at 1000 g in order to get rid of larger aggregates.

5.3.4.8. Modification with PEG-PA

We used 5 mL of the stock dispersion of UCLNPs in DMF (for preparation see section "5.3.4.6. Modification with BF$_4^-$") and added 80 mg (0.14 mmol) of PEG-PA dissolved in 1 mL of dd water under vigorous stirring. The turbid mixture was further stirred for 20 minutes. Afterwards, the dispersion was centrifuged for 15 minutes at 14000 g. The pellet was redispersed in 500 µL of dd water and again centrifuged for 15 minutes at 14000 g. This

step was repeated two times. Finally, the pellet was redispersed in 5 mL of dd water and centrifuged for 3 minutes at 1000 g in order to get rid of larger aggregates.

5.3.4.9. Modification with PAA

We used 5 mL of the stock dispersion of UCLNPs in DMF (for preparation see section "5.3.4.6. Modification with BF_4^-") and added 80 mg (0.04 mmol) of PAA dissolved in 1 mL of dd water under vigorous stirring. The following steps were the same as described in section "Modification with PEG-PA".

5.3.4.10. Modification using a Layer-by-Layer (LbL) Coating Strategy

The polyelectrolytes used for multilayer deposition were PAH and PSS [273,274]. They were dissolved in Milli-Q water to obtain stock solutions of 20 mg mL^{-1}. An amount of 1 mL of citrate-capped UCLNPs (0.68 µM) in dd water was added drop by drop and under vigorous stirring (1000 rpm) to a total volume of 1 mL of a stock solution of 20 mg mL^{-1} of PAH in order to adjust a ratio of polyelectrolyte chains of 100 per UCLNP. After mixing, the dispersion was stirred 1 hour and then centrifuged for 1 hour at 8000 rpm in 2 mL Eppendorf tubes; the supernatant was then carefully removed and replaced by ultrapure water. The centrifugation procedure was repeated. Then, the precipitated sample was redispersed in 1 mL Milli-Q water. This sample was then used to form the second layer consisting of PSS. It was added drop by drop and under vigorous stirring (1000 rpm) to a total volume of 1 mL of a stock solution of 20 mg mL^{-1} of PSS and left stirring for 20 minutes. Again, the sample was centrifuged for 1 hour at 8000 rpm. Then, the supernatant was replaced by ultrapure water and the centrifugation procedure was repeated. The third (PAH) and fourth (PSS) layers were prepared following the same procedure as used for the second layer. Finally, the sample was redispersed in 1 mL of Milli-Q water.

5.3.5. Sample Preparation for ICP-OES Measurements

Oleate-coated β-UCLNPs (0.3 mg) were solubilized in 417 µL of sulfuric acid (95-97 %). Afterwards, 7.083 mL double-distilled (dd) water and 7.5 mL of HNO_3 (1 M) were added. Finally, a clear solution with a total volume of 15 mL was obtained. The quantitative content of rare-earth ions of UCLNPs was determined using ICP-OES.

5.4. Results and Discussion

5.4.1. Large Scale Synthesis of Oleate-coated β-NaYF$_4$(Yb^{3+}/Er^{3+}) UCLNPs

Pure hexagonal-phase (β)-NaYF$_4$ nanocrystals doped with lanthanide ions can be prepared in solvent mixtures of oleic acid and 1-octadecene at 300 °C according to a method reported by Li *et al.* in 2008 [209]. This protocol is used by many research groups [275,276,277], but has disadvantages: (1) Temperature has to be well controlled and stabilized (300 °C for 1 hour); (2) Only ~ 100 mg of UCLNP are obtained in a batch. This is an essential drawback due to the fact that each batch results in particles that are slightly different in terms of size, shape, and elemental composition. All of these parameters strongly affect the upconversion luminescence properties [155,156].

The method presented here has several attractive features: (1) It yields β-UCLNPs in a single-batch reaction due to proper control of reaction conditions; (2) The process can be monitored with the bare eyes *via* the strong luminescence of the final product formed; and (3) Using our optimized synthesis protocol, a temperature stabilization at 300 °C can be omitted, since the reaction mixture is heated to reflux (~ 320 °C; see Figure 20). A diagram which documents the course of the temperature during synthesis is displayed in Figure 20a. A timer was started when the reaction mixture had reached 300 °C (see Figure 21). The onset of the crystallization of NaYF$_4$(Yb^{3+}/Er^{3+}) UCLNPs is characterized by the formation of small (~ 5 nm in diameter) cubic phase (α)-UCLNPs as the first (kinetic) product. This was proven by X-ray powder diffraction (XRD) and transmission electron microscopy (TEM). Subsequently, the α-UCLNPs are transformed to β-UCLNPs. Temperatures > 300 °C are required for phase transformation to occur [118]. As the α-UCLNPs disintegrate, the growth of larger β-UCLNPs can be observed. This step was

monitored using a 980 nm CW diode laser (~ 10 W·cm^{-2}) in order to excite the upconversion luminescence [278]. The laser power density was selected so that the upconversion luminescence produced by β-UCLNPs (~ 15 nm in diameter) could be monitored visually. Green upconversion luminescence of β-UCLNPs becomes visible (see Figure 20c) after approximately 22 minutes beyond 300 °C. XRD and TEM studies of a sample taken at this time verify the presence of smaller (~ 5 nm) α-UCLNPs and larger (~ 16 nm) β-UCLNPs. When using an even higher laser power density, the upconversion luminescence may be observed earlier, and therefore the final particle size may be smaller.
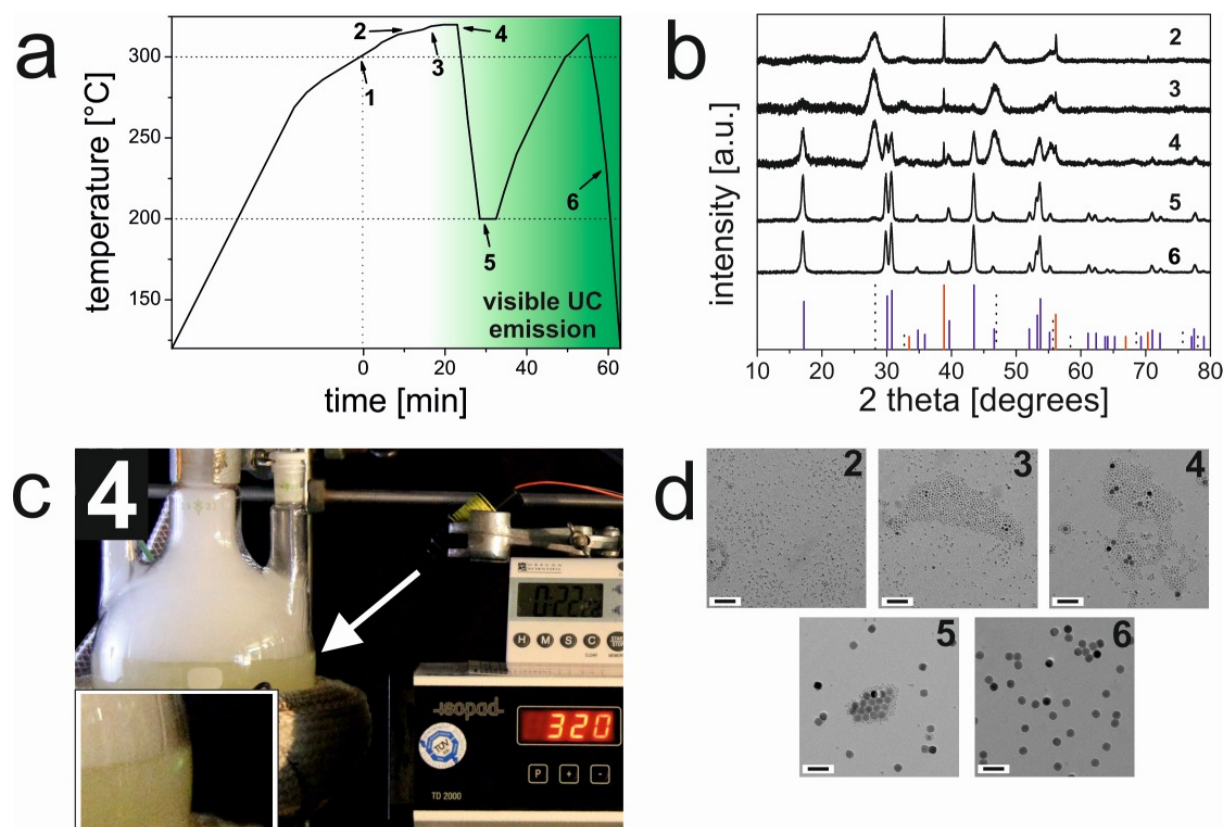
Figure 20 | Large scale synthesis of monodisperse β-NaYF$_4$(Yb^{3+}/Er^{3+}) UCLNPs. (**a**) Diagram showing the temperature protocol as a function of reaction time. The timer was started when the temperature of the reaction mixture had reached 300 °C (1). Samples taken from the reaction mixture were characterized by XRD (**b**) and TEM (**d**) after 10 (2), 15 (3), 22 (4), 27 (5), and 60 (6) minutes, respectively. (**c**) Image of the synthesis setup continuously illuminated with a 980 nm CW laser (~ 10 W·cm^{-2}). Green upconversion luminescence (see inset) was detectable after ~ 22 minutes (4). XRD reference patterns: cubic NaF (ICDD PDF #36-1455): red solid lines; cubic NaYF$_4$ (ICDD PDF #77-2042): black dotted lines; hexagonal NaYF$_4$ (ICDD PDF #16-0334): blue solid lines. Scale bars indicate 60 nm.
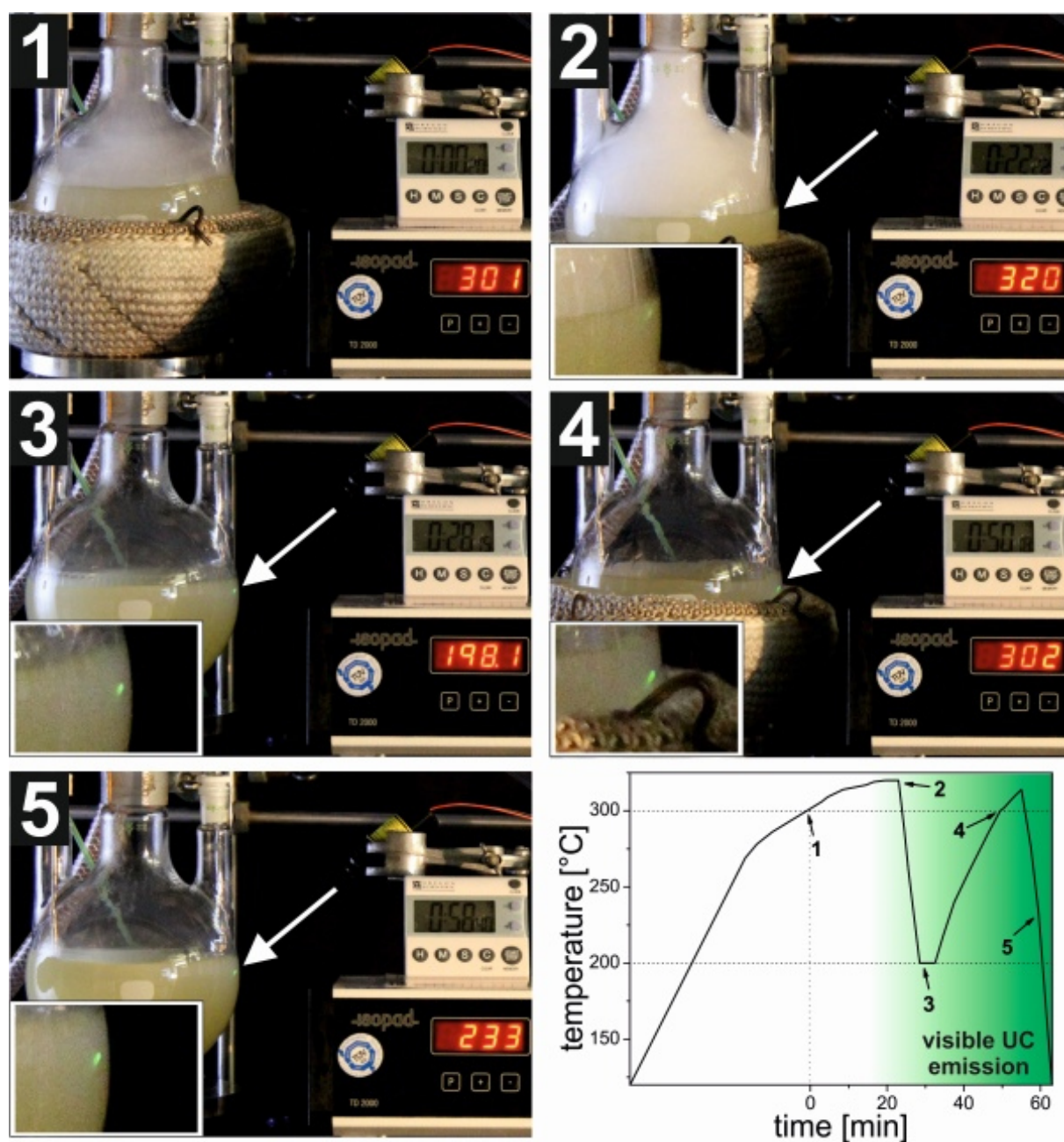
Figure 21 | Setup of a large scale synthesis of oleate-coated β-NaYF$_4$(Yb^{3+},Er^{3+}) UCLNPs. Once the reaction mixture had reached 300 °C a timer was started. The images were taken at 0 (1), 22 (2), 28 (3), 50 (4), and 58 (5) minutes, respectively. The diagram shows the course of the reaction mixture temperature as a function of time. Green upconversion luminescence (see inset) could be observed by the bare eye after ~ 22 minutes (2).

It is well known that the upconversion luminescence efficiency is about one order of magnitude higher for bulk lanthanide-doped hexagonal phase NaYF$_4$ than for the cubic phase [136]. However, efficiency decreases rapidly as the surface area-to-volume ratio increases due to non-radiative deactivation of excited state lanthanide ions by surface-bound

ligands and solvent molecules [279]. Thus, we presume that the difference in upconversion luminescence efficiency of smaller α-UCLNPs and larger β-UCLNPs is even higher than one order of magnitude. The subsequent occurrence of visible upconversion emission can be ascribed to the fast formation of β-UCLNPs within a few minutes.

Once the upconversion luminescence becomes visible, the reaction mixture is cooled to 200 °C since further heating would lead to a further growth of the β-UCLNPs which may result in a broader particle size distribution [280]. At 200 °C, the TEM image displays a bimodal particle distribution, *i.e.* one fraction of larger β-UCLNPs and a second fraction of smaller α-UCLNPs. This was further verified by XRD measurements (see Figure 20). In order to yield pure β-UCLNPs, an additional heating step (~ 5 minutes > 300 °C) was applied. This results in the disintegration of α-UCLNPs and a growth of β-UCLNPs, as again confirmed by TEM and XRD studies (see Figure 20).

The synthesis of monodisperse β-UCLNPs can be scaled up by a factor of 20 in comparison to Li's *et al.* protocol, and approximately 2 g of oleate-coated (OA) β-NaYF$_4$(Yb^{3+}/Er^{3+}) UCLNPs with purely hexagonal crystal structure can be obtained. This was the prerequisite to study for the first time the influence of the ligand attached to identical UCLNPs as will be shown below. An overview of surface modification strategies used in this work is displayed in Scheme 6. These strategies can be classified into two general groups: Type_Add and Type_Ex.

5.4.2.   Characterization of UCLNPs based on NaYF$_4$(Yb^{3+}/Er^{3+})

TEM images of OA-coated UCLNPs demonstrating the narrow size distribution (average diameter 22.7 ± 0.7 nm) and a uniform roughly spherical shape are displayed in Figure 22. The variation in size is as low as ~ 3 %. The inset in Figure 22a shows a single upconverting nanocrystal and the corresponding lattice fringes with a spacing of ~ 0.5 nm. XRD measurements (see Figure 22b) underpin the purely hexagonal crystal structure of NaYF$_4$(Yb^{3+}/Er^{3+}) UCLNPs as compared to the XRD pattern of standard Yb^{3+}/Er^{3+}-doped β-NaYF$_4$ (ICDD PDF #28-1192). The diameter as evaluated from the XRD experiments using Scherrer's equation is 23 ± 1.3 nm, which is in good agreement with the diameter obtained from the analysis of the TEM image [281].
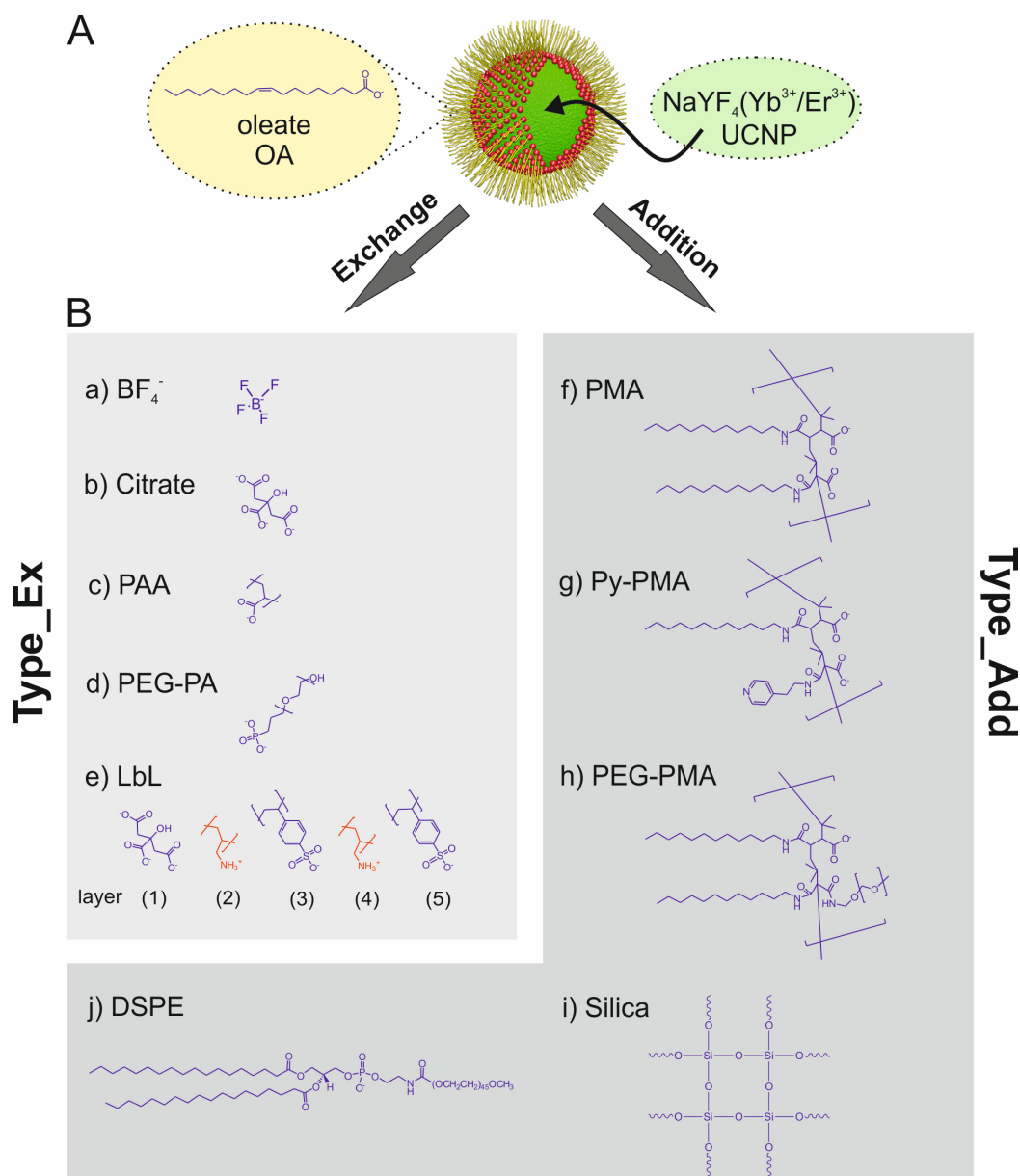
Scheme 6 | (A) Single oleate-coated (OA) UCLNP based on $NaYF_4(Yb^{3+}/Er^{3+})$. (B) Overview of surface modification strategies used in this work. The modifications can be classified into two categories: a)-e) ligand exchange methods (Type_Ex), and f)-j) addition of an amphiphilic layer or silica coating (Type_Add). Note: The oleate layer is still present for Type_Add modifications. Examples of Type_Ex modifications include coating with: a) tetrafluoroborate (BF_4^-); b) trisodium citrate (Citrate); c) poly(acrylic acid sodium salt) (PAA); d) poly(ethylene oxide)-10-OH terminated phosphonic acid (PEG-PA); e) layer-by-layer coating with poly(sodium-4-styrenesulfonate) (PSS) and poly(allylamine hydrochloride) (PAH) (LbL). Examples of Type_Add modifications include coating with: f) poly(isobutylene-alt-maleic anhydride) modified with dodecylamine (PMA); g) same as f) but with further modification with 4-(aminomethyl)pyridine (Py-PMA); h) same as f) but with further modification with α-methoxy-ω-amino poly(ethylene glycol)-1200 (PEG-PMA); i) silica coating with a shell thickness of ~5 nm (Silica); and j) 1,2-distearoyl-sn-glycero-3-phospho-ethanolamine-N-[methoxy(poly-ethylene glycol)-2000] (ammonium salt) (DSPE).
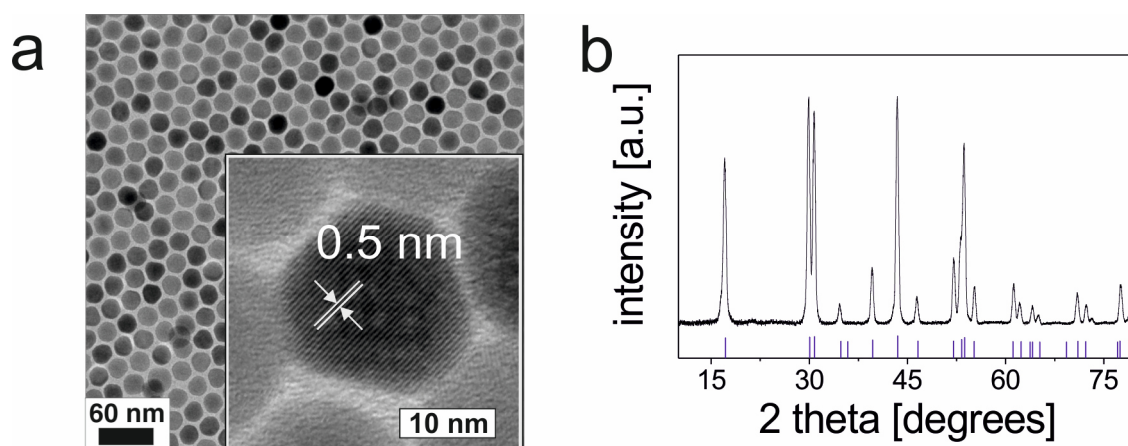
Figure 22 | Characterization of UCLNPs. (**a**) TEM image of β-NaYF$_4$(Yb^{3+}/Er^{3+}) UCLNPs coated with oleate (OA). The inset displays lattice fringes of a single UCLNP with a lattice spacing of ~ 0.5 nm. (**b**) UCLNPs produced by our method exhibit purely hexagonal crystal structure of NaYF$_4$ as compared to the XRD standard pattern ICDD PDF #28-1192.

Dynamic light scattering (DLS) experiments of OA-coated UCLNPs based on an intensity-weighed size distribution model revealed a solvodynamic diameter of 29 ± 3 nm with a polydispersity index (PdI) of 0.19 in cyclohexane (see Figure 23a). Additionally, the rare-earth ion content of β-NaYF$_4$(Yb^{3+}/Er^{3+}) UCLNPs was determined using inductively ICP-OES. The fractions are 78.4 ± 0.1 mol% of Y^{3+}, 19.3 ± 0.1 mol% of Yb^{3+}, and 2.3 ± 0.1 mol% of Er^{3+}, respectively. These values are in good agreement with the concentrations calculated from the amounts of lanthanide ions applied in synthesis (see Table 3). This demonstrates that these UCLNPs prepared on a large scale clearly are of excellent quality in terms of size distribution, shape uniformity, elemental composition, and crystal phase.

Table 3 | Content of rare-earth ions of NaYF$_4$(Yb^{3+},Er^{3+}) UCLNPs

Element	Concentration [μM]	Content [mol%]	Theoretical Content$^{(*)}$ [mol%]
Yttrium	319.5 ± 0.3	78.4 ± 0.1	78.0
Ytterbium	78.8 ± 0.4	19.3 ± 0.1	20.0
Erbium	9.2 ± 0.1	2.3 ± 0.1	2.0

$^{(*)}$Theoretical content as revealed from the original sample weight.
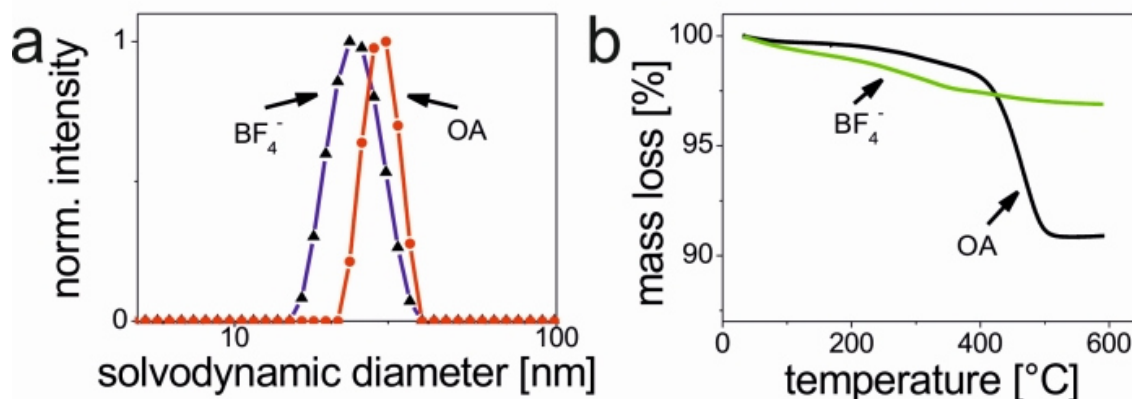
Figure 23 | (**a**) The solvodynamic diameter (intensity-weighted distribution) of OA-coated UCLNPs in cyclohexane is 29 nm (PdI 0.189), and 24 nm (PdI 0.089) for BF$_4^-$-coated UCLNPs (BF$_4^-$) in DMF. (**b**) TGA experiments showing the relative mass loss of OA-coated and BF$_4^-$-coated UCLNPs being ~ 9.1% and ~ 3.1%, respectively.

5.4.3. Quantification of Oleate Surface Ligands

Thermal gravimetric analysis (TGA) experiments under a nitrogen atmosphere with a heating rate of 10 °C min^{-1} were performed in the temperature range of 35 to 600 °C (see Figure 23b). A relative mass loss of ~ 9.1 % can be observed for initially oleate-coated UCLNPs. One can calculate the number of oleate ions per UCLNP from the absolute mass loss and the density of hexagonal NaYF$_4$ (4.21·10^{-21} g nm^{-3}) [282]. The volume of one UCLNP (V_{UCLNP}) was calculated using Formula (4) , assuming a spherical particle shape:

$$V_{UCLNP} = \frac{4}{3}\left(\frac{d}{2}\right)^3 \pi \tag{4}$$

With d = 22.7 nm (obtained from evaluation of TEM images) the volume of one UCLNP (V_{UCLNP}) is ~ 6.1·10^3 nm^3.

The average mass of one single UCLNP (m_{UCLNP}) is calculated using Formula (5):

$$m_{UCLNP} = \rho_{NaYF_4} \cdot V_{UCLNP} \qquad (5)$$

With: $\qquad \rho_{NaYF_4} = 4.21 \cdot 10^{-21}$ g nm^{-3}

$V_{UCLNP} = 6.1 \cdot 10^3$ nm^3

$$m_{UCLNP} = \sim 2.6 \cdot 10^{-17} \text{g}$$

The average mass of one single UCLNP (m_{UCLNP}) is $\sim 2.6 \cdot 10^{-17}$ g.

The mass of the OA-sample did not change above $\sim 500\,°C$ as can be seen from the thermogram (see Figure 23b). The absolute mass (m_{abs}; 15.162 mg) at 500 °C was considered as the mass of plain UCLNPs (plUCLNPs) without any surface ligands. The number of plUCLNPs ($N_{plUCLNPs}$) is calculated using Formula (6):

$$N_{plUCLNPs} = \frac{m_{abs}}{m_{UCLNP}} \qquad (6)$$

With: $\qquad m_{abs} = 15.162 \cdot 10^{-3}$ g

$m_{UCLNP} = 2.6 \cdot 10^{-17}$ g

$$N_{plUCLNPs} = \sim 5.8 \cdot 10^{14}$$

The number of plUCLNPs ($N_{plUCLNPs}$) is ~ $5.8 \cdot 10^{14}$.

The number of oleate (OA) ions (N_{oleate}) was calculated from the absolute mass loss (m_{abs_OA}) of the TGA experiment (1.53 mg) using Formula (7). Here, it is assumed that the absolute mass loss is only due to the loss of oleate ligands:

$$N_{oleate} = \frac{m_{abs\_OA}}{M(OA)} \cdot N_A \qquad (7)$$

With: $m_{abs\_OA} = 1.53 \cdot 10^{-3}$ g

$M(OA) = 281.45$ g·mol^{-1}

$N_A = 6.022 \cdot 10^{23}$ mol^{-1}

$$N_{oleate} = \sim 3.3 \cdot 10^{18}$$

The number of oleate (OA) ions (N_{oleate}) is ~ $3.3 \cdot 10^{18}$

The number of OA ions per one single UCLNP $\left(N_{\frac{oleate}{UCLNP}} \right)$ is calculated using Formula (8):

$$N_{\frac{oleate}{UCLNP}} = \frac{N_{oleate}}{N_{plUCLNPs}} \qquad (8)$$

With: $N_{oleate} = 3.3 \cdot 10^{18}$

$N_{plUCLNPs} = 5.8 \cdot 10^{14}$

$$N_{\underline{oleate}\atop UCLNP} = \sim 5.7 \cdot 10^3$$

The number of OA ions per one single UCLNP $\left(N_{\frac{oleate}{UCLNP}} \right)$ is $\sim 5.7 \cdot 10^3$.

The surface area of one UCLNP (A_{UCLNP}) was calculated using Formula (9):

$$A_{UCLNP} = 4 \cdot \pi \cdot \left(\frac{d}{2} \right)^2 \tag{9}$$

With d = 22.7 nm (obtained from evaluation of TEM images) the surface area of one UCLNP A_{UCLNP} is $\sim 1.6 \cdot 10^3$ nm^2.

Assuming a diameter of an oleate ions of ~ 0.5 nm, their area (cross section) is ~ 0.2 nm^2 [283]. The surface area of one UCLNP, which is covered by oleate ions, can be calculated from these results to be $\sim 1.1 \cdot 10^3$ nm^2. This means that $\sim 70\,\%$ of the UCLNP surface is covered by oleate ions.

5.4.4.   Surface Modifications

Nine commonly applied approaches (overview shown in Scheme 6) for surface modification of hydrophobic nanomaterials (*e.g.* quantum dots, magnetic nanoparticles) were investigated [220]. These modifications can be classified into two general groups (see Scheme 7).
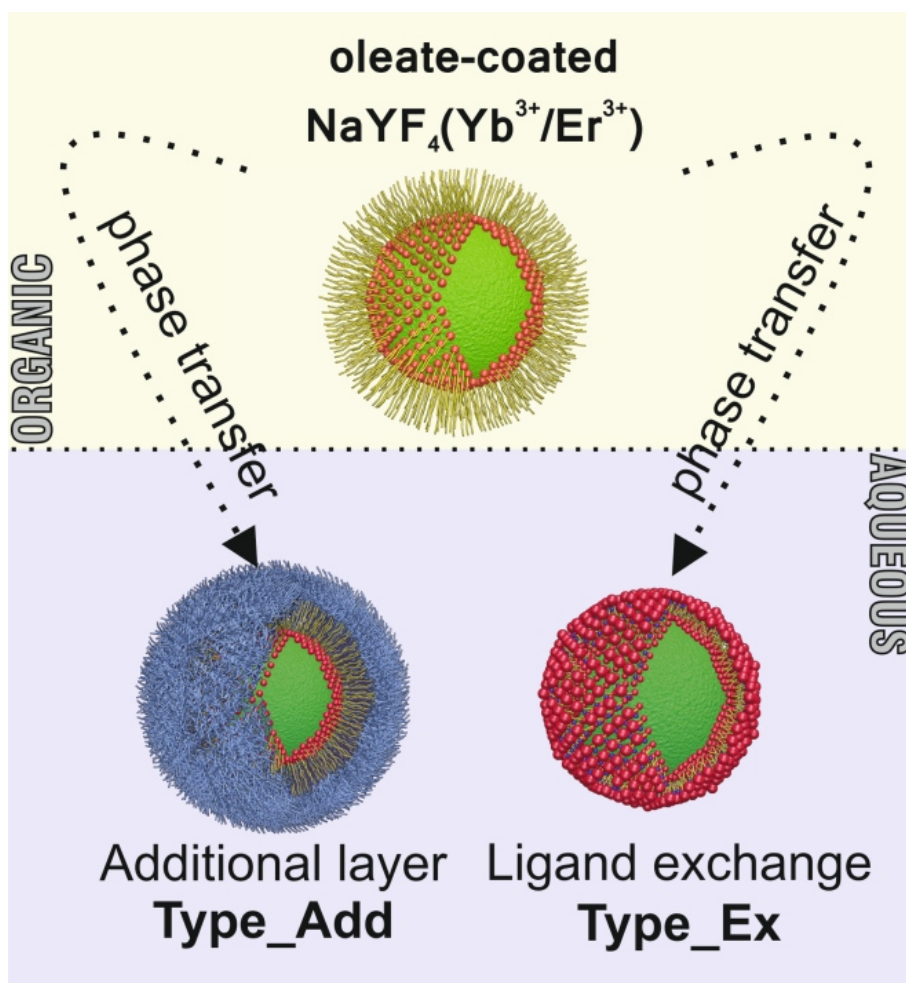
Scheme 7 | Phase transfer strategies for rendering hydrophobic UCLNPs dispersible in aqueous media. Initially, UCLNPs based on β-NaYF$_4$(Yb^{3+}/Er^{3+}) are coated by OA ligands and therefore only dispersible in non-polar solvents. The surface modifications employed here can be classified into two general groups: (1) In Type_Add, the OA ligands are preserved and an additional layer is formed for example by amphiphilic molecules, polymers, silica. (2) In Type_Ex, exchange of OA ligands are replaced by water-soluble molecules or polymers.

5.4.4.1.   Surface Modifications via Additional Layer Strategies

The first group comprises surface modifications that make use of an additional shell on top of the OA layer (Type_Add). Here, we used amphiphilic molecules (DSPE), amphiphilic polymers (PMA, Py-PMA, PEG-PMA), or a silica shell (shell thickness ~ 5 nm). These modifications are attractive for (bio)-analytical applications of hydrophobic nanoparticles due to their great stability and capability for further bioconjugation [245,246,265,268]. The hydrodynamic diameter and Zeta potential values of these modifications are summarized in Table 4. The corresponding TEM images are shown in Figure 24.

Phospholipids are amphiphilic molecules which comprise a major component of cell membranes. Coatings using phospholipids such as DSPE for engineering of surface properties may afford biocompatibility by mimicking the composition and functionality of cell's external membrane. Lipids with various functional headgroups (*e.g.* COOH, NH$_2$, SH, maleimide, biotin) are commercially available and allow for easy functionalization of UCLNPs. The physical surface properties can be fine-tuned to be positive, negative, or zwitterionic by using phospholipids with different charged headgroups. However, one drawback of this method is the relatively high price of functionalized phospholipids [265].

Amphiphilic polymers are a cheaper alternative to such high pricy functionalized phospholipids. The hydrophobic backbone of amphiphilic polymers such as PMA or Py-PMA can intercalate the hydrophobic oleate layer of UCLNPs to form a polymer shell. The water solubility of the polymer-coated UCLNPs is ensured by the hydrophilic carboxyl groups located on the outer region of the polymer shell [245]. These modifications exhibit excellent colloidal stability in aqueous media with high Zeta potential values (Table 4). In addition, carboxyl groups offer platforms for further functionalization. For example, amino-modified PEG molecules can be covalently linked to carboxyl groups *via* EDC chemistry. This additional PEG coating may afford UCLNPs with a prolonged circulation half-life and reduced unspecific binding [284,285].

Silica encapsulation is another elegant method to transfer hydrophobic UCLNPs into water [200]. A stable silica shell with a thickness of ~ 5 nm was prepared by a water-in-oil (reverse) microemulsion technique which renders UCLNPs water-dispersible and facilitates the integration of functional groups for subsequent bioconjugation [247,286].

5.4.4.1. *Surface Modifications via Ligand Exchange Strategies*

The second group includes modifications that are based on the complete exchange of the OA ligands with another ligand (Type_Ex). The hydrodynamic diameter and Zeta potential values of these modifications are summarized in Table 4. The corresponding TEM images are shown in Figure 24.

In 2011, Dong *et al.* reported a general strategy for ligand exchange using nitrosonium tetrafluoroborate (NOBF$_4$) to replace OA ligands attached to the UCLNPs surface [272]. This procedure enables the phase transfer of initial hydrophobic UCLNPs into

polar, hydrophilic media such as N,N-dimethylformamide (DMF). BF$_4^-$-coated UCLNPs exhibit a solvodynamic diameter of 24 nm (PdI 0.089) as revealed by DLS experiments in DMF dispersion (see Figure 23a). A TEM image of BF$_4^-$-coated UCLNPs is shown in Figure 24.

Table 4 | Summary of the results of the DLS measurements and Zeta potential values.

	Ligand[a]	Hydrodynamic diameter[b] [nm]	PdI[c]	Zeta potential[d] [mV]
Additional layer	PMA	34	0.176	-53
	PEG-PMA	35	0.147	-52
	Py-PMA	39	0.091	-51
	Silica	42	0.223	-32
	DSPE	53	0.098	-9
Ligand exchange	PAA	37	0.199	-36
	LbL	33	0.182	-34
	Citrate	24	0.025	-25
	PEG-PA	77	0.181	18

(a) For full names of ligands see Scheme 6.
(b) DLS results based on an intensity-weighed size distribution model.
(c) Polydispersity index.
(d) Zeta potential in dd water at pH 7 (UCLNPs concentration 10 mg·mL^{-1})

Additionally, it is demonstrated that hydrophilic BF$_4^-$-stabilized UCLNPs can be covered with polymers (PAA) or small molecules (citrate and PEG-PA) using a sequential coating step. Citrate-coated UCLNPs can be further modified through the sequential deposition of positively and negatively charged polymers (PAH and PSS) based on a Layer-by-Layer (LbL) strategy to form (PSS/PAH/PSS/PAH/citrate/UCLNP). Particles modified by this strategy offer the ability to minimize the distance of a receptor or a probe to the luminescent UCLNP, enabling a more efficient energy transfer in (bio)-analytical sensor applications.

Stable, optically transparent colloids resulted from all of the nine surface modifications dispersed in double-distilled water at pH 7.
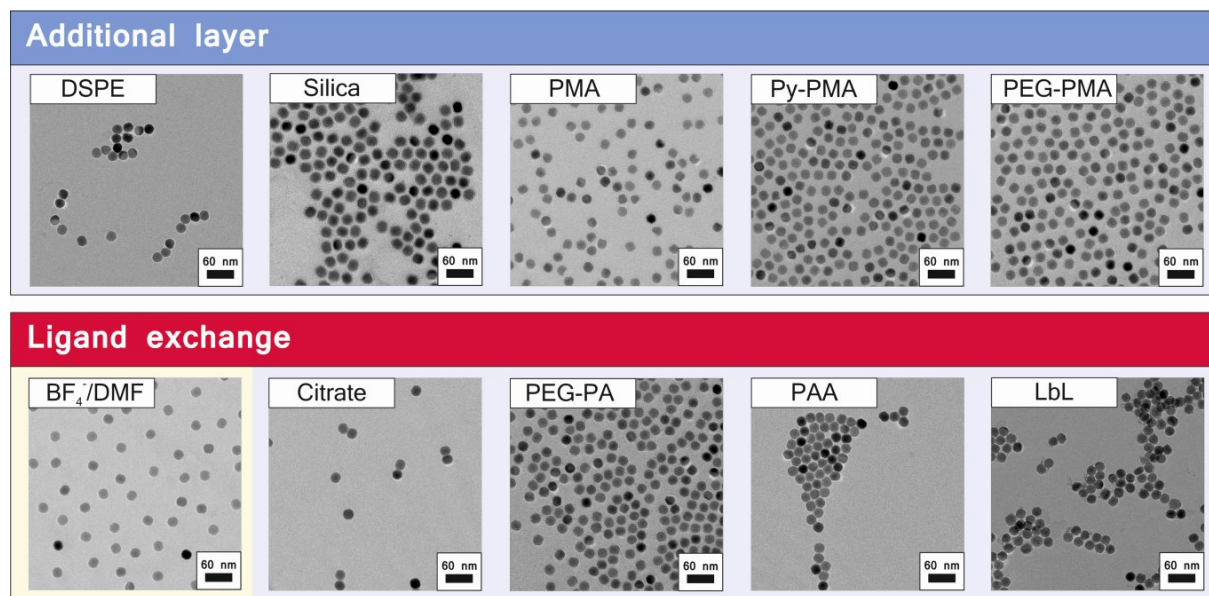
Figure 24 | TEM images of UCLNPs modified by additional layer (Type_Add) and ligand exchange (Type_Ex) surface coatings, respectively. Scale bars indicate 60 nm.

5.4.5.   Luminescence Properties

UCLNPs based on β-NaYF$_4$(Yb^{3+}/Er^{3+}) display two dominant anti-Stokes-shifted emission peaks at 545 nm and 658 nm, respectively, upon 980 nm CW laser excitation with a full width at half maximum (FWHM) of ~ 16 nm and ~ 19 nm, respectively (see Figure 25). In contrast to other luminescent nanomaterials (*e.g.* quantum dots), the spectral positions of the emission peaks are not influenced by UCLNP size. The size of UCLNPs, however, has a tremendous effect on their upconversion luminescence intensity [156,287]. Our OA-coated β-NaYF$_4$(Yb^{3+}/Er^{3+}) UCLNPs (22.7 nm in diameter) dispersed in cyclohexane exhibit a quantum yield (QY) of ~ 0.35 % if excited with a power density of 150 W·cm^{-2}, measured absolutely with an integration sphere setup [264]. In 2010, Boyer *et al.* reported QY measurements of OA-coated β-NaYF$_4$(Yb^{3+}/Er^{3+}) UCLNPs dispersed in hexane. The QY of UCLNPs with a diameter of 30 nm determined at the same excitation power density was ~ 0.1 % and decreased by a factor of 20 for UCLNPs with diameters of 8-10 nm (QY

~ 0.005 %) [279]. This size-dependent decrease in upconversion luminescence efficiency of UCLNPs is commonly ascribed to an increase in their surface area-to-volume ratio, with surface defects as well as ligands and solvent molecules favoring the non-radiative deactivation of electronically excited states. As a consequence, this could suggest that our optimized synthesis protocol yields UCLNPs exhibiting less surface defects, since our smaller UCLNPs (22.7 nm vs. 30 nm) have a three times higher QY in comparison to UCLNPs from Boyer *et al.*

In aqueous dispersions the QYs of DSPE-modified UCLNPs (representative of Type_Add modifications) and citrate-modified UCLNPs (representative of Type_Ex modifications) are approximately two times lower than in cyclohexane at an excitation power density of 150 $W \cdot cm^{-2}$, demonstrating the known quenching effect of water, related to its high energy vibration modes [281].

A second surprising finding is the alteration of the relative intensities of the upconversion emission peaks in water dispersion [201,288]. This follows from a comparison of the luminescence spectra of all surface-modified UCLNPs shown in Figure 25 that were measured under identical conditions upon 980 nm CW laser excitation (15 $W \cdot cm^{-2}$) and normalized at 658 nm. In this respect, the two general phase transfer strategies for OA-coated UCLNPs (Type_Add and Type_Ex) can be clearly distinguished (see Figure 25) by the different intensity ratios ($I_{g/r}$) of upconversion emission maxima at 545 nm (green; g) and at 658 nm (red; r), with the ratio $I_{g/r}$ of Type_Add and Type_Ex surface-modified UCLNPs being ~ 0.7 and ~ 0.5, respectively (see Figure 25b and Figure 25c). This is due to the presence of OA ligands (Type_Add), which cover ~ 70 % of UCLNPs surface and sufficiently prevent direct access of water molecules to the particle surface. Furthermore, when comparing the spectra of water dispersible UCLNPs with those of the same particles with OA coating dispersed in cyclohexane (see Figure 25a), the impact of H_2O on the relative intensities of both emissions becomes obvious. The intensity of the emission at 545 nm drops by a factor of ~ 3 regardless of the type of surface engineering performed to achieve phase transfer.

To gain further insight in the luminescence behavior of our UCLNPs, we compared the relative luminescence intensities in H_2O and D_2O. D_2O can prevent luminescence quenching of excited lanthanide ions caused by high energy O-H vibrational modes. The corresponding normalized upconversion emission spectra are displayed in Figure 26. As expected, a strong increase in the ratio $I_{g/r}$ is observed in D_2O (factors of ~ 6 and ~ 9

for Type_Add and Type_Ex modifications, respectively). It is also possible to distinguish between both types of surface modifications dispersed in D_2O, with Type_Ex modifications exhibiting a significantly higher ratio $I_{g/r}$ compared to Type_Add modifications. We attribute this effect to luminescence quenching caused by the C-H vibrational modes of OA ligands and amphiphilic coating compounds.
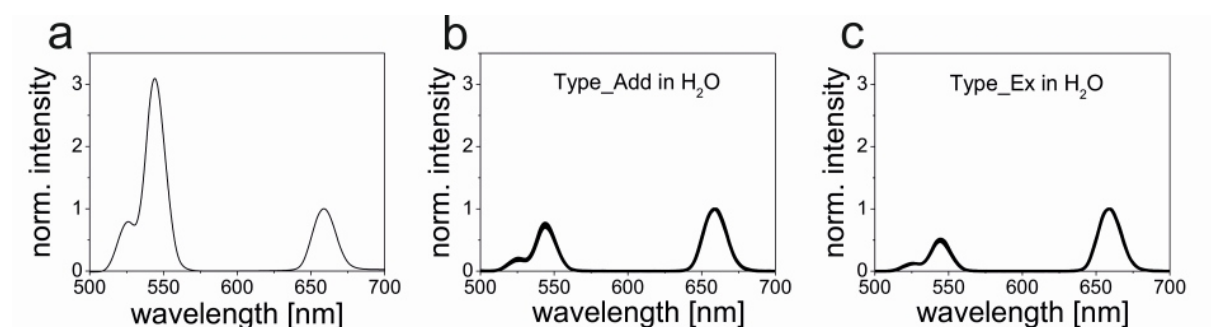
Figure 25 | Normalized upconversion luminescence spectra of UCLNPs. Spectra were aquired upon 980 nm CW laser excitation with a power density of 15 W·cm^{-2} and are normalized at 658 nm. (**a**) Spectrum of OA-coated UCLNPs in cyclohexane ($I_{g/r} \sim 3$); (**b**) Five spectra of Type_Add surface-modified UCLNPs dispersed in H_2O ($I_{g/r} \sim 0.7$); (**c**) Four spectra of Type_Ex surface-modified UCLNPs dispersed in H_2O ($I_{g/r} \sim 0.5$).

Based on these results, two suggestions using surface-modified UCLNPs for self-referenced sensing can be made: (a) Type_Add modifications exhibit a higher dynamic range of the $I_{g/r}$, which is beneficial for sensing schemes according to inner filter effects. Here UCLNPs act as nanolamps for the excitation of sensor probes [224,225,226]. (b) Ligand exchange modifications (Type_Ex) could be beneficial for the design of sensors utilizing fluorescence energy transfer processes (FRET), since the distance between donors (lanthanide ions) and acceptors can be minimized.
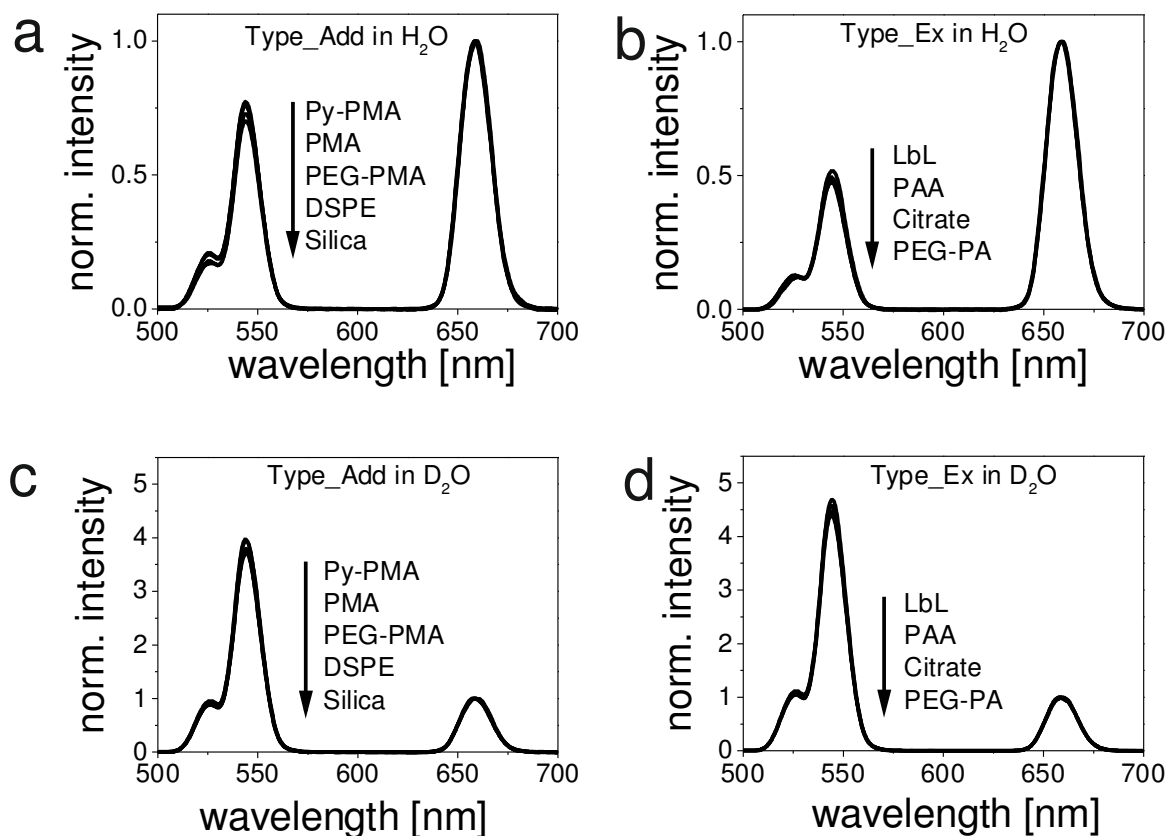
Figure 26 | Normalized upconversion luminescence spectra of Type_Add and Type_Ex surface-modified UCLNPs. All spectra were aquired upon 980 nm CW laser excitation (15 W cm^{-2}) and normalized at 658 nm. (**a**) Type_Add surface-modified UCLNPs dispersed in water ($I_{g/r} \sim 0.7$); (**b**) Type_Ex surface-modified UCLNPs dispersed in water ($I_{g/r} \sim 0.5$); (**c**) Type_Add surface-modified UCLNPs dispersed in D$_2$O ($I_{g/r} \sim 4$); (**d**) Type_Ex surface-modified UCLNPs dispersed in D$_2$O ($I_{g/r} \sim 4.7$).

5.5.   Conclusion

We developed an optimized protocol for the synthesis of oleate-capped β-NaYF$_4$(Yb^{3+}/Er^{3+}) UCLNPs that enables their preparation on a large scale with an extremely narrow size-distribution, pure crystallinity, and comparatively high QY. Nine different surface modifications of identical water-dispersible β-UCLNPs were characterized in their colloidal stability. The brightness of phase-transferred UCLNPs is significantly reduced compared to the oleate-coated UCLNPs due to non-radiative decay of excited states of lanthanide ions

caused by surface ligands and water molecules. A closer look at the upconversion emission intensity ratios revealed that for the nine commonly used surface modifications only two intensity ratios can be observed. This allows for the differentiation between the two sets of surface modification principles. From these results it can be concluded, that for bioimaging applications water-dispersibility introduced by an additional amphiphilic layer leads to UCLNPs which perform better. In contrast, for self-referenced sensors based on non-radiative energy transfer processes, ligand exchange modifications may be of advantage since the distance between donors and acceptors can be efficiently reduced. Additionally, it is expected that an analysis of upconversion intensity ratios of UCLNPs may become a powerful tool in monitoring the growth and formation of regular, homogenous, and compact shells. This principle may allow for a luminescence-controlled characterization of core-shell architectures of UCLNPs.

Acknowledgments

6.   Perspectives of Upconverting Luminescent Nanoparticles

Upconverting luminescent nanoparticles (UCLNPs) constitute a novel type of contrast agent for noninvasive *in vivo* luminescence bioimaging due to their unique optical properties [289]. They are capable of emitting visible light upon NIR excitation (anti-Stokes emission) enabling improved detection sensitivity and autofluorescence-free background imaging in comparison to commonly used luminescent labels which are excited by UV or visible light [290]. The advantages of UCLNPs for (bio)-analytical applications include high photostability, non-blinking emissions, large anti-Stokes shifts, and sharp emission bands. However, there are still some limitations and challenges which will be discussed in this chapter. Finally, new trends for an improved design and performance of UCLNPs will be introduced.

6.1.   Absorption of 980 nm Excitation Light by Water

The spectral range from ~ 650 nm to ~ 900 nm is known as the near-infrared biological window (NIR window; therapeutic window; or optical window) [295]. This window (see Figure 27) is characterized by a minimal absorption coefficient of tissue pigments (such as hemoglobin or melanin) and water. Hence, light of this particular wavelength (650-900 nm) can penetrate deeper into tissue than visible light which is beneficial for *in vivo* imaging applications and light-driven therapeutics [291,292].

The absorption maximum of Yb^{3+} ions is located around 980 nm. These ions are employed as sensitizers in lanthanide-doped UCLNPs. A 980 nm NIR laser is commonly used to excite UCLNPs. However, water as the most significant component in all creatures has a local absorption maximum at 980 nm. The absorption coefficient of water at 980 nm is

~ 0.485 cm^{-1} [293]. Therefore, the utilization of 980 nm laser in (bio)-imaging has the disadvantage that excitation light is overwhelmingly attenuated while diffusing into biological tissue which limits its penetration depth. Moreover, light with a wavelength of 980 nm can lead to local overheating of the biological sample and induce tissue damage. Interestingly, 980 nm radiation has been used as an optical heating source in laser thermal therapy due to the strong absorption of water at this wavelength [294]. In consequence, a shift of the excitation wavelength of UCLNPs into the NIR window, where absorption of water is significantly lower than at 980 nm, would be of great advantage.
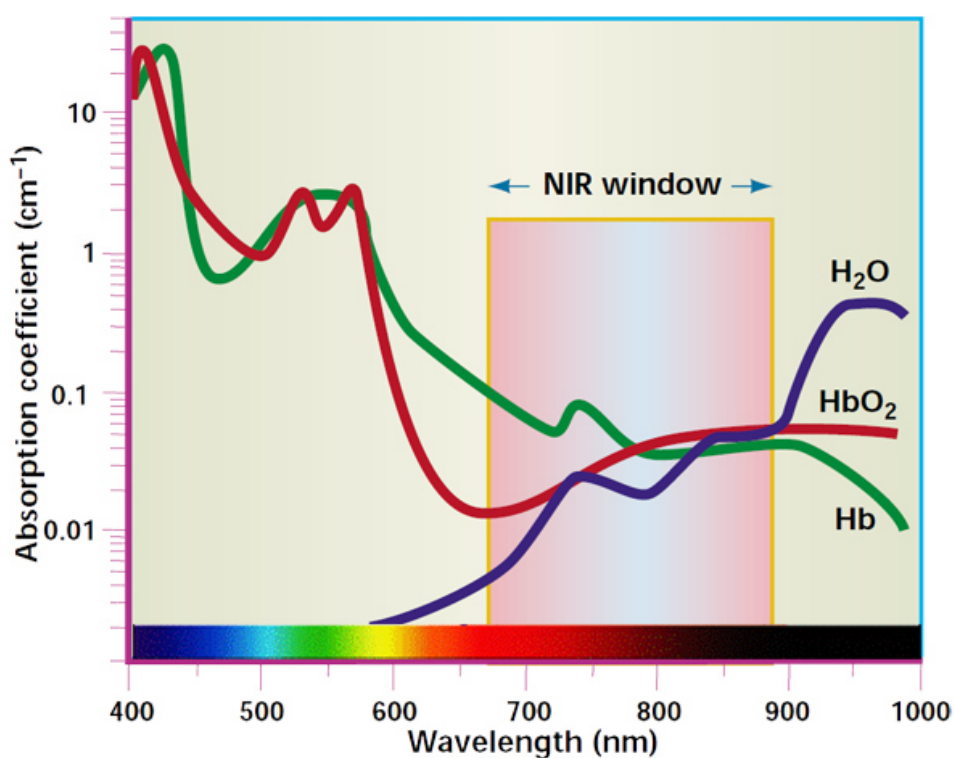
Figure 27 | Near-infrared biological window. The absorption coefficients of H_2O and hemoglobin are displayed as a function of wavelength. Reprinted by permission from Macmillan Publishers Ltd: Nature Biotechnology, copyright (2001) [295].

6.2.   Excitation Power Density-dependent Quantum Yield

Upconversion luminescence refers to nonlinear optical phenomena. The upconversion luminescence intensity (I) scales proportionally to the nth power of the excitation power density (I_{ex}) according to Formula (10):

$$I \propto I_{ex}^{n} \qquad\qquad (10)$$

Here, n is the number of photons absorbed. The theoretical model for this power density dependency was developed by Pollnau *et al.* and Suyver *et al.* [296,297]. They showed that this relationship is only valid in a limited range of excitation power densities since saturation effects occur at high power. As a result, the quantum yield of upconversion luminescence processes of UCLNPs exhibits an excitation power density-dependent behavior [298]. The determination of the excitation power density is of great importance for quantum yield (QY) measurements of UCLNPs [261].

The QY of UCLNPs can be measured absolutely using an integration sphere setup. Figure 28 displays the QY of UCLNPs as a function of excitation power density in the range from ~ 6 to ~ 1600 W·cm^{-2}. The diameter of UCLNPs is 22.7 ± 0.7 nm. Data of their detailed characterization (TEM, XRD, ICP-OES, DLS, *etc.*) can be found in Chapter 5. The QY of oleate-coated UCLNPs dispersed in cyclohexane is ~ 0.02 % at ~ 6 W·cm^{-2} and increases linearly with increasing excitation power density. Beyond ~ 100 W·cm^{-2} a deviation from this linear increase can be observed due to saturation effects. A saturated QY of ~ 1 % was measured. A similar behavior could be found for DSPE-coated UCLNPs dispersed in water. However, their saturation QY is ~ 0.5 %. Moreover, the QY at ~ 6 W·cm^{-2} is as low as ~ 0.005 % which can be attributed to strong quenching effects caused by O-H vibrational modes of water molecules [281]. It is worth pointing out that the conservative limit for human skin exposure at 980 nm equals 726 mW·cm^{-2} [172,299]. Therefore, the utilization of pulsed excitation with a high power density rather than continuous excitation is suggested for bioimaging applications of UCLNPs in order to limit the heating of tissue [166,289]. In doing so, the QY of UCLNPs is maximized since the power density of the excitation light can be increased.
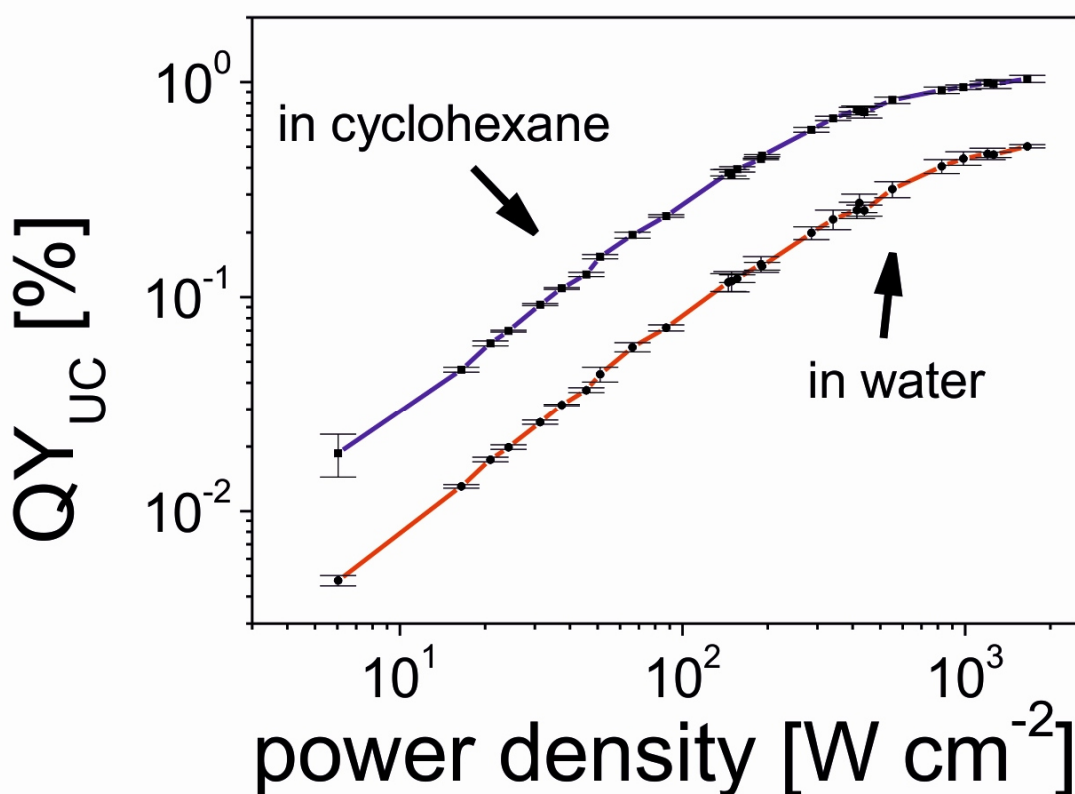
Figure 28 | *Excitation power density-dependent QY measurements of UCLNPs dispersed in cyclohexane and water, respectively. UCLNPs exhibit a diameter of 22.7 ± 0.7 nm. These data were measured by Dipl. Phys. Martin Kaiser at the Federal Institute for Materials Research and Testing, BAM, Berlin, Germany, with a custom-designed integrating sphere setup.*

6.3.   Future Directions and Perspectives

During the last three years remarkable efforts have been reported in order to shift the excitation wavelength of UCLNPs from 980 nm to a more suitable wavelength for biological applications [300]. In 2011, Zhan *et al.* used 915 nm-excited UCLNPs for *in vitro* and *in vivo* bioimaging. They took advantage of the relatively broad absorption band of Yb^{3+} sensitizer ions which is located in the range of ~ 900 nm to ~ 1000 nm. However, this approach suffers from a compromised luminescence efficiency due to a lower absorption of Yb^{3+} around 915 nm [293]. In 2012, Zou *et al.* reported on NIR dye-sensitized UCLNPs. In their concept,

light (740 to 850 nm) is absorbed by surface-bound NIR dyes acting as antennas for light harvesting and then transferred to the UCLNP core (doped with Yb^{3+}/Er^{3+}) *via* Förster Resonance Energy Transfer (FRET) mechanism to produce upconversion luminescence. Drawbacks of this conception are, that organic dyes are prone to photobleaching, and dye molecules may leach from the UCLNP surface since they are only electrostatically attached [282].

Shen *et al.* published a different approach in 2013. Nd^{3+} was employed as a new primary sensitizer capable of absorbing 800 nm radiation. The excitation energy is transferred from Nd^{3+} to Er^{3+} (or Tm^{3+}) activator ions by using Yb^{3+} ions as "bridging" sensitizers (see Scheme 8). These cascade-sensitized UCLNPs display visible upconversion luminescence upon 800 nm excitation [301]. Recently, similar approaches have been published by different research groups [302,303,304,305,306].
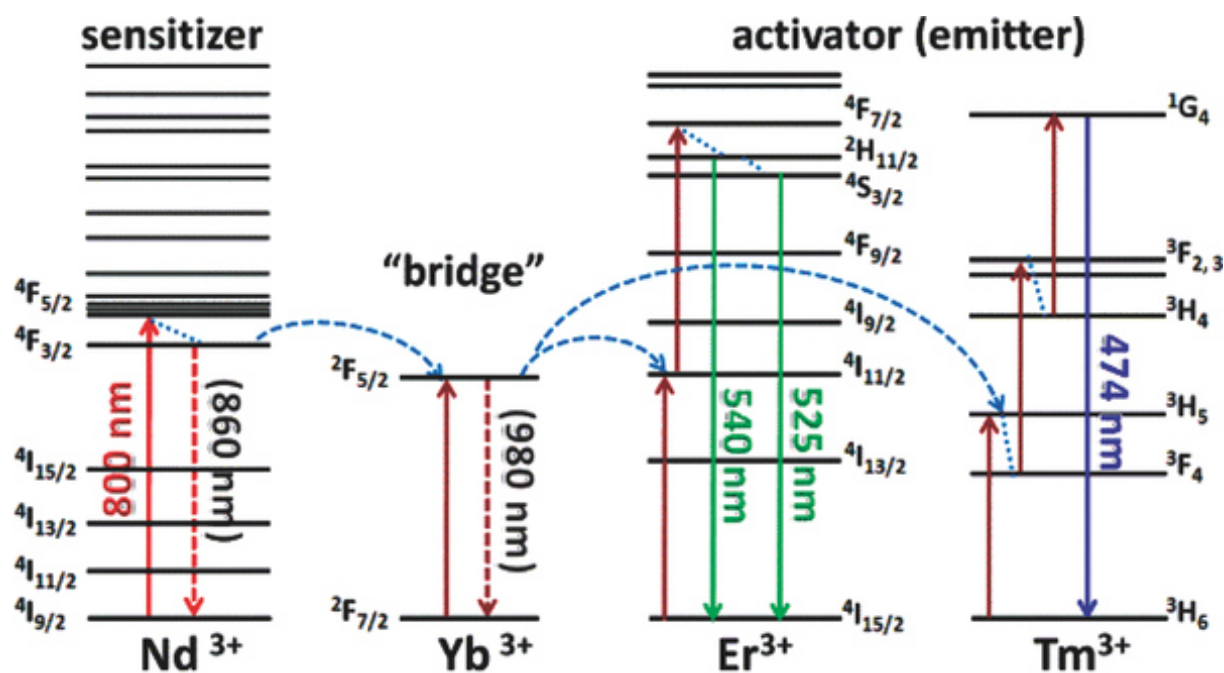
Scheme 8 | Upconversion process of $Nd^{3+} \rightarrow Yb^{3+} \rightarrow Er^{3+}$ (Tm^{3+}) tri-doped UCLNPs upon 800 nm excitation. Reprinted with permission from ref. [301]. Copyright 2013, Wiley-VCH Verlag GmbH & Co. KGaA, Weinheim.

This concept is highly promising since local overheating can be greatly reduced by using 800 nm rather than 980 nm excitation light simultaneously increasing the

penetration depth into biological tissue. However, the preparation of such Nd^{3+},Yb^{3+},Er^{3+} (or Tm^{3+})-tridoped UCLNPs is a nontrivial task. Deleterious energy transfer processes from Er^{3+} (or Tm^{3+}) activator ions to Nd^{3+} *via* cross-relaxations can occur, when all these ions are embedded in the same matrix. Therefore, Nd^{3+} ions and activator ions must be spatially separated from one another. The design of core-shell architectures allows for such a separation. Though, the controlled synthesis and characterization of core-shell UCLNPs with defined compositions of the core and the shell is very challenging. Nevertheless, Nd^{3+}-sensitized UCLNPs hold great potential of being the next generation of upconverting nanomaterials. The shift in the excitation wavelength from 980 nm to 800 nm, where water absorbs minimally, is an important improvement. The utilization of Nd^{3+}-doped UCLNPs may advance their future (bio)-analytical applications and theranostic capabilities.

Another challenge is the impossibility to excite upconversion luminescence of UCLNPs by commercially available instrumentation. Typically, the excitation power density achieved by lamps is not sufficiently strong to induce the upconversion processes. Thus, laser diodes with an emission wavelength of ~ 980 nm (or ~ 800 nm in case of Nd^{3+}-doped UCLNPs) are required. This lack of commercial instrumentation limits the utilization of UCLNPs to only a small community of research groups which have custom-built or custom-modified instruments available. An additional issue of this circumstance is that in most cases no information of the excitation power density applied for such custom-built instruments is reported. Since upconversion luminescence properties strongly depend on the excitation power density, no reliable quantitative comparison of results obtained by different research groups on different instruments is possible.

In order to fully exploit the potential of UCLNPs these challenges have to be addressed. Most importantly, an absolute value of the efficiency of UCLNPs needs to be provided, which allows for a direct comparison of results obtained by different groups. Furthermore, it is expected that the development of UCLNPs for imaging and sensing applications strongly benefits from the shift of the excitation wavelength from 980 nm to 800 nm, where the absorption of water is greatly reduced.

7.   Summary

The thesis describes the synthesis, characterization, surface modification, and (bio)-analytical applications of upconverting luminescent nanoparticles (UCLNPs). In Chapter 1 an overview of nanomaterials used for (bio)-analytical sensing and imaging is provided with special emphasis on luminescent nanomaterials. UCLNPs as one class of luminescent nanomaterials are introduced. The aims of this work such as synthesis of small UCLNPs with a narrow size-distribution, their surface engineering, and a study on their luminescence properties are addressed in Chapter 2.

Chapter 3 deals with surface-functionalized multicolor UCLNPs suitable for protein conjugation. The preparation and characterization of monodisperse silica-coated UCLNPs (average diameter of 38 nm) modified with poly(ethylene glycol) spacers carrying N-hydroxysuccinimde groups is presented. It is demonstrated that such UCLNPs can be employed as luminescent labels due to their strong binding to proteins. A hybrid material consisting of streptavidinylated magnetic beads labeled with amino-reactive UCLNPs is prepared which can be separated from a colloidal dispersion by applying an external magnetic force. These magnetic beads/UCLNPs conjugates display visible upconversion luminescence upon 980 nm continuous wave laser excitation.

The synthesis of amphiphilic polymer-coated core-shell UCLNPs is reported in Chapter 4. Using such a core-shell architecture, the upconversion luminescence intensity at 475 nm is increased by a factor of ~ 60. It is demonstrated that the upconversion emission of core-shell UCLNPs based on β-NaYF$_4$(Yb^{3+}/Tm^{3+})@NaYF$_4$ spectrally matches the absorption of the coenzyme FAD and the enzyme cosubstrate NADH. This spectral match is exploited to fluorescently monitor the formation of NADH and the consumption of FAD during enzymatic reactions using 980 nm photoexcitation. A sensing scheme based on an inner filter effect employing UCLNPs as a kind of nanolamps is developed which allows for the quantification of ethanol and glucose levels.

In Chapter 5 an optimized synthesis protocol for the large scale production of oleate-capped UCLNPs based on β-NaYF$_4$(Yb^{3+}/Er^{3+}) is described. Such UCLNPs are

characterized by a high crystallinity, an extremely narrow size distribution, and a comparatively high quantum yield. The impact of nine different surface modifications, which allow for a phase transfer of initially hydrophobic UCLNPs into water, on their upconversion luminescence properties is described.

Limitations and challenges of UCLNPs are addressed in Chapter 6. Their future directions and perspectives are highlighted.

8.   Zusammenfassung

Die vorliegende Arbeit beschreibt die Synthese, die Charakterisierung, die Oberflächen-modifizierung und die bioanalytischen Anwendungen von lumineszierenden Nanopartikeln mit der Fähigkeit zur Aufwärtskonvertierung (UCLNPs). Das erste Kapitel gibt einen Überblick über verschiedene Nanomaterialien und deren Einsatz in der bioanalytischen Sensorik und Bildgebung, wobei ein besonderes Augenmerk auf lumineszierende Nanomaterialien gelegt wird. Darüber hinaus werden UCLNPs, die als eine besondere Klasse von lumineszierenden Nanomaterialien angesehen werden können, vorgestellt und beschrieben. Im zweiten Kapitel wird die Motivation für die Forschung an diesem Thema dargelegt, und es werden die Ziele dieser Arbeit abgesteckt.

Das dritte Kapitel befasst sich mit UCLNPs, die an Proteine gebunden werden können und Lumineszenz mit mehreren diskreten Emissionsbanden aufweisen. Die Synthese und Charakterisierung von monodispersen UCLNPs, die mit einer Silikatschicht umhüllt sind, wird gezeigt. Dabei beträgt der Partikeldurchmesser 38 nm. Weiterhin sind diese Partikel mit Polyethylenglycol Molekülen modifiziert, die kovalent mit N-hydroxysuccinimid Gruppen verknüpft sind. Es wird gezeigt, dass diese Art von UCLNPs als lumineszierende Marker verwendet werden können, die eine starke Bindungsaffinität zu Proteinen aufweisen. Die Herstellung eins Hybridmaterials, welches aus mit Streptavidin modifizierten magnetischen Partikeln und mit Aminogruppen modifizierten UCLNPs aufgebaut ist, wird beschrieben. Dieses Hybridmaterial kann mit Hilfe eines externen Permanentmagneten aus einer kolloidalen Dispersion abgetrennt werden. Weiterhin zeigt dieses Material sichtbare aufwärtskonvertierte Lumineszenz bei Anregung durch einen 980 nm Dauerstrichlaser.

Die Synthese von Kern-Hülle UCLNPs, die mit einem amphiphilen Polymer umhüllt sind, wird in Kapitel 4 vorgestellt. Mit Hilfe einer solchen Kern-Hülle Architektur ist es möglich, die Intensität der aufwärtskonvertierten Lumineszenz bei einer Emissionswellenlänge von 475 nm um einen Faktor von 60 zu erhöhen. Die Emissionen von Kern-Hülle UCLNPs der Zusammensetzung β-NaYF$_4$(Yb^{3+}/Tm^{3+})@NaYF$_4$ weisen einen spektralen Überlapp mit der Absorption des Coenzyms FAD und des Cosubstrates NADH auf. Dieser spektrale Überlapp wird dahingehend ausgenutzt, die Bildung von NADH und den

Verbrauch von FAD während enzymatischer Reaktionen fluoreszenzbasiert zu verfolgen. Dies geschieht unter Anregung mit Licht einer Wellenlänge von 980 nm. Aufbauend auf diesen Ergebnissen wird die Entwicklung eines Sensorkonzepts das auf einem inneren Filtereffekt beruht, dargestellt. Damit ist es möglich, quantitativ Ethanol und Glucose zu bestimmen. Die Kern-Hülle UCLNPs werden dabei als sogenannte „Nanolampen" eingesetzt.

Im fünften Kapitel wird ein optimiertes Syntheseprotokoll vorgestellt, mit dem es möglich ist, UCLNPs der Zusammensetzung β-NaYF$_4$(Yb^{3+}/Er^{3+}), die ihrerseits mit Oleat Ionen umhüllt sind, im Großmaßstab herzustellen. Die dabei produzierten UCLNPs zeichnen sich durch ihre hohe Kristallinität und ihre sehr enge Größenverteilung aus. Des Weiteren besitzen sie eine vergleichsweise hohe Quantenausbeute. In einer Studie wird der Einfluss von neun verschiedenen Oberflächenmodifikationen bezüglich der Lumineszenzeigenschaften von UCLNPs untersucht. Mit Hilfe dieser Oberflächenmodifikationen wird der Phasentransfer von hydrophoben UCLNPs in wässrige Medien gewährleistet.

Die Einschränkungen und Herausforderungen im Zusammenhang mit UCLNPs werden im sechsten Kapitel aufgelistet. Ein Ausblick über zukünftige Trends zur Verwendung von UCLNPs in der bioanalytischen Bildgebung und Sensorik wird eröffnet.

9.   Curriculum Vitae

Vorname, NAME	Stefan WILHELM
Adresse	Pischdorf 14
	92543 Guteneck
Geboren am	21.04.1981

Akademische Ausbildung

07/2010 - 06/2014	Doktorarbeit in Chemie
	Universität Regensburg; Institut für Analytische Chemie, Chemo- und Biosensorik; Arbeitsgruppe von Prof. Otto S. Wolfbeis
08/2009 - 04/2010	Diplomarbeit in Chemie
	Universität Regensburg; Institut für Analytische Chemie, Chemo- und Biosensorik; Arbeitsgruppe von Prof. Otto S. Wolfbeis
	Thema:"*Irreversibler optischer Nachweis von Sauerstoff; Anwendung in der Analytik und Zeitmessung*"
10/2002 - 09/2008	Diplomstudium der Chemie an der Universität Regensburg
	Hauptfach: Analytische Chemie
	Nebenfächer: Organische Chemie, Anorganische Chemie

Schulische Ausbildung

08/2008 - 07/2010	Berufsfachschule für Musik in Nürnberg
	Hauptfach: Rock/Pop/Jazz – Drumset
09/1992 - 07/2001	Johann-Andreas-Schmeller Gymnasium in Nabburg

Wehrdienst

09/2001 - 09/2002	Sanitätssoldat am Bundeswehrkrankenhaus in Amberg

Auszeichnungen

2012	Posterpreis, EUROPT(R)ODE XI, Barcelona, Spanien
2011	European Materials Research Society (E-MRS) Travel Award, Nizza, Frankreich

10. Publications

11. V. Muhr, **S. Wilhelm**, T. Hirsch, O. S. Wolfbeis. Phase Transfer of Colloidal Upconverting Nanoparticles: From Nonpolar Solvents to Aqueous Media. *Submitted.*

10. **S. Wilhelm**, M. Kaiser, C. Würth, J. Heiland, C. C. Carrion, V. Muhr, O. S. Wolfbeis, W. J. Parak, U. Resch-Genger, T. Hirsch. Impact of Surface Modification on the Luminescence and Colloidal Properties of Water Dispersible Upconverting Nanoparticles. *Submitted.*

9. E. Scheucher, **S. Wilhelm**, T. Hirsch, T. Mayr. Magnetic Luminescent Oxygen Sensor Particles Excited with Internal Upconversion Nanolamps. *In preparation.*

8. **S. Wilhelm**, M. del Barrio, J. Heiland, S. F. Himmelstoß, J. Galban, O. S. Wolfbeis, T. Hirsch. Spectrally Matched Upconverting Luminescent Nanoparticles for Monitoring Enzymatic Reactions. *Submitted.*

7. M. del Barrio, S. de Marcos, V. Cebolla, J. Heiland, **S. Wilhelm**, T. Hirsch, J. Galban. Enzyme-induced Modulation of the Emission of Upconverting Nanoparticles: Towards a New Sensing Scheme for Glucose. *Biosensors and Bioelectronics* 2014, 59, 14-20.

6. C. Röhrer, M. Dollinger, **S. Wilhelm**, T. Hirsch, O. S. Wolfbeis, C. Fellner, C. Stroszczynski, P. Wiggermann. Gd^{3+} dotierte lumineszierende Nanokristalle als Kontrastmittel in der MRT. *RöFo - Fortschritte auf dem Gebiet der Röntgenstrahlen und der bildgebenden Verfahren* 2013, 185, VO309_5.

5. **S. Wilhelm**, T. Hirsch, W.M. Patterson, E. Scheucher, T. Mayr, O. S. Wolfbeis. Protein-reactive Multicolor Upconversion Nanoparticles. *Theranostics* 2013, 3, 239-248.

4. C. Fenzl, **S. Wilhelm**, T. Hirsch, O.S. Wolfbeis. Optical Sensing of the Ionic Strength Using Photonic Crystals in a Hydrogel Matrix. *ACS Applied Materials & Interfaces* 2013, 5, 173–178.

3.   **S. Wilhelm**, T. Hirsch, E. Scheucher, T. Mayr, O. S. Wolfbeis. Magnetic Nanosensor Particles with Luminescence Upconversion Capability. *Angewandte Chemie Intational Edition* 2011, 50 (37), A59-A62.
Angewandte Chemie German Edition 2011, 123 (37), A59-A62.

2.   **S. Wilhelm**, O. S. Wolfbeis. Irreversible Sensing of Oxygen Ingress. *Sensors and Actuators B*: Chemical 2011, 153, 199-204.

1.   **S. Wilhelm**, O. S. Wolfbeis. Opto-Chemical Micro-Capillary Clocks. *Microchimica Acta* 2010, 171, 211-216.

11. Presentations

Oral Presentations

2013 **Materials Research Society (MRS) Spring Meeting**, San Francisco, USA
Upconverting luminescent nanoparticles based on lanthanide-doped $NaYF_4$: surface engineering for (bio)-analytical applications

2012 **Chebana, UpCore Meeting**, Regensburg, Germany
Protein-reactive upconverting luminescent nanoparticles (UCLNPs)

2011 **7th Int. Students Conference "Modern Analytical Chemistry"**, Prague, Czech Republic
Magnetic and upconverting luminescent core-shell nanoparticles for sensor applications

2011 **European Materials Research Society (E-MRS) Spring Meeting**, Nice, France
$Fe_3O_4@NaYF_4(Yb/Er)$ core-shell nanoparticles for sensor applications

Poster Presentations

2013 **8th German Biosensor Symposium**, Wildau, Germany
Silica-coated multicolor upconverting luminescent nanoparticles for protein conjugation

2012 **EUROPT(R)ODE XI**, Barcelona, Spain
Magnetic core-shell rare earth-doped nanoparticles with tunable upconversion luminescence for sensor applications

2011 **European Materials Research Society (E-MRS) Spring Meeting**, Nice, France
$Fe_3O_4@NaYF_4(Yb/Er)$ core-shell nanoparticles for sensor applications

2011 **ANAKON**, Zurich, Switzerland
Leuco dyes for irreversible sensing of oxygen ingress and optical timing

12.   References

1 Yin, Y. & Alivisatos, A. P. Colloidal nanocrystal synthesis and the organic–inorganic interface. *Nature* **437,** 664–670 (2005).

2 Williams, D. B. & Carter, C. B. *Transmission Electron Microscopy: A Textbook for Materials Science*. (Springer, 2009).

3 Hutchings, J. Engineering and science, Volume 23:5, February 1960. *Engineering and Science* (1960).

4 Lu, Y., Wang, L., Chen, D. & Wang, G. Determination of the concentration and the average number of gold atoms in a gold nanoparticle by osmotic pressure. *Langmuir* **28,** 9282–9287 (2012).

5 Ackerson, C. J., Jadzinsky, P. D., Sexton, J. Z., Bushnell, D. A. & Kornberg, R. D. Synthesis and bioconjugation of 2 and 3 nm-diameter gold nanoparticles. *Bioconjugate Chemistry* **21,** 214–218 (2010).

6 Cao, A., Lu, R. & Veser, G. Stabilizing metal nanoparticles for heterogeneous catalysis. *Physical Chemistry Chemical Physics* **12,** 13499 (2010).

7 Mattoussi, H., Palui, G. & Na, H. B. Luminescent quantum dots as platforms for probing in vitro and in vivo biological processes. *Advanced Drug Delivery Reviews* **64,** 138–166 (2012).

8 Bond, G. C. & Thompson, D. T. Catalysis by gold. *Catalysis Reviews* **41,** 319–388 (1999).

9 Grabow, L. C. & Mavrikakis, M. Nanocatalysis Beyond the gold-rush era. *Angewandte Chemie International Edition* **47,** 7390–7392 (2008).

10 Bell, A. T. The impact of nanoscience on heterogeneous catalysis. *Science* **299,** 1688–1691 (2003).

11 Wagner, F. E. *et al.* Before striking gold in gold-ruby glass. *Nature* **407,** 691–692 (2000).

12 Barber, D. J. & Freestone, I. C. An investigation of the origin of the colour of the lycurgus cup by analytical transmission electron microscopy. *Archaeometry* **32,** 33–45 (1990).

13 Faraday, M. The bakerian lecture: experimental relations of gold (and other metals) to light. *Philosophical Transactions of the Royal Society London* **147,** 145–181 (1857).

14 Graham, T. Liquid diffusion applied to analysis. *Philosophical Transactions of the Royal Society London* **151,** 183–224 (1861).

15 Murphy, C. J. *et al.* Gold nanoparticles in biology: beyond toxicity to cellular imaging. *Accounts of Chemical Research.* **41,** 1721–1730 (2008).

16 El-Sayed, M. A. Some interesting properties of metals confined in time and nanometer space of different shapes. *Accounts of Chemical Research* **34,** 257–264 (2001).

17 Mie, G. Beiträge zur optik trueber medien, speziell kolloidaler metallösungen. *Annalen der Physik* **330,** 377–445 (1908).

18 Page Faulk, W. & Malcolm Taylor, G. Communication to the editors: An immunocolloid method for the electron microscope. *Immunochemistry* **8,** 1081–1083 (1971).

19 Plas, F. E. M. P. van de & Leunissen, J. L. M. in *Nonradioactive Analysis of Biomolecules* (Kessler, P.-D. D. C.) 193–205 (Springer Berlin Heidelberg, 2000).

20 Daniel, M.-C. & Astruc, D. Gold nanoparticles: assembly, supramolecular chemistry, quantum-size-related properties, and applications toward biology, catalysis, and nanotechnology. *Chemical Reviews* **104,** 293–346 (2004).

21 Bunz, U. H. F. & Rotello, V. M. Gold nanoparticle–fluorophore complexes: sensitive and discerning 'noses' for biosystems sensing. *Angewandte Chemie International Edition* **49,** 3268–3279 (2010).

22 Llevot, A. & Astruc, D. Applications of vectorized gold nanoparticles to the diagnosis and therapy of cancer. *Chemical Society Reviews* **41,** 242–257 (2011).

23 Dreaden, E. C., Alkilany, A. M., Huang, X., Murphy, C. J. & El-Sayed, M. A. The golden age: gold nanoparticles for biomedicine. *Chemical Society Reviews* **41,** 2740–2779 (2012).

24 Eustis, S. & El-Sayed, M. A. Why gold nanoparticles are more precious than pretty gold: Noble metal surface plasmon resonance and its enhancement of the radiative and nonradiative properties of nanocrystals of different shapes. *Chemical Society Reviews* **35,** 209 (2006).

25 Stratakis, M. & Garcia, H. Catalysis by supported gold nanoparticles: beyond aerobic oxidative processes. *Chemical Reviews* **112,** 4469–4506 (2012).

26 Homola, J. Surface plasmon resonance sensors for detection of chemical and biological species. *Chemical Reviews* **108,** 462–493 (2008).

27 Abramczyk, H. & Brozek-Pluska, B. Raman imaging in biochemical and biomedical applications. Diagnosis and treatment of breast cancer. *Chemical Reviews* **113,** 5766–5781 (2013).

28 Qian, X.-M. & Nie, S. M. Single-molecule and single-nanoparticle SERS: from fundamental mechanisms to biomedical applications. *Chemical Society Reviews* **37,** 912 (2008).

29 Saha, K., Agasti, S. S., Kim, C., Li, X. & Rotello, V. M. Gold nanoparticles in chemical and biological sensing. *Chemical Reviews* **112,** 2739–2779 (2012).

30 Dykman, L. & Khlebtsov, N. Gold nanoparticles in biomedical applications: recent advances and perspectives. *Chemical Society Reviews* **41,** 2256 (2012).

31 Dubertret, B., Calame, M. & Libchaber, A. J. Single-mismatch detection using gold-quenched fluorescent oligonucleotides. *Nature Biotechnology* **19,** 365–370 (2001).

32 Reddy, L. H., Arias, J. L., Nicolas, J. & Couvreur, P. Magnetic nanoparticles: design and characterization, toxicity and biocompatibility, pharmaceutical and biomedical applications. *Chemical Reviews* **112,** 5818–5878 (2012).

33 Hao, R. *et al.* Synthesis, functionalization, and biomedical applications of multifunctional magnetic nanoparticles. *Advanced Materials* **22,** 2729–2742 (2010).

34 Pan, Y., Du, X., Zhao, F. & Xu, B. Magnetic nanoparticles for the manipulation of proteins and cells. *Chemical Society Reviews* **41,** 2912–2942 (2012).

35 Yoo, D., Lee, J.-H., Shin, T.-H. & Cheon, J. Theranostic magnetic nanoparticles. *Accounts of Chemical Research* **44,** 863–874 (2011).

36 Chomoucka, J. *et al.* Magnetic nanoparticles and targeted drug delivering. *Pharmacological Research* **62,** 144–149 (2010).

37 Kumar, C. S. S. R. & Mohammad, F. Magnetic nanomaterials for hyperthermia-based therapy and controlled drug delivery. *Advanced Drug Delivery Reviews* **63,** 789–808 (2011).

38 Jung, J. H., Lee, J. H. & Shinkai, S. Functionalized magnetic nanoparticles as chemosensors and adsorbents for toxic metal ions in environmental and biological fields. *Chemical Society Reviews* **40,** 4464–4474 (2011).

39 Xie, J., Liu, G., Eden, H. S., Ai, H. & Chen, X. Surface-engineered magnetic nanoparticle platforms for cancer imaging and therapy. *Accounts of Chemical Research.* **44,** 883–892 (2011).

40 Colombo, M. *et al.* Biological applications of magnetic nanoparticles. *Chemical Society Reviews* **41,** 4306–4334 (2012).

41 Lee, N. & Hyeon, T. Designed synthesis of uniformly sized iron oxide nanoparticles for efficient magnetic resonance imaging contrast agents. *Chemical Society Reviews* **41,** 2575–2589 (2012).

42 Sieber, M. A., Steger-Hartmann, T., Lengsfeld, P. & Pietsch, H. Gadolinium-based contrast agents and NSF: Evidence from animal experience. *Journal of Magnetic Resonance Imaging* **30,** 1268–1276 (2009).

43 Simonsen, C. Z. *et al.* CBF and CBV measurements by USPIO bolus tracking: Reproducibility and comparison with Gd-based values. *Journal of Magnetic Resonance Imaging* **9,** 342–347 (1999).

44 Yallapu, M. M. *et al.* Multi-functional magnetic nanoparticles for magnetic resonance imaging and cancer therapy. *Biomaterials* **32,** 1890–1905 (2011).

45 Edwards, K. A., Bolduc, O. R. & Baeumner, A. J. Miniaturized bioanalytical systems: enhanced performance through liposomes. *Current Opinion in Chemical Biology* **16,** 444–452 (2012).

46 Allen, T. M. & Cullis, P. R. Liposomal drug delivery systems: From concept to clinical applications. *Advanced Drug Delivery Reviews* **65,** 36–48 (2013).

47 Wang, A. Z., Langer, R. & Farokhzad, O. C. Nanoparticle delivery of cancer drugs. *Annual Review of Medicine* **63,** 185–198 (2012).

48 Edwards, K. A. & Baeumner, A. J. Liposomes in analyses. *Talanta* **68,** 1421–1431 (2006).

49 Liu, Q. & Boyd, B. J. Liposomes in biosensors. *The Analyst* **138,** 391 (2013).

50 Yu, H. *et al.* Dumbbell-like bifunctional Au−Fe₃O₄ nanoparticles. *Nano Letters* **5,** 379–382 (2005).

51 Selvan, S. T., Tan, T. T. Y., Yi, D. K. & Jana, N. R. Functional and multifunctional nanoparticles for bioimaging and biosensing. *Langmuir* **26,** 11631–11641 (2010).

52 Resch-Genger, U., Grabolle, M., Cavaliere-Jaricot, S., Nitschke, R. & Nann, T. Quantum dots versus organic dyes as fluorescent labels. *Nature Methods* **5,** 763–775 (2008).

53 Wang, F., Tan, W. B., Zhang, Y., Fan, X. & Wang, M. Luminescent nanomaterials for biological labelling. *Nanotechnology* **17,** R1 (2006).

54 Wang, R. & Zhang, F. NIR luminescent nanomaterials for biomedical imaging. *Journal of Materials Chemistry B* **2,** 2422–2443 (2014).

55 Petryayeva, E., Algar, W. R. & Medintz, I. L. Quantum dots in bioanalysis: A review of applications across various platforms for fluorescence spectroscopy and imaging. *Applied Spectroscopy* **67,** 215–252 (2013).

56 Feldmann, C. Luminescent nanomaterials. *Nanoscale* **3,** 1947–1948 (2011).

57 Lakowicz, J. R. Principles of fluorescence spectroscopy (Lakowicz, J. R.) 1–26, *Springer US*, (2006).

58 Zhao, X., Bagwe, R. P. & Tan, W. Development of organic-dye-doped silica nanoparticles in a reverse microemulsion. *Advanced Materials* **16,** 173–176 (2004).

59 Klapper, M., Nenov, S., Haschick, R., Müller, K. & Müllen, K. Oil-in-oil emulsions: A unique tool for the formation of polymer nanoparticles. *Accounts of Chemical Research* **41,** 1190–1201 (2008).

60 Bae, S. W., Tan, W. & Hong, J.-I. Fluorescent dye-doped silica nanoparticles: new tools for bioapplications. *Chemical Communications* **48,** 2270–2282 (2012).

61 Zanarini, S. *et al.* Ru(bpy)₃ covalently doped silica nanoparticles as multicenter tunable structures for electrochemiluminescence amplification. *Journal of the American Chemical Society* **131,** 2260–2267 (2009).

62 Li, Z., Barnes, J. C., Bosoy, A., Stoddart, J. F. & Zink, J. I. Mesoporous silica nanoparticles in biomedical applications. *Chemical Society Reviews* **41,** 2590–2605 (2012).

63 Genovese, D. *et al.* Energy transfer processes in dye-doped nanostructures yield cooperative and versatile fluorescent probes. *Nanoscale* **6,** 3022–3036 (2014).

64 Bagwe, R. P., Yang, C., Hilliard, L. R. & Tan, W. Optimization of dye-doped silica nanoparticles prepared using a reverse microemulsion method. *Langmuir* **20,** 8336–8342 (2004).

65 Ganguli, A. K., Ganguly, A. & Vaidya, S. Microemulsion-based synthesis of nanocrystalline materials. *Chemical Society Reviews* **39,** 474 (2010).

66 Rao, J. P. & Geckeler, K. E. Polymer nanoparticles: Preparation techniques and size-control parameters. *Progress in Polymer Science* **36,** 887–913 (2011).

67 He, Q. & Shi, J. Mesoporous silica nanoparticle based nano drug delivery systems: synthesis, controlled drug release and delivery, pharmacokinetics and biocompatibility. *Journal of Materials Chemistry* **21,** 5845–5855 (2011).

68 Peng, F. *et al.* Silicon nanomaterials platform for bioimaging, biosensing, and cancer therapy. *Accounts of Chemical Research* **47,** 612–623 (2014).

69 Tang, F., Li, L. & Chen, D. Mesoporous silica nanoparticles: synthesis, biocompatibility and drug delivery. *Advanced Materials* **24,** 1504–1534 (2012).

70 Lee, J. E., Lee, N., Kim, T., Kim, J. & Hyeon, T. Multifunctional mesoporous silica nanocomposite nanoparticles for theranostic applications. *Accounts of Chemical Research* **44,** 893–902 (2011).

71 Mochalin, V. N., Shenderova, O., Ho, D. & Gogotsi, Y. The properties and applications of nanodiamonds. *Nature Nanotechnology* **7,** 11–23 (2012).

72 Baker, S. N. & Baker, G. A. Luminescent carbon nanodots: emergent nanolights. *Angewandte Chemie International Edition* **49,** 6726–6744 (2010).

73 Loh, K. P., Bao, Q., Eda, G. & Chhowalla, M. Graphene oxide as a chemically tunable platform for optical applications. *Nature Chemistry* **2,** 1015–1024 (2010).

74 Wu, H.-C., Chang, X., Liu, L., Zhao, F. & Zhao, Y. Chemistry of carbon nanotubes in biomedical applications. *Journal of Materials Chemistry* **20,** 1036–1052 (2010).

75 Shiang, Y.-C., Huang, C.-C., Chen, W.-Y., Chen, P.-C. & Chang, H.-T. Fluorescent gold and silver nanoclusters for the analysis of biopolymers and cell imaging. *Journal of Materials Chemistry* **22,** 12972–12982 (2012).

76 Zhu, Y. *et al.* The biocompatibility of nanodiamonds and their application in drug Delivery systems. *Theranostics* **2,** 302–312 (2012).

77 Krueger, A. Diamond nanoparticles: jewels for chemistry and physics. *Advanced Materials* **20,** 2445–2449 (2008).

78 Chang, Y.-R. *et al.* Mass production and dynamic imaging of fluorescent nanodiamonds. *Nature Nanotechnology* **3,** 284–288 (2008).

79 Williams, O. A. *et al.* Growth, electronic properties and applications of nanodiamond. *Diamond and Related Materials* **17,** 1080–1088 (2008).

80 Li, H., Kang, Z., Liu, Y. & Lee, S.-T. Carbon nanodots: synthesis, properties and applications. *Journal of Materials Chemisty* **22,** 24230–24253 (2012).

81 Kochmann, S., Hirsch, T. & Wolfbeis, O. S. Graphenes in chemical sensors and biosensors. *TrAC Trends in Analytical Chemistry* **39,** 87–113 (2012).

82 Chen, D., Feng, H. & Li, J. Graphene oxide: preparation, functionalization, and electrochemical applications. *Chemical Reviews* **112,** 6027–6053 (2012).

83 Jariwala, D., Sangwan, V. K., Lauhon, L. J., Marks, T. J. & Hersam, M. C. Carbon nanomaterials for electronics, optoelectronics, photovoltaics, and sensing. *Chemical Society Reviews* **42,** 2824–2860 (2013).

84 Shang, L., Dong, S. & Nienhaus, G. U. Ultra-small fluorescent metal nanoclusters: Synthesis and biological applications. *Nano Today* **6,** 401–418 (2011).

85 Lu, Y. & Chen, W. Sub-nanometre sized metal clusters: from synthetic challenges to the unique property discoveries. *Chemical Society Reviews* **41,** 3594–3623 (2012).

86 Alivisatos, A. P. Semiconductor clusters, nanocrystals, and quantum dots. *Science* **271,** 933–937 (1996).

87 El-Sayed, M. A. Small is different: shape-, size-, and composition-dependent properties of some colloidal semiconductor nanocrystals. *Accounts of Chemical Research* **37,** 326–333 (2004).

88 Smith, A. M. & Nie, S. Semiconductor nanocrystals: structure, properties, and band gap engineering. *Accounts of Chemical Research* **43,** 190–200 (2010).

89 Gao, X., Cui, Y., Levenson, R. M., Chung, L. W. K. & Nie, S. In vivo cancer targeting and imaging with semiconductor quantum dots. *Nature Biotechnology* **22,** 969–976 (2004).

90 Medintz, I. L., Uyeda, H. T., Goldman, E. R. & Mattoussi, H. Quantum dot bioconjugates for imaging, labelling and sensing. *Nature Materials* **4,** 435–446 (2005).

91 Dubertret, B. *et al.* In vivo imaging of quantum dots encapsulated in phospholipid micelles. *Science* **298,** 1759–1762 (2002).

92 Derfus, A. M., Chan, W. C. W. & Bhatia, S. N. Intracellular delivery of quantum dots for live cell labeling and organelle tracking. *Advanced Materials* **16,** 961–966 (2004).

93 Otsuka, H., Nagasaki, Y. & Kataoka, K. PEGylated nanoparticles for biological and pharmaceutical applications. *Advanced Drug Delivery Reviews* **64,** 46–255 (2012).

94 Kairdolf, B. A. *et al.* Semiconductor quantum dots for bioimaging and biodiagnostic applications. *Annual Review of Analytical Chemistry* **6,** 143–162 (2013).

95 Michalet, X. *et al.* Quantum dots for live cells, in vivo imaging, and diagnostics. *Science* **307,** 538–544 (2005).

96 Vossmeyer, T. *et al.* CdS nanoclusters: synthesis, characterization, size dependent oscillator strength, temperature shift of the excitonic transition energy, and reversible absorbance shift. *Journal of Physical Chemistry.* **98,** 7665–7673 (1994).

97 Chan, W. C. *et al.* Luminescent quantum dots for multiplexed biological detection and imaging. *Current Opinion in Biotechnology* **13,** 40–46 (2002).

98 Dabbousi, B. O. *et al.* (CdSe)ZnS core−shell quantum dots: synthesis and characterization of a size series of highly luminescent nanocrystallites. *Journal of Physical Chemisty B* **101,** 9463–9475 (1997).

99 Murray, C. B., Norris, D. J. & Bawendi, M. G. Synthesis and characterization of nearly monodisperse CdE (E = sulfur, selenium, tellurium) semiconductor nanocrystallites. *Journal of the American Chemical Society* **115,** 8706–8715 (1993).

100 Yu, W. W., Qu, L., Guo, W. & Peng, X. Experimental determination of the extinction coefficient of CdTe, CdSe, and CdS nanocrystals. *Chemistry of Materials.* **15,** 2854–2860 (2003).

101 Kuçur, E., Boldt, F. M., Cavaliere-Jaricot, S., Ziegler, J. & Nann, T. Quantitative analysis of cadmium selenide nanocrystal concentration by comparative techniques. *Analytical Chemisty* **79,** 8987–8993 (2007).

102 Chan, W. C. W. & Nie, S. Quantum dot bioconjugates for ultrasensitive nonisotopic detection. *Science* **281,** 2016–2018 (1998).

103 Wang, X., Qu, L., Zhang, J., Peng, X. & Xiao, M. Surface-related emission in highly luminescent CdSe quantum dots. *Nano Letters* **3,** 1103–1106 (2003).

104 Qu, L. & Peng, X. Control of photoluminescence properties of CdSe nanocrystals in growth. *Journal of the American Chemical Society* **124,** 2049–2055 (2002).

105 Seybold, P. G., Gouterman, M. & Callis, J. Calorimetric, photometric and lifetime determinations of fluorescence yields of fluorescein dyes. *Photochemistry and Photobiology* **9,** 229–242 (1969).

106 Soper, S. A. & Mattingly, Q. L. Steady-state and picosecond laser fluorescence studies of nonradiative pathways in tricarbocyanine dyes: implications to the design of near-IR fluorochromes with high fluorescence efficiencies. *Journal of the American Chemical Society* **116,** 3744–3752 (1994).

107 Efros, A. L. & Rosen, M. The electronic structure of semiconductor nanocrystals. *Annual Review of Materials Science* **30,** 475–521 (2000).

108 Dahan, M. *et al.* Time-gated biological imaging by use of colloidal quantum dots. *Optics Letters* **26,** 825–827 (2001).

109 Larson, D. R. *et al.* Water-soluble quantum dots for multiphoton fluorescence imaging in vivo. *Science* **300,** 1434–1436 (2003).

110 Clapp, A. R. *et al.* Two-photon excitation of quantum-dot-based fluorescence resonance energy transfer and its applications. *Advanced Materials* **19,** 1921–1926 (2007).

111 Schlegel, G., Bohnenberger, J., Potapova, I. & Mews, A. Fluorescence decay time of single semiconductor nanocrystals. *Physical Review Letters* **88,** 137401 (2002).

112 Nirmal, M. *et al.* Fluorescence intermittency in single cadmium selenide nanocrystals. *Nature* **383,** 802–804 (1996).

113 Hardman, R. A Toxicologic review of quantum dots: toxicity depends on physicochemical and environmental factors. *Environ Health Perspect* **114,** 165–172 (2006).

114 Derfus, A. M., Chan, W. C. W. & Bhatia, S. N. Probing the cytotoxicity of semiconductor quantum dots. *Nano Letters* **4,** 11–18 (2004).

115 Yang, Y. Upconversion nanophosphors for use in bioimaging, therapy, drug delivery and bioassays. *Microchimica Acta* **181,** 263–294 (2014).

116 Auzel, F. Upconversion and anti-stokes processes with f and d ions in solids. *Chemical Reviews* **104,** 139–174 (2004).

117 Gamelin, D. R. & Güdel, H. U. Design of luminescent inorganic materials: new photophysical processes studied by optical spectroscopy. *Accounts of Chemical Research* **33,** 235–242 (2000).

118 Haase, M. & Schäfer, H. Upconverting nanoparticles. *Angewandte Chemie International Edition* **50,** 5808–5829 (2011).

119 Drobizhev, M., Makarov, N. S., Tillo, S. E., Hughes, T. E. & Rebane, A. Two-photon absorption properties of fluorescent proteins. *Nature Methods* **8,** 393–399 (2011).

120 Yao, S. & Belfield, K. D. Two-photon fluorescent probes for bioimaging. *European Journal of Organic Chemistry.* **2012,** 3199–3217 (2012).

121 Campagnola, P. Second harmonic generation imaging microscopy: applications to diseases diagnostics. *Analytical Chemistry* **83,** 3224–3231 (2011).

122 Reeve, J. E., Anderson, H. L. & Clays, K. Dyes for biological second harmonic generation imaging. *Physical Chemistry Chemical Physics* **12,** 13484 (2010).

123 Heer, S., Kömpe, K., Güdel, H.-U. & Haase, M. Highly efficient multicolour upconversion emission in transparent colloids of lanthanide-doped NaYF4 nanocrystals. *Advanced Materials* **16,** 2102–2105 (2004).

124 Huang, L. & Cheng, J.-X. Nonlinear optical microscopy of single nanostructures. *Annual Review of Materials Research* **43,** 213–236 (2013).

125 Wang, F. & Liu, X. Multicolor tuning of lanthanide-doped nanoparticles by single wavelength excitation. *Accounts of Chemical Research* **47,** 1378–1385 (2014).

126 Bünzli, J.-C. G. Lanthanide luminescence for biomedical analyses and imaging. *Chemical Reviews* **110,** 2729–2755 (2010).

127 Eliseeva, S. V. & Bünzli, J.-C. G. Lanthanide luminescence for functional materials and bio-sciences. *Chemical Society Reviews* **39,** 189–227 (2009).

128 Wang, F. & Liu, X. Recent advances in the chemistry of lanthanide-doped upconversion nanocrystals. *Chemical Society Reviews* **38,** 976–989 (2009).

129 Wang, G., Peng, Q. & Li, Y. Lanthanide-doped nanocrystals: synthesis, optical-magnetic properties, and Aaplications. *Accounts of Chemical Research* **44,** 322–332 (2011).

130 Aebischer, A. *et al.* Structural and spectroscopic characterization of active sites in a family of light-emitting sodium lanthanide tetrafluorides. *Angewandte Chemie International Edition* **45,** 2802–2806 (2006).

131 Aebischer, A. *et al.* Visible light emission upon near-infrared excitation in a transparent solution of nanocrystalline β-NaGdF$_4$: Yb^{3+}, Er^{3+}. *Chemical Physics Letters* **407,** 124–128 (2005).

132 Boyer, J.-C., Cuccia, L. A. & Capobianco, J. A. Synthesis of colloidal upconverting NaYF$_4$: Er^{3+}/Yb^{3+} and Tm^{3+}/Yb^{3+} monodisperse nanocrystals. *Nano Letters* **7,** 847–852 (2007).

133 Renero-Lecuna, C. *et al.* Origin of the high upconversion green luminescence efficiency in β-NaYF$_4$:2%Er^{3+},20%Yb^{3+}. *Chemisty of Materials.* **23,** 3442–3448 (2011).

134 Thoma, R. E., Insley, H. & Hebert, G. M. The sodium fluoride-lanthanide trifluoride systems. *Inorganic Chemisty* **5,** 1222–1229 (1966).

135 Chan, E. M. *et al.* Reproducible, high-throughput synthesis of colloidal nanocrystals for optimization in multidimensional parameter space. *Nano Letters* **10,** 1874–1885 (2010).

136 Krämer, K. W. *et al.* Hexagonal sodium yttrium fluoride based green and blue emitting upconversion phosphors. *Chemistry of Materials* **16,** 1244–1251 (2004).

137 Wang, F., Banerjee, D., Liu, Y., Chen, X. & Liu, X. Upconversion nanoparticles in biological labeling, imaging, and therapy. *Analyst* **135,** 1839–1854 (2010).

138 Rocha, J., Carlos, L. D., Paz, F. A. A. & Ananias, D. Luminescent multifunctional lanthanides-based metal–organic frameworks. *Chemical Society Reviews* **40,** 926 (2011).

139 Liu, Y., Tu, D., Zhu, H. & Chen, X. Lanthanide-doped luminescent nanoprobes: controlled synthesis, optical spectroscopy, and bioapplications. *Chemical Society Reviews* **42,** 6924 (2013).

140 Veggel, F. C. J. M. van, Dong, C., Johnson, N. J. J. & Pichaandi, J. Ln^{3+}-doped nanoparticles for upconversion and magnetic resonance imaging: some critical notes on recent progress and some aspects to be considered. *Nanoscale* **4,** 7309–7321 (2012).

141 Smith, A. M., Mancini, M. C. & Nie, S. Bioimaging: second window for in vivo imaging. *Nature Nanotechnology* **4,** 710–711 (2009).

142 Lin, M. *et al.* Recent advances in synthesis and surface modification of lanthanide-doped upconversion nanoparticles for biomedical applications. *Biotechnology Advances* **30,** 1551–1561 (2012).

143 Hilderbrand, S. A. & Weissleder, R. Near-infrared fluorescence: application to in vivo molecular imaging. *Current Opinion in Chemical Biology* **14,** 71–79 (2010).

144 Zhou, J., Liu, Z. & Li, F. Upconversion nanophosphors for small-animal imaging. *Chemical Society Reviews* **41,** 1323 (2012).

145 Wu, S. *et al.* Non-blinking and photostable upconverted luminescence from single lanthanide-doped nanocrystals. *PNAS* **106,** 10917–10921 (2009).

146 Yi, G. *et al.* Synthesis, characterization, and biological application of size-controlled nanocrystalline NaYF$_4$:Yb,Er infrared-to-visible up-conversion phosphors. *Nano Letters* **4,** 2191–2196 (2004).

147 Li, C. & Lin, J. Rare earth fluoride nano-/microcrystals: synthesis, surface modification and application. *Journal of Materials Chemistry* **20,** 6831–6847 (2010).

148 Chatterjee, D. K., Gnanasammandhan, M. K. & Zhang, Y. Small upconverting fluorescent nanoparticles for biomedical applications. *Small* **6,** 2781–2795 (2010).

149 Mai, H.-X. *et al.* High-quality sodium rare-earth fluoride nanocrystals: controlled synthesis and optical properties. *Journal of the American Chemical Society* **128,** 6426–6436 (2006).

150 Wei, Y., Lu, F., Zhang, X. & Chen, D. Synthesis of oil-dispersible hexagonal-phase and hexagonal-shaped NaYF$_4$:Yb,Er nanoplates. *Chemistry of Materials* **18,** 5733–5737 (2006).

151 Liu, X. *et al.* Ionothermal synthesis of hexagonal-phase NaYF$_4$:Yb^{3+},Er^{3+}/Tm^{3+} upconversion nanophosphors. *Chemical Communications.* 6628–6630 (2009).

152 Chen, C. *et al.* Ionic liquid-based route to spherical NaYF$_4$ aanoclusters with the assistance of microwave radiation and their multicolor upconversion luminescence. *Langmuir* **26,** 8797–8803 (2010).

153 Jin, J. *et al.* Polymer-coated NaYF$_4$:Yb^{3+}, Er^{3+} upconversion nanoparticles for charge-dependent cellular imaging. *ACS Nano* **5,** 7838–7847 (2011).

154 Yi, G. S. & Chow, G. M. Synthesis of hexagonal-phase NaYF$_4$:Yb,Er and NaYF$_4$:Yb,Tm nanocrystals with efficient up-conversion fluorescence. *Advanced Functional Materials* **16,** 2324–2329 (2006).

155 Zhao, J. *et al.* Upconversion luminescence with tunable lifetime in NaYF$_4$:Yb,Er nanocrystals: role of nanocrystal size. *Nanoscale* **5,** 944–952 (2013).

156 Wang, F., Wang, J. & Liu, X. Direct evidence of a surface quenching effect on size-dependent luminescence of upconversion nanoparticles. *Angewandte Chemie International Edition* **49,** 7456–7460 (2010).

157 Erathodiyil, N. & Ying, J. Y. Functionalization of inorganic nanoparticles for bioimaging applications. *Accounts of Chemical Research* **44,** 925–935 (2011).

158 Wang, M., Abbineni, G., Clevenger, A., Mao, C. & Xu, S. Upconversion nanoparticles: synthesis, surface modification and biological applications. *Nanomedicine: Nanotechnology, Biology and Medicine* **7,** 710–729 (2011).

159 Jiang, S. *et al.* Surface-functionalized nanoparticles for biosensing and imaging-guided therapeutics. *Nanoscale* **5,** 3127 (2013).

160 Gu, Z. *et al.* Recent advances in design and fabrication of upconversion nanoparticles and their safe theranostic applications. *Advanced Materials* **25,** 3758–3779 (2013).

161 Xiong, L.-Q. *et al.* Synthesis, characterization, and in vivo targeted imaging of amine-functionalized rare-earth up-converting nanophosphors. *Biomaterials* **30,** 5592–5600 (2009).

162 Xiong, L. *et al.* High contrast upconversion luminescence targeted imaging in vivo using peptide-labeled nanophosphors. *Analytical Chemistry* **81,** 8687–8694 (2009).

163 Xiong, L., Yang, T., Yang, Y., Xu, C. & Li, F. Long-term in vivo biodistribution imaging and toxicity of polyacrylic acid-coated upconversion nanophosphors. *Biomaterials* **31,** 7078–7085 (2010).

164 Liu, Q. *et al.* Multifunctional rare-earth self-assembled nanosystem for tri-modal upconversion luminescence /fluorescence /positron emission tomography imaging. *Biomaterials* **32,** 8243–8253 (2011).

165 Zhou, J.-C. *et al.* Bioimaging and toxicity assessments of near-infrared upconversion luminescent NaYF$_4$:Yb,Tm nanocrystals. *Biomaterials* **32,** 9059–9067 (2011).

166 Xu, C. T. *et al.* Upconverting nanoparticles for pre-clinical diffuse optical imaging, microscopy and sensing: Current trends and future challenges. *Laser & Photonics Reviews* **7,** 663–697 (2013).

167 Gorris, H. H. & Wolfbeis, O. S. Photon-upconverting nanoparticles for optical encoding and multiplexing of cells, biomolecules, and microspheres. *Angewandte Chemie International Edition* **52,** 3584–3600 (2013).

168 Mader, H. S., Kele, P., Saleh, S. M. & Wolfbeis, O. S. Upconverting luminescent nanoparticles for use in bioconjugation and bioimaging. *Current Opinion in Chemical Biology* **14,** 582–596 (2010).

169 Achatz, D. E., Ali, R. & Wolfbeis, O. S. in Luminescence applied in sensor science (Prodi, L., Montalti, M. & Zaccheroni, N.) 29–50 *Springer Berlin Heidelberg* (2011).

170 Hallouard, F., Anton, N., Choquet, P., Constantinesco, A. & Vandamme, T. Iodinated blood pool contrast media for preclinical X-ray imaging applications – A review. *Biomaterials* **31,** 6249–6268 (2010).

171 Lee, J.-H. *et al.* Artificially engineered magnetic nanoparticles for ultra-sensitive molecular imaging. *Nature Medicine* **13,** 95–99 (2007).

172 Hilderbrand, S. A., Shao, F., Salthouse, C., Mahmood, U. & Weissleder, R. Upconverting luminescent nanomaterials: application to in vivo bioimaging. *Chemical Communications* 4188–4190 (2009).

173 Agasti, S. S. *et al.* Nanoparticles for detection and diagnosis. *Advanced Drug Delivery Reviews* **62,** 316–328 (2010).

174 Von Maltzahn, G. *et al.* Nanoparticles that communicate in vivo to amplify tumour targeting. *Nature Materials* **10,** 545–552 (2011).

175 Zrazhevskiy, P., Sena, M. & Gao, X. Designing multifunctional quantum dots for bioimaging, detection, and drug delivery. *Chemical Society Reviews* **39,** 4326 (2010).

176 Wang, H., Leeuwenburgh, S. C. G., Li, Y. & Jansen, J. A. The use of micro- and nanospheres as functional components for bone tissue regeneration. *Tissue Engineering Part B: Reviews* **18,** 24–39 (2012).

177 Davis, M. E. *et al.* Evidence of RNAi in humans from systemically administered siRNA via targeted nanoparticles. *Nature* **464,** 1067–1070 (2010).

178 Ma, X., Zhao, Y. & Liang, X.-J. Theranostic nanoparticles engineered for clinic and pharmaceutics. *Accounts of Chemical Research* **44,** 1114–1122 (2011).

179 Yong, K.-T. *et al.* Preparation of quantum dot/drug nanoparticle formulations for traceable targeted delivery and therapy. *Theranostics* **2,** 681–694 (2012).

180 Park, J. *et al.* Ultra-large-scale syntheses of monodisperse nanocrystals. *Nature Materials* **3,** 891–895 (2004).

181 Frey, N. A., Peng, S., Cheng, K. & Sun, S. Magnetic nanoparticles: synthesis, functionalization, and applications in bioimaging and magnetic energy storage. *Chemical Society Reviews* **38,** 2532 (2009).

182 Ye, X. *et al.* Morphologically controlled synthesis of colloidal upconversion nanophosphors and their shape-directed self-assembly. *Proceedings of the National Academy of Sciences* **107,** 22430–22435 (2010).

183 Singamaneni, S., Bliznyuk, V. N., Binek, C. & Tsymbal, E. Y. Magnetic nanoparticles: recent advances in synthesis, self-assembly and applications. *Journal of Materials Chemistry* **21,** 16819 (2011).

184 Shao, H. *et al.* Magnetic nanoparticles and microNMR for diagnostic applications. *Theranostics* **2,** 55–65 (2012).

185 Gao, J., Gu, H. & Xu, B. Multifunctional magnetic nanoparticles: design, synthesis, and biomedical applications. *Accounts of Chemical Research* **42,** 1097–1107 (2009).

186 Boisselier, E. & Astruc, D. Gold nanoparticles in nanomedicine: preparations, imaging, diagnostics, therapies and toxicity. *Chemical Society Reviews* **38,** 1759 (2009).

187 Alivisatos, A. P., Gu, W. & Larabell, C. Quantum dots as cellular probes. *Annual Review of Biomedical Engineering* **7,** 55–76 (2005).

188 Liu, L. *et al.* Bioconjugated pluronic triblock-copolymer micelle-encapsulated quantum dots for targeted imaging of cancer: in vitro and in vivo studies. *Theranostics* **2,** 705–713 (2012).

189 Zhuang, Z., Peng, Q. & Li, Y. Controlled synthesis of semiconductor nanostructures in the liquid phase. *Chemical Society Reviews* **40,** 5492 (2011).

190 Zou, H., Wu, S. & Shen, J. Polymer/silica nanocomposites: preparation, characterization, properties, and applications. *Chemical Reviews* **108,** 3893–3957 (2008).

191 Vennerberg, D. & Lin, Z. Upconversion nanocrystals: synthesis, properties, assembly and applications. *Science of Advanced Materials* **3,** 26–40 (2011).

192 Menyuk, N., Dwight, K. & Pierce, J. W. $NaYF_4$: Yb,Er—an efficient upconversion phosphor. *Applied Physics Letters* **21,** 159–161 (1972).

193 Park, Y. I. *et al.* Nonblinking and nonbleaching upconverting nanoparticles as an optical imaging nanoprobe and T1 magnetic resonance imaging contrast agent. *Advanced Materials* **21,** 4467–4471 (2009).

194 Wang, F. *et al.* Simultaneous phase and size control of upconversion nanocrystals through lanthanide doping. *Nature* **463,** 1061–1065 (2010).

195 Chen, G. *et al.* (α-NaYbF$_4$:Tm^{3+})/CaF$_2$ core/shell nanoparticles with efficient near-infrared to near-infrared upconversion for high-contrast deep tissue bioimaging. *ACS Nano* (2012).

196 Kuningas, K. *et al.* Upconversion fluorescence resonance energy transfer in a homogeneous immunoassay for estradiol. *Analytical Chemistry* **78,** 4690–4696 (2006).

197 Rantanen, T., Järvenpää, M.-L., Vuojola, J., Kuningas, K. & Soukka, T. Fluorescence-quenching-based enzyme-activity assay by using photon upconversion. *Angewandte Chemie* **120,** 3871–3873 (2008).

198 Abel, K. A., Boyer, J.-C. & Veggel, F. C. J. M. van. Hard proof of the NaYF$_4$/NaGdF$_4$ nanocrystal core/shell structure. *Journal of the American Chemical Society* **131,** 14644–14645 (2009).

199 Chen, G., Ohulchanskyy, T. Y., Kumar, R., Ågren, H. & Prasad, P. N. Ultrasmall monodisperse NaYF$_4$:Yb^{3+}/Tm^{3+} nanocrystals with enhanced near-infrared to near-infrared upconversion photoluminescence. *ACS Nano* **4,** 3163–3168 (2010).

200 Abdul Jalil, R. & Zhang, Y. Biocompatibility of silica coated NaYF$_4$ upconversion fluorescent nanocrystals. *Biomaterials* **29,** 4122–4128 (2008).

201 Johnson, N. J. J., Sangeetha, N. M., Boyer, J.-C. & Veggel, F. C. J. M. van. Facile ligand-exchange with polyvinylpyrrolidone and subsequent silica coating of hydrophobic upconverting β-NaYF$_4$:Yb^{3+}/Er^{3+} nanoparticles. *Nanoscale* **2,** 771–777 (2010).

202 Li, Z., Zhang, Y., Shuter, B. & Muhammad Idris, N. Hybrid lanthanide nanoparticles with paramagnetic shell coated on upconversion fluorescent nanocrystals. *Langmuir* **25,** 12015–12018 (2009).

203 Jana, N. R., Earhart, C. & Ying, J. Y. Synthesis of water-soluble and functionalized nanoparticles by silica coating. *Chemistry of Materials* **19,** 5074–5082 (2007).

204 Park, J. C., Gilbert, D. A., Liu, K. & Louie, A. Y. Microwave enhanced silica encapsulation of magnetic nanoparticles. *Journal of Materials Chemistry* **22,** 8449 (2012).

205 Salgueiriño-Maceira, V., Correa-Duarte, M. A., Spasova, M., Liz-Marzán, L. M. & Farle, M. Composite silica spheres with magnetic and luminescent functionalities. *Advanced Functional Materials* **16,** 509–514 (2006).

206 Mader, H. S. *et al.* Surface-modified upconverting microparticles and nanoparticles for use in click chemistries. *Chemistry – A European Journal* **16,** 5416–5424 (2010).

207 Ehlert, O., Thomann, R., Darbandi, M. & Nann, T. A four-color colloidal multiplexing nanoparticle system. *ACS Nano* **2,** 120–124 (2008).

208 Sivakumar, S., Diamente, P. R. & van Veggel, F. C. J. M. Silica-coated Ln^{3+}-doped LaF$_3$ nanoparticles as robust down- and upconverting biolabels. *Chemistry – A European Journal* **12,** 5878–5884 (2006).

209 Li, Z., Zhang, Y. & Jiang, S. Multicolor core/shell-structured upconversion fluorescent nanoparticles. *Advanced Materials* **20,** 4765–4769 (2008).

210 Mirsky, V. M., Riepl, M. & Wolfbeis, O. S. Capacitive monitoring of protein immobilization and antigen–antibody reactions on monomolecular alkylthiol films on gold electrodes. *Biosensors and Bioelectronics* **12,** 977–989 (1997).

211 Qian, H.-S. & Zhang, Y. Synthesis of hexagonal-phase core−shell NaYF$_4$ nanocrystals with tunable upconversion fluorescence. *Langmuir* **24,** 12123–12125 (2008).

212 Sedlmeier, A., Achatz, D. E., Fischer, L. H., Gorris, H. H. & Wolfbeis, O. S. Photon upconverting nanoparticles for luminescent sensing of temperature. *Nanoscale* **4,** 7090–7096 (2012).

213 Miller, S. A., Rast, H. E. & Caspers, H. H. Lattice vibrations of LiYF$_4$. *The Journal of Chemical Physics* **52,** 4172–4175 (1970).

214 Chen, G., Ohulchanskyy, T. Y., Kachynski, A., Ågren, H. & Prasad, P. N. Intense visible and near-infrared upconversion photoluminescence in colloidal LiYF$_4$:Er^{3+} nanocrystals under excitation at 1490 nm. *ACS Nano* **5,** 4981–4986 (2011).

215 Suyver, J. F. *et al.* Upconversion spectroscopy and properties of NaYF$_4$ doped with Er^{3+}, Tm^{3+} and/or Yb^{3+}. *Journal of Luminescence* **117,** 1–12 (2006).

216 Liu, G. K., Chen, X. Y., Zhuang, H. Z., Li, S. & Niedbala, R. S. Confinement of electron–phonon interaction on luminescence dynamics in nanophosphors of Er^{3+}:Y$_2$O$_2$S. *Journal of Solid State Chemistry* **171,** 123–132 (2003).

217 Tandon, P., Förster, G., Neubert, R. & Wartewig, S. Phase transitions in oleic acid as studied by X-ray diffraction and FT-Raman spectroscopy. *Journal of Molecular Structure* **524,** 201–215 (2000).

218 Mayo, D. W., Foil F. A., Hannah R. W. Course notes on the interpretation of infrared and Raman spectra. Chichester, USA: John Wiley and Sons (2004)

219 Breitsprecher, D. *et al.* Rocket launcher mechanism of collaborative actin assembly defined by single-molecule imaging. *Science* **336,** 1164–1168 (2012).

220 Sperling, R. A. & Parak, W. J. Surface modification, functionalization and bioconjugation of colloidal inorganic nanoparticles. *Philosophical Transactions of the Royal Society A* **368,** 1333–1383 (2010).

221 Schasfoort R. B. M., Tudos A. J., Handbook of surface plasmon resonance. *Cambridge, UK: Royal Society of Chemistry* (2008).

222 Liebherr, R. B., Soukka, T., Wolfbeis, O. S. & Gorris, H. H. Maleimide activation of photon upconverting nanoparticles for bioconjugation. *Nanotechnology* **23,** 485103 (2012).

223 Zhang, J., Li, B., Zhang, L. & Jiang, H. An optical sensor for Cu(II) detection with upconverting luminescent nanoparticles as an excitation source. *Chemical Communications* **48,** 4860–4862 (2012).

224 Cheng, L., Wang, C. & Liu, Z. Upconversion nanoparticles and their composite nanostructures for biomedical imaging and cancer therapy. *Nanoscale* **5,** 23–37 (2012).

225 Del Barrio, M. *et al.* Enzyme-induced modulation of the emission of upconverting nanoparticles: Towards a new sensing scheme for glucose. *Biosensors and Bioelectronics* **59,** 14–20 (2014).

226 Vetrone, F. *et al.* Temperature sensing using fluorescent nanothermometers. *ACS Nano* **4,** 3254–3258 (2010).

227 Zhou, Y., Xu, Z. & Yoon, J. Fluorescent and colorimetric chemosensors for detection of nucleotides, FAD and NADH: highlighted research during 2004–2010. *Chemical Society Reviews* **40,** 2222 (2011).

228 Mayevsky, A. & Barbiro-Michaely, E. Use of NADH fluorescence to determine mitochondrial function in vivo. *The International Journal of Biochemistry & Cell Biology* **41,** 1977–1988 (2009).

229 Álvarez-González, M. I., Saidman, S. B., Lobo-Castañón, M. J., Miranda-Ordieres, A. J. & Tuñón-Blanco, P. Electrocatalytic detection of NADH and glycerol by NAD^+-modified carbon electrodes. *Analytical Chemistry* **72,** 520–527 (2000).

230 Malinauskas, A., Ruzgas, T., Gorton, L. & Kubota, L. T. A reagentless amperometric carbon paste based sensor for NADH. *Electroanalysis* **12,** 194–198 (2000).

231 Tang, L. *et al.* Highly sensitive sensor for detection of NADH based on catalytic growth of Au nanoparticles on glassy carbon electrode. *Analytical and Bioanalytical Chemistry* **393,** 1677–1684 (2009).

232 Gros, P. & Comtat, M. A bioelectrochemical polypyrrole-containing $Fe(CN)_6^{3-}$ interface for the design of a NAD-dependent reagentless biosensor. *Biosensors and Bioelectronics* **20,** 204–210 (2004).

233 Jaegfeldt, H., Kuwana, T. & Johansson, G. Electrochemical stability of catechols with a pyrene side chain strongly adsorbed on graphite electrodes for catalytic oxidation of dihydronicotinamide adenine dinucleotide. *Journal of the American Chemical Society* **105,** 1805–1814 (1983).

234 Schubert, K., Khalid, W., Yue, Z., Parak, W. J. & Lisdat, F. Quantum-dot-modified electrode in combination with NADH-dependent dehydrogenase reactions for substrate analysis. *Langmuir* **26,** 1395–1400 (2010).

235 Passonneau, J. V. & Lowry, O. H. Enzymatic analysis: a practical guide. *Springer* (1993).

236 Borisov, S. M. & Wolfbeis, O. S. Optical Biosensors. *Chemical Reviews* **108,** 423–461 (2008).

237 Georgakoudi, I. & Quinn, K. P. Optical Imaging Using Endogenous Contrast to Assess Metabolic State. *Annual Review of Biomedical Engineering* **14,** 351–367 (2012).

238 Marose, S., Lindemann, C., Ulber, R. & Scheper, T. Optical sensor systems for bioprocess monitoring. *Trends in Biotechnology* **17,** 30–34 (1999).

239 Wolfbeis, O. S. & Leiner, M. Mapping of the total fluorescence of human blood serum as a new method for its characterization. *Analytica Chimica Acta* **167,** 203–215 (1985).

240 Miller, J. N. in Standardization and quality assurance in fluorescence measurements I (Resch-Genger, U.) 147–162 *Springer Berlin Heidelberg* (2008).

241 Liu, S., Shi, F., Chen, L. & Su, X. Albumin coated $CuInS_2$ quantum dots as a near-infrared fluorescent probe for NADH, and their application to an assay for pyruvate. *Microchim Acta* **181,** 339–345 (2014).

242 Freeman, R. *et al.* Biosensing and probing of intracellular metabolic pathways by NADH-sensitive quantum dots. *Angewandte Chemie International Edition* **48,** 309–313 (2009).

243 Harvey, P., Oakland, C., Driscoll, M. D., Hay, S. & Natrajan, L. S. Ratiometric detection of enzyme turnover and flavin reduction using rare-earth upconverting phosphors. *Dalton Transactions* **43,** 5265 (2014).

244 Johnson, N. J. J., Korinek, A., Dong, C. & van Veggel, F. C. J. M. Self-focusing by ostwald ripening: a strategy for layer-by-layer epitaxial growth on upconverting nanocrystals. *Journal of the American Chemical Society* **134,** 11068–11071 (2012).

245 Pellegrino, T. *et al.* Hydrophobic nanocrystals coated with an amphiphilic polymer shell: a general route to water soluble nanocrystals. *Nano Letters* **4,** 703–707 (2004).

246 Sperling, R. A., Pellegrino, T., Li, J. K., Chang, W. H. & Parak, W. J. Electrophoretic separation of nanoparticles with a discrete number of functional groups. *Advanced Functional Materials* **16,** 943–948 (2006).

247 Wilhelm, S. *et al.* Multicolor upconversion nanoparticles for protein conjugation. *Theranostics* **3,** 239–248 (2013).

248 Langford, J. I. & Wilson, A. J. C. Scherrer after sixty years: A survey and some new results in the determination of crystallite size. *Journal of Applied Crystallography* **11,** 102–113 (1978).

249 Johnson, N. J. J. & Veggel, F. C. J. M. van. Sodium lanthanide fluoride core-shell nanocrystals: A general perspective on epitaxial shell growth. *Nano Research.* **6,** 547–561 (2013).

250 Mayevsky, A. & Chance, B. Oxidation–reduction states of NADH *in vivo*: from animals to clinical use. *Mitochondrion* **7,** 330–339 (2007).

251 Li, L. Z., Xu, H. N., Ranji, M., Nioka, S. & Chance, B. Mitochondrial redox imaging for cancer diagnostic and therapeutic studies. *Journal of Innovative Optial Health Sciences* **02,** 325–341 (2009).

252 Schafer, F. Q. & Buettner, G. R. Redox environment of the cell as viewed through the redox state of the glutathione disulfide/glutathione couple. *Free Radical Biology and Medicine* **30,** 1191–1212 (2001).

253 Huang, S., Heikal, A. A. & Webb, W. W. Two-photon fluorescence spectroscopy and microscopy of NAD(P)H and flavoprotein. *Biophysical Journal* **82,** 2811–2825 (2002).

254 Patterson, G. H. & Piston, D. W. Photobleaching in two-photon excitation microscopy. *Biophysical Journal* **78,** 2159–2162 (2000).

255 Zhang, F. *et al.* Fabrication of Ag@SiO$_2$@Y$_2$O$_3$:Er nanostructures for bioimaging: tuning of the upconversion fluorescence with silver nanoparticles. *Journal of the American Chemical Society* **132,** 2850–2851 (2010).

256 Kumar, R., Nyk, M., Ohulchanskyy, T. Y., Flask, C. A. & Prasad, P. N. Combined optical and MR bioimaging using rare earth ion doped NaYF$_4$ nanocrystals. *Advanced Functional Materials* **19,** 853–859 (2009).

257 Wang, X. *et al.* Imaging of cellular oxygen via two-photon excitation of fluorescent sensor nanoparticles. *Sensors and Actuators B: Chemical* **188,** 257–262 (2013).

258 Mout, R., Moyano, D. F., Rana, S. & Rotello, V. M. Surface functionalization of nanoparticles for nanomedicine. *Chemical Society Reviews* **41,** 2539–2544 (2012).

259 Bünzli, J.-C. G. & Piguet, C. Taking advantage of luminescent lanthanide ions. *Chemical Society Reviews* **34,** 1048 (2005).

260 Bischof, C., Wahsner, J., Scholten, J., Trosien, S. & Seitz, M. Quantification of C−H quenching in near-IR luminescent ytterbium and neodymium cryptates. *Journal of the American Chemical Society* **132,** 14334–14335 (2010).

261 Liu, H. *et al.* Balancing power density based quantum yield characterization of upconverting nanoparticles for arbitrary excitation intensities. *Nanoscale* **5,** 4770–4775 (2013).

262 Kou, L., Labrie, D. & Chylek, P. Refractive indices of water and ice in the 0.65- to 2.5-μm spectral range. *Applied Optics* **32,** 3531–3540 (1993).

263 Resch-Genger, U. *et al.* State-of-the art comparability of corrected emission spectra. 2. Field laboratory assessment of calibration performance using spectral fluorescence standards. *Analytical Chemistry* **84,** 3899–3907 (2012).

264 Würth, C., Pauli, J., Lochmann, C., Spieles, M. & Resch-Genger, U. Integrating sphere setup for the traceable measurement of absolute photoluminescence quantum yields in the near infrared. *Analytical Chemisty* **84,** 1345–1352 (2012).

265 Li, L.-L. *et al.* Biomimetic surface engineering of lanthanide-doped upconversion nanoparticles as versatile bioprobes. *Angewandte Chemie International Edition* **51,** 6121–6125 (2012).

266 Abdul Jalil, R. & Zhang, Y. Biocompatibility of silica coated NaYF$_4$ upconversion fluorescent nanocrystals. *Biomaterials* **29,** 4122–4128 (2008).

267 Zhang, F. *et al.* Polymer-coated nanoparticles: a universal tool for biolabelling experiments. *Small* **7,** 3113–3127 (2011).

268 Sperling, R. A. *et al.* Size determination of (bio)conjugated water-soluble colloidal nanoparticles: a comparison of different techniques. *The Journal of Physical Chemistry C* **111,** 11552–11559 (2007).

269 De Geyter, B. *et al.* The different nature of band edge absorption and emission in colloidal PbSe/CdSe core/shell quantum dots. *ACS Nano* **5,** 58–66 (2011).

270 De la Presa, P., Multigner, M., de la Venta, J., García, M. A. & Ruiz-González, M. L. Structural and magnetic characterization of oleic acid and oleylamine-capped gold nanoparticles. *Journal of Applied Physics* **100,** 123915–123915–6 (2006).

271 Sperling, R. A. *et al.* Size Determination of (bio)conjugated water-soluble colloidal nanoparticles: a comparison of different techniques. *Journal of Physical Chemistry C* **111,** 11552–11559 (2007).

272 Dong, A. *et al.* A generalized ligand-exchange strategy enabling sequential surface functionalization of colloidal nanocrystals. *Journal of the American Chemical Society* **133,** 998–1006 (2011).

273 Schneider, G. & Decher, G. From functional core/shell nanoparticles prepared via layer-by-layer deposition to empty nanospheres. *Nano Letters* **4,** 1833–1839 (2004).

274 Schneider, G. & Decher, G. Functional core/shell nanoparticles via layer-by-layer assembly. Investigation of the experimental parameters for controlling particle aggregation and for enhancing dispersion stability. *Langmuir* **24,** 1778–1789 (2008).

275 Liu, C., Hou, Y. & Gao, M. Are rare-earth nanoparticles suitable for *in vivo* applications? *Advanced Materials.* n/a–n/a (2014). doi:10.1002/adma.201305535.

276 Hou, Y. *et al.* NaGdF$_4$ nanoparticle-based molecular probes for magnetic resonance imaging of intraperitoneal tumor xenografts *in vivo*. *ACS Nano* **7,** 330–338 (2013).

277 Chien, Y.-H. *et al.* Near-infrared light photocontrolled targeting, bioimaging, and chemotherapy with caged upconversion nanoparticles *in vitro* and *in vivo*. *ACS Nano* **7,** 8516–8528 (2013).

278 Suter, J. D., Pekas, N. J., Berry, M. T. & May, P. S. Real-time-monitoring of the synthesis of β-NaYF$_4$:17% Yb,3% Er nanocrystals using NIR-to-visible upconversion luminescence. *The Journal of Physical Chemistry C* (2014). doi:10.1021/jp502971j.

279 Boyer, J.-C. & Veggel, F. C. J. M. van. Absolute quantum yield measurements of colloidal NaYF$_4$: Er^{3+}, Yb^{3+} upconverting nanoparticles. *Nanoscale* **2,** 1417–1419 (2010).

280 Voss, B. & Haase, M. Intrinsic focusing of the particle size distribution in colloids containing nanocrystals of two different crystal phases. *ACS Nano* **7,** 11242–11254 (2013).

281 Boyer, J.-C., Vetrone, F., Cuccia, L. A. & Capobianco, J. A. Synthesis of colloidal upconverting NaYF$_4$ nanocrystals doped with Er^{3+}, Yb^{3+} and Tm^{3+}, Yb^{3+} via thermal decomposition of lanthanide trifluoroacetate precursors. *Journal of the American Chemical Society* **128,** 7444–7445 (2006).

282 Zou, W., Visser, C., Maduro, J. A., Pshenichnikov, M. S. & Hummelen, J. C. Broadband dye-sensitized upconversion of near-infrared light. *Nature Photonics* **6,** 560–564 (2012).

283 Ulman, A. Formation and structure of self-assembled monolayers. *Chemical Reviews* **96,** 1533–1554 (1996).

284 Drummond, D. C., Zignani, M. & Leroux, J.-C. Current status of pH-sensitive liposomes in drug delivery. *Progress in Lipid Research* **39,** 409–460 (2000).

285 Drummond, D. C., Meyer, O., Hong, K., Kirpotin, D. B. & Papahadjopoulos, D. Optimizing liposomes for delivery of chemotherapeutic agents to solid tumors. *Pharmacological Reviews* **51,** 691–744 (1999).

286 Hlaváček, A., Sedlmeier, A., Skládal, P. & Gorris, H. H. Electrophoretic characterization and purification of silica-coated photon-upconverting nanoparticles and their bioconjugates. *ACS Applied Materials and Interfaces* **6,** 6930–6935 (2014).

287 Boyer, J.-C., Manseau, M.-P., Murray, J. I. & van Veggel, F. C. J. M. Surface modification of upconverting NaYF$_4$ nanoparticles with PEG–phosphate ligands for NIR (800 nm) biolabeling within the biological window. *Langmuir* **26,** 1157–1164 (2010).

288 Pichaandi, J., Boyer, J.-C., Delaney, K. R. & van Veggel, F. C. J. M. Two-photon upconversion laser (scanning and wide-field) microscopy using Ln^{3+}-Doped NaYF$_4$ upconverting nanocrystals: a critical evaluation of their performance and potential in bioimaging. The *Journal of Physical Chemistry C* **115,** 19054–19064 (2011).

289 Zhan, Q., He, S., Qian, J., Cheng, H. & Cai, F. Optimization of optical excitation of upconversion nanoparticles for rapid microscopy and deeper tissue imaging with higher quantum yield. *Theranostics* **3,** 306–316 (2013).

290 Xu, C. T. *et al.* Autofluorescence insensitive imaging using upconverting nanocrystals in scattering media. *Applied Physics Letters* **93,** 171103 (2008).

291 He, X., Wang, K. & Cheng, Z. In vivo near-infrared fluorescence imaging of cancer with nanoparticle-based probes. *WIREs Nanomedicine and Nanobiotechnology* **2,** 349–366 (2010).

292 Melancon, M. P., Zhou, M. & Li, C. Cancer Theranostics with near-infrared light-activatable multimodal nanoparticles. *Accounts of Chemical Research* **44,** 947–956 (2011).

293 Zhan, Q. *et al.* Using 915 nm laser excited Tm^{3+}/Er^{3+}/Ho^{3+}-doped NaYbF$_4$ upconversion nanoparticles for in vitro and deeper in Vivo bioimaging without overheating irradiation. *ACS Nano* **5,** 3744–3757 (2011).

294 Kangasniemi, M. *et al.* Thermal therapy of canine cerebral tumors using a 980 nm diode laser with MR temperature-sensitive imaging feedback. *Lasers in Surgery Medicine.* **35,** 41–50 (2004).

295 Weissleder, R. A clearer vision for in vivo imaging. *Nature Biotechnology* **19,** 316–317 (2001).

296 Pollnau, M., Gamelin, D. R., Lüthi, S. R., Güdel, H. U. & Hehlen, M. P. Power dependence of upconversion luminescence in lanthanide and transition-metal-ion systems. *Physical Review B* **61,** 3337–3346 (2000).

297 Suyver, J. F., Aebischer, A., García-Revilla, S., Gerner, P. & Güdel, H. U. Anomalous power dependence of sensitized upconversion luminescence. *Physical Review B* **71,** 125123 (2005).

298 Page, R. H. *et al.* Upconversion-pumped luminescence efficiency of rare-earth-doped hosts sensitized with trivalent ytterbium. *Journal of the Optical Society of America B* **15,** 996–1008 (1998).

299 Gnach, A. & Bednarkiewicz, A. Lanthanide-doped up-converting nanoparticles: merits and challenges. *Nano Today* **7,** 532–563 (2012).

300 Jayakumar, M. kumara gnanasammandhan, Idris, N. M., Huang, K. & Zhang, Y. A paradigm shift in the excitation wavelength of upconversion nanoparticles. *Nanoscale* (2014). doi:10.1039/C4NR02422B

301 Shen, J. *et al.* Engineering the upconversion nanoparticle excitation wavelength: cascade censitization of tri-doped upconversion colloidal nanoparticles at 800 nm. *Advanced Optical Materials* **1,** 644–650 (2013).

302 Xie, X. *et al.* Mechanistic investigation of photon upconversion in Nd³⁺-sensitized core–shell nanoparticles. *Journal of the American Chemical Society* **135,** 12608–12611 (2013).

303 Wen, H. *et al.* Upconverting near-infrared light through energy management in core–shell–shell nanoparticles. *Angewandte Chemie International Edition* **52,** 13419–13423 (2013).

304 Wang, Y.-F. *et al.* Nd³⁺-sensitized upconversion nanophosphors: efficient in vivo bioimaging probes with minimized heating effect. *ACS Nano* **7,** 7200–7206 (2013).

305 Li, X. *et al.* Nd³⁺ sensitized up/down converting dual-mode nanomaterials for efficient in-vitro and in-vivo bioimaging excited at 800 nm. *Scientific Reports* **3,** (2013).

306 Zhong, Y. *et al.* Elimination of photon quenching by a transition layer to fabricate a quenching-shield sandwich structure for 800 nm excited upconversion luminescence of Nd³⁺-sensitized nanoparticles. *Advanced Materials* **26,** 2831–2837 (2014).

Eidesstattliche Erklärung

Ich erkläre hiermit an Eides statt, dass ich die vorliegende Arbeit ohne unzulässige Hilfe Dritter und ohne Benutzung anderer als der angegebenen Hilfsmittel angefertigt habe; die aus anderen Quellen direkt oder indirekt übernommenen Daten und Konzepte sind unter Angabe des Literaturzitats gekennzeichnet.

Weitere Personen waren an der inhaltlich-materiellen Herstellung der vorliegenden Arbeit nicht beteiligt. Insbesondere habe ich hierfür nicht die entgeltliche Hilfe eines Promotionsberaters oder anderer Personen in Anspruch genommen. Niemand hat von mir weder unmittelbar noch mittelbar geldwerte Leistungen für Arbeiten erhalten, die im Zusammenhang mit dem Inhalt der vorgelegten Dissertation stehen.

Die Arbeit wurde bisher weder im In- noch im Ausland in gleicher oder ähnlicher Form einer anderen Prüfungsbehörde vorgelegt.

Ort, Datum   Unterschrift